EFFICIENT MODE EXCITATION AND CONVERSION IN FEW-MODE FIBER FOR SPACE-DIVISION MULTIPLEXING SYSTEM

LEE YEN SIAN

INSTITUTE FOR ADVANCED STUDIES
UNIVERSITY OF MALAYA
KUALA LUMPUR

2019

EFFICIENT MODE EXCITATION AND CONVERSION IN FEW-MODE FIBER FOR SPACE-DIVISION MULTIPLEXING SYSTEM

LEE YEN SIAN

THESIS SUBMITTED IN FULFILMENT OF THE REQUIREMENTS FOR THE DEGREE OF DOCTOR OF PHILOSOPHY

INSTITUTE FOR ADVANCED STUDIES
UNIVERSITY OF MALAYA
KUALA LUMPUR

2019

UNIVERSITY OF MALAYA

ORIGINAL LITERARY WORK DECLARATION

Name of Candidate: Lee Yen Sian

Matric No: HHE150001

Name of Degree: Doctor of Philosophy (Photonics)

Title of Thesis ("this Work"):

Efficient Mode Excitation and Conversion in Few-Mode Fiber for Space-Division Multiplexing System

Field of Study: Photonics Engineering

I do solemnly and sincerely declare that:

(1) I am the sole author/writer of this Work;
(2) This Work is original;
(3) Any use of any work in which copyright exists was done by way of fair dealing and for permitted purposes and any excerpt or extract from, or reference to or reproduction of any copyright work has been disclosed expressly and sufficiently and the title of the Work and its authorship have been acknowledged in this Work;
(4) I do not have any actual knowledge nor do I ought reasonably to know that the making of this work constitutes an infringement of any copyright work;
(5) I hereby assign all and every rights in the copyright to this Work to the University of Malaya ("UM"), who henceforth shall be owner of the copyright in this Work and that any reproduction or use in any form or by any means whatsoever is prohibited without the written consent of UM having been first had and obtained;
(6) I am fully aware that if in the course of making this Work I have infringed any copyright whether intentionally or otherwise, I may be subject to legal action or any other action as may be determined by UM.

Candidate's Signature Date:

Subscribed and solemnly declared before,

Witness's Signature Date:

Name:

Designation:

ABSTRACT

Ever increasing demand on the transmission capacity of optical fiber communication network has led to the research interest in space-division multiplexing (SDM) technology. SDM has been deemed as a promising solution to expand the transmission capacity beyond the limit of ~100 Tb/s. It also aims to reduce the cost and energy consumption per bit of information being transmitted. Generally, there are two main approaches to SDM: (i) mode-division multiplexing (MDM) that employs the orthogonal spatial modes in few-mode fiber (FMF) and (ii) core multiplexing (CM) that employs spatially separated cores in a multi-core fiber (MCF). The key components for the implementation of the SDM by these approaches are the optical fibers, amplifiers and (de)-multiplexers. This thesis focuses on the investigation of mode conversion and polarisation manipulation in FMF that can find useful applications in the (de)-multiplexers of MDM. Firstly, $LP_{01} \rightarrow LP_{11}$ mode conversion and selective excitation in FMF by a tilted binary phase plate (BPP) were investigated. It was demonstrated in this work that a tilted BPP can enable efficient $LP_{01} \rightarrow LP_{11}$ mode conversion and excitation at operating wavelength longer than the design wavelength of the BPP. A method based on the peak intensity difference of the lobes in a LP_{11} mode profile has been proposed to estimate the LP_{01}:LP_{11} ratio of the mode profile recorded at the FMF output. Next, effect of the two-mode fiber (TMF) output facet angle on the output beam profile was investigated via simulation. Simulation has shown that output facet angle close to the critical angle of the fiber can convert the LP_{11} mode in the fiber into a single-lobe beam at the fiber output. Based on the simulation result, a simple and low cost $LP_{11} \rightarrow LP_{01}$ mode converter made from an angled-facet TMF (AFTMF) has been demonstrated experimentally. Following that, LP_{01} and LP_{11} modes were simultaneously excited in a TMF by core-offset splicing technique and the output of the TMF was spliced to a three-paddle two-mode fiber polarisation controller (TMPC). The output beam of the TMPC was split by a polarising beam splitter (PBS).

By tuning the paddles of the TMPC, it was observed at the PBS outputs that the LP_{01} and LP_{11} modes can be simultaneously aligned into two perpendicular polarisation states and split by the PBS. The mode profile and power at the PBS outputs were measured to evaluate the polarisation manipulation performance of the TMPC. Modal decomposition by numerical method was used to determine the modal purity of the mode profile. In addition, the stability of the mode purity, profile and power was analysed.

Keywords: Few-mode fiber; space-division multiplexing.

ABSTRAK

Permintaan yang semakin meningkat ke atas kapasiti penghantaran rangkaian komunikasi gentian optik telah membawa kepada minat dalam penyelidikan teknologi pemultipleksan pembahagian ruang (SDM). SDM telah dianggap sebagai satu penyelesaian yang menjanjikan untuk meningkatkan kapasiti panghantaran tersebut melebihi had ~100 Tb/s. Ia juga bertujuan untuk mengurangkan kos dan penggunaan tenaga untuk setiap bit maklumat yang dihantar. Secara umum, terdapat dua pendekatan utama kepada SDM: (i) pemultipleksan pembahagian mod (MDM) yang menggunakan mod-mod yang ortogonal dalam gentian beberapa mod (FMF) dan (ii) pemultipleksan teras (CM) yang menggunakan teras-teras yang terpisah dalam satu gentian berbilang teras (MCF). Komponen-komponen utama dalam pelaksanaan SDM dengan pendekatan-pendekatan di atas adalah gentian optik, penguat dan pemultipleks/penyahmultipleks. Tesis ini focus kepada penyelidikan penukaran mod dan manipulasi polarisasi dalam FMF yang mempunyai aplikasi-aplikasi yang berguna dalam pemultipleks/penyahmultipleks MDM. Pertama, penukaran mod $LP_{01} \rightarrow LP_{11}$ dan pengujaan secara terpilih dalam FMF dengan menggunakan plat fasa perduaan (BPP) yang condong telah diselidik. Dalam kerja ini, telah ditunjukkan bahawa BPP condong dapat mencapai penukaran dan pengujaan mod $LP_{01} \rightarrow LP_{11}$ yang efisien pada panjang gelombang operasi yang lebih panjang daripada panjang gelombang rekaan BPP tersebut. Satu kaedah berdasarkan perbezaan keamatan puncak lobus-lobus dalam profil mod LP_{11} telah dicadang untuk menganggar nisbah LP_{01}:LP_{11} bagi profil mod yang direkod di output FMF. Seterusnya, kesan sudut faset output gentian dua mod (TMF) ke atas profil alur output telah diselidik melalui simulasi. Simulasi menunjukkan bahawa sudut faset output yang mendekati sudut kritikal gentian dapat menukarkan mod LP_{11} dalam gentian kepada alur berlobus tunggal di output gentian. Berdasarkan keputusan simulasi, satu penukar mod $LP_{11} \rightarrow LP_{01}$ yang ringkas dan berkos rendah telah diperbuat daripada gentian dua mod dengan sudut faset output yang serong (AFTMF) dan ditunjukkan melalui eksperimen. Berikutan itu, mod LP_{01} dan LP_{11} telah diuja secara serentak dalam satu TMF menggunakan teknik sambat ofset-teras dan output TMF tersebut telah disambat kepada satu pengawal polarisasi gentian dua mode berdayung tiga (TMPC). Alur output TMPC tersebut telah dipecah oleh pemecah alur kutub (PBS). Dengan menala dayung-dayung TMPC, telah diperhatikan di output-output PBS bahawa mod LP_{01} dan LP_{11} dapat dijajar secara serentak kepada dua keadaan polarisasi yang bersudut tepat dan dipecah oleh PBS. Profil dan kuasa mod di output-output PBS telah diukur untuk menilai prestasi manipulasi polarisasi TMPC tersebut. Penguraian mod dengan kaedah berangka telah diguna untuk menentukan ketulenan mod bagi profil mod tersebut. Selain itu, kestabilan ketulenan, profil dan kuasa mod telah dianalisis.

Kata kunci: Gentian beberapa mod; pemultipleksan pembahagian ruang.

ACKNOWLEDGEMENTS

First of all, I would like to thank my supervisors Ir. Dr. Kok-Sing Lim and Distinguished Professor Harith Ahmad for giving me the opportunity to conduct this PhD research study at Photonics Research Centre, University of Malaya (PRCUM). Their guidance, support and assistance throughout my PhD study have been invaluable. I would also like to express my appreciation to the faculty members of PRCUM for providing various supports during this study. Special thanks to the staffs of PRCUM and Institute for Advanced Studies (IAS), University of Malaya for their administrative support.

Besides, I would like to acknowledge the Ministry of Education, Malaysia for its financial support through MyPhD program. Furthermore, Postgraduate Research Grant (PPP) awarded by University of Malaya (PG115-2015B) is acknowledged. In addition, Optiwave System Inc. is acknowledged for the free OptiFDTD 32-bit simulator.

Other than that, I am grateful for the suggestions and help provided by my colleagues (Dr. Muhammad Mahmood Ali, Dr. Dinusha Serandi Gunawardena, Dr. Man-Hong Lai, Dr. Md. Rajibul Islam, Mr. Muhammad Khairol Annuar Zaini, Ms. Nurul Asha Mohd Nazal and Mr. Daryl Tan). Last but not least, I wish to extend my gratitude to my family members and friends for their support throughout my PhD study.

TABLE OF CONTENTS

LIST OF FIGURES

LIST OF TABLES

LIST OF SYMBOLS AND ABBREVIATIONS

1-D	:	One-dimensional
2-D	:	Two-dimensional
AFTMF	:	Angled-facet two-mode fiber
AR	:	Anti-reflection
BPP	:	Binary phase plate
CCD	:	Charge-coupled device
CM	:	Core-multiplexing
DC	:	Direct-current
DI	:	De-ionised
DMD	:	Differential mode delay
DSP	:	Digital signal processing
EDFA	:	Erbium-doped fiber amplifier
FMF	:	Few-mode fiber
FM-FBG	:	Few-mode fiber Bragg grating
HOM	:	Higher-order mode
HWP	:	Half-wave plate
ICP	:	Inductively-coupled plasma
IPA	:	Isopropyl alcohol
LCoS	:	Liquid crystal on silicon
LID	:	Lobes intensity difference
LP	:	Linearly polarised
LPG	:	Long period grating
MCF	:	Multicore fiber
MC-FMF	:	Multicore few-mode fiber

MD	:	Modal dispersion
MDL	:	Mode dependent loss
MDM	:	Mode-division multiplexing
MER	:	Mode extinction ratio
MIMO	:	Multiple-input multiple-output
MMF	:	Multimode fiber
MSC	:	Mode selective coupler
OPD	:	Optical path difference
OPL	:	Optical path length
PBS	:	Polarising beam splitter
PC	:	Polarisation controller
PDI	:	Propagation direction interleaving
PR	:	Photoresist
QWP	:	Quarter-wave plate
RF	:	Radio frequency
RI	:	Refractive index
SDM	:	Space-division multiplexing
SLM	:	Spatial light modulator
SMF	:	Single-mode fiber
TLS	:	Tunable laser source
TMF	:	Two-mode fiber
TMPC	:	Three-paddle two-mode fiber polarisation controller
UV	:	Ultraviolet
WDM	:	Wavelength-division multiplexing

CHAPTER 1: INTRODUCTION

This chapter intends to provide a brief overview on the development in the field of telecommunication specifically passive optical devices for Space-Division Multiplexing (SDM) system. It also discusses the motivation for the research works to be presented in this thesis. In addition, the research objectives and outline of this thesis will be presented at the end of the chapter.

1.1 Historical Background

Revolution in the field of telecommunication has always brought significant impact to the society. Since the advent of telegraph in 1830s, new emerging telecommunication technologies have led to transmission of information at higher speed, larger capacity and longer distance. For example, the operation of the first successful transatlantic telegraph cable in 1866 greatly reduced the time for information exchange between Europe and North America. With the invention of telephone in 1876, voice transmission was made possible by means of continuously varying electrical signal. Following that, the expansion of telephone network across the globe has led to increasing demand on the transmission capacity. Then, the coaxial cable system was deployed in 1930s to increase the transmission capacity of telephone network. However, coaxial cable system suffers from high attenuation loss. Hence, the transmitted signals need to be amplified every few kilometres.

While the transmission of information by telegraph and telephone rely on the transmission of electrical signals in cables connecting two locations, scientific advancement has led to the development of wireless communication system that utilised electromagnetic carrier wave. In such system, information is incorporated into the carrier wave by a modulator and the modulated carrier wave is transmitted towards the receiver.

Radio wave and microwave are two commonly used electromagnetic carrier frequencies where information can be transmitted through free space over large distance. The maximum transmission rate is generally larger for carrier wave at higher frequency. Based on this concept, optical wave can provide higher transmission speed than radio wave and microwave. However, optical wave is easily affected by disturbance in atmosphere such as rain, snow or fog. This has limited the development of free space optical communication system. Besides, suitable light source for optical communication system is not available until the invention of laser in the early 1960s. In contrast, microwave communication system has benefited from the radar technology developed during World War II and it has been commercially employed for the transmission of telephone and television signals after the war.

Upon the invention of laser in early 1960s, interest in optical communication system was revitalised. Nevertheless, free space optical communication system was limited to short distance applications because optical wave is sensitive to disturbance in atmosphere. To overcome the problem, scientists have turned to optical waveguides for optical wave transmission, in analogous to the transmission of electrical signal by copper wires. Reflective light pipes and confocal waveguides employing gas or glass lenses were proposed and tested but they were found to be commercially impractical due to engineering difficulties and high transmission loss. On the other hand, the use of glass fiber has not been given serious consideration because the clearest glass in the market at that time was unable to meet the tolerable loss for long distance transmission.

In spite of that, Charles K. Kao and George A. Hockham at Standard Telecommunication Laboratories (STL) pursued an in-depth study on the problem of glass fiber. They suggested that the loss of a glass fiber to be used for optical communication system should be less than 20 dB/km and the loss can be reduced by improving the purity of the glass material. In 1966, their investigation on the use of dielectric optical fiber for optical communication system was published in the Proceeding of the Institute of Electrical Engineers (Kao & Hockham, 1966). It took another four years before Bob Maurer, Donald Keck and Peter Schultz from Corning Glass Works successfully fabricated a single mode fiber with loss of 16 dB/km at 633 nm in 1970 (Hecht, 1999). Continuous efforts have led to better optical fibers that met the requirement for practical application in communication. Concurrently, development of room temperature semiconductor laser with longer life time has provided a reliable optical light source for optical communication system. Development of low-loss optical fibers and compact light source have significantly advanced the field of optical fiber communication (Gambling, 2000).

The first field test of optical fiber communication system has been conducted in Chicago's Loop district in 1977, seven years after the successful fabrication of optical fiber with transmission loss below 20 dB/km. Since then, the optical fiber network has expanded rapidly in terms of coverage and transmission capacity with the introduction of new technologies such as optical amplifier, wavelength-division multiplexing, coherent detection, advanced modulation format and dispersion management (Gnauck, Tkach, Chraplyvy, & Li, 2008). Today, optical fiber submarine cables have connected the globe while the transmission capacity of an SMF has increased from ~45 Mb/s to >8 Tb/s (refer Figure 1.1).

1.2 Space-Division Multiplexing

The demand on the transmission capacity of optical fiber network has greatly increased as a result of tremendous growth in the utilisation of the Internet, smartphone and related applications such as high-definition video streaming and cloud-computing (Hecht, 2016). Over the past few decades, various technologies have been introduced to increase the transmission capacity of the SMF-based optical fiber network (Figure 1.1). This is achieved by exploiting the physical dimensions/degrees of freedom of light wave in SMF. However, the transmission capacity has upper limit of ~100 Tb/s per fiber due to Shannon capacity limit, fiber nonlinearity and limitation on optical amplifier bandwidths (Desurvire, 2006; Essiambre, Foschini, Kramer, & Winzer, 2008; Essiambre, Kramer, Winzer, Foschini, & Goebel, 2010). To overcome the transmission capacity crunch in SMF network, space-division multiplexing is deemed as one of the most promising solutions (Krummrich, 2011; A. Li, Chen, Amin, Ye, & Shieh, 2012; G. Li, Bai, Zhao, & Xia, 2014; Morioka, 2009; Richardson, Fini, & Nelson, 2013; P. J. Winzer, 2013). The technology is aimed to increase the transmission capacity of the optical fiber telecommunication network beyond the limit of ~100 Tb/s and reduce the average cost and energy consumption per bit of information.

In contrast to WDM that makes use of different wavelengths, SDM employs orthogonal fiber modes or spatially separated fiber cores as independent data channels. They formed the main approaches to SDM which are known as: (i) mode-division multiplexing (MDM) using few-mode fiber and (ii) core multiplexing (CM) using multi-core fiber. MDM using MMF has been demonstrated by Berdagué and Facq in 1982 (Berdagué & Facq, 1982) while Inao et al. has reported the fabrication and characterisation of MCF for optical fiber communication system as early as 1979 (Inao, Sato, Sentsui, Kuroha, & Nishimura, 1979). In MDM, the fundamental and higher-order spatial modes propagate in the FMF or MMF are used as independent data channels. Meanwhile, MCF consists of multiple single-mode cores is used in core multiplexing to increase the transmission capacity.

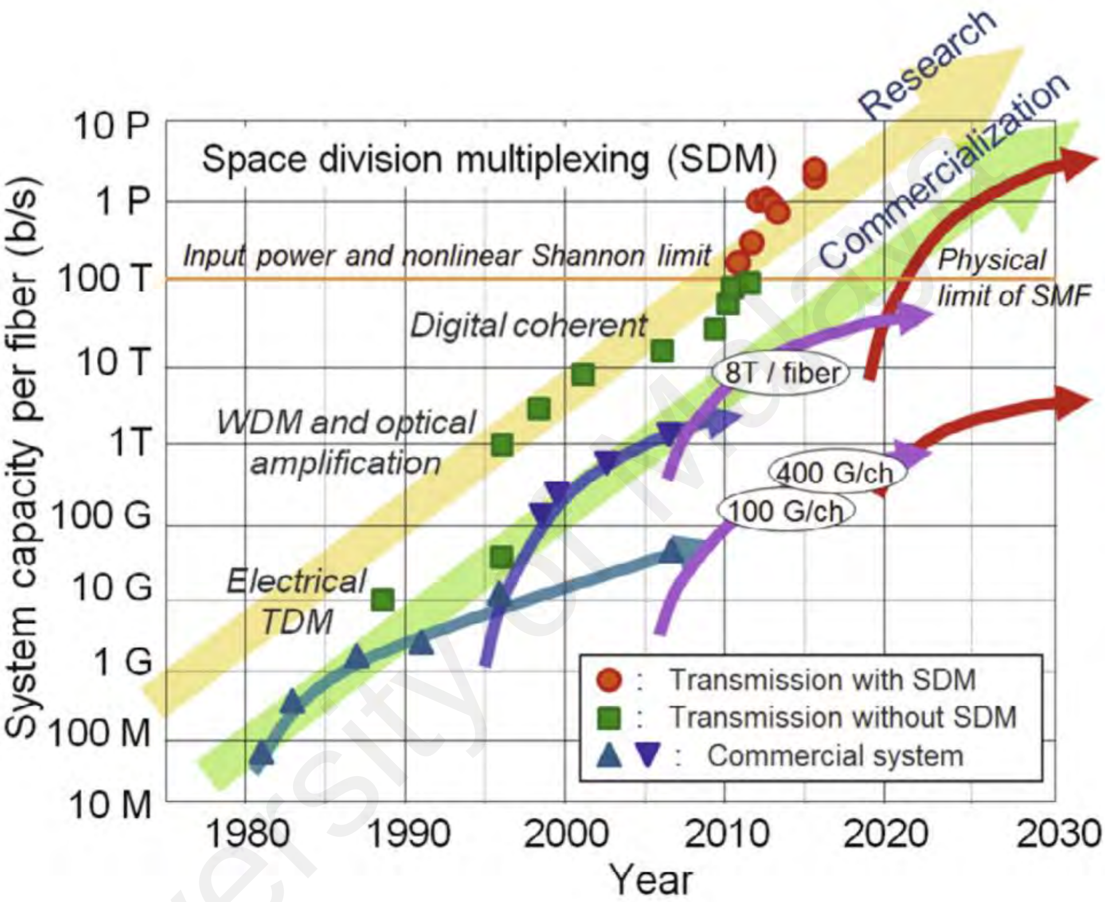

Figure 1.1: Growth in the transmission capacity of optical fiber system. (Mizuno & Miyamoto, 2017)

Although the concept of MDM and CM were first proposed and demonstrated more than 30 years ago, they only began to gain significant research interest around 2008. Murshid et al. revisited the concept of spatial multiplexing to increase the bandwidth of optical fiber systems in 2008 (Murshid, Grossman, & Narakorn, 2008). In the same year, the Extremely Advanced Transmission (EXAT) initiative was launched in Japan to explore solutions for the transmission capacity crunch of SMF-based network (Morioka, 2009). Universities and industry players in Europe had followed their footsteps in 2010 through MODE-GAP, a project funded under the European 7th Framework Program (FP7) (Ellis, 2013). In the early years, research works in Japan were generally based on CM technology while those in Europe and the United States had tended to explore the MDM technology. Many transmission experiments based on either MDM or CM had been reported in early 2010s (Koebele, Salsi, Milord, et al., 2011; Randel et al., 2011; Ryf, Randel, et al., 2011; Ryf, Randel, et al., 2012; Sakaguchi et al., 2011; Salsi et al., 2012; Sleiffer et al., 2012; Takara et al., 2012; Zhu et al., 2011). Integration of both multiplexing techniques to achieve higher transmission capacity had also been demonstrated by using MCF with few-mode cores (Qian et al., 2012; Takenaga et al., 2012; van Uden et al., 2014).

Three major components necessary for the implementation of SDM in optical fiber network are the optical fibers, amplifiers and (de)multiplexers that can accommodate higher-order modes or multiple cores. In a MDM system, input signals from multiple SMFs are converted/coupled into different spatial modes in an FMF by mode converters/couplers in the multiplexer before they are transmitted to the receiver. To overcome the transmission loss over the long FMF, few-mode amplifier can be used to boost up the signal power and keep their signal-to-noise ratio at healthy level. At the receiver end, de-multiplexer will separate the signals of different spatial modes and convert/couple them back to fundamental mode in SMFs.

On the other hand, for CM system that employs MCF with single-mode cores, input signals from SMFs are coupled into the MCF cores by multiplexer without the need of mode conversion. The multiplexer is known as fan-in device which could be free-space optics, bundled fiber or waveguide. The signals remain in fundamental mode during the transmission along the MCF. Multicore amplifier is used to amplify the signals in each core. At the receiver end, a fan-out device serves as a de-multiplexer to transfer the signals from each core back to SMFs. The fan-out device is similar to the fan-in device but operating in the opposite direction.

Mode dependent loss (MDL) and differential mode delay (DMD) due to modal dispersion (MD) are among the main technical challenges in the MDM approach. Meanwhile, crosstalk between spatial modes or cores is the major challenge in both MDM and CM approach. The MDL, DMD and crosstalk will deteriorate the quality of transmitted signals and hinder the growth in transmission capacity (Hayashi, 2013; Ho & Kahn, 2013; Peckham, Sun, McCurdy, & Lingle, 2013). Therefore, it is necessary to eliminate or minimise the impairments cause by them during the development of SDM technologies.

Meeting the demand in transmission capacity is not the only consideration in the development of SDM technologies. The technologies should also be attractive and beneficial from the economic point of view to ensure the success deployment of commercial SDM system. For that reason, newly developed SDM technologies should be compatible and can be integrated with the current optical fiber network infrastructure to achieve reduction in cost and energy consumption (Agrell et al., 2016; Kilper & Tucker, 2013; P. J. Winzer, 2011).

1.3 Motivation

In general, (de)multiplexer in MDM system achieves the (de)multiplexing process by matching either the profile or propagation constant of the input spatial mode to the target spatial mode. Most MDM transmission experiments reported in early 2010s multiplexed the spatial modes into FMF through profile-matching method (Koebele, Salsi, Milord, et al., 2011; Randel et al., 2011; Ryf, Randel, et al., 2011; Ryf, Randel, et al., 2012; Salsi et al., 2012; Sleiffer et al., 2012). To achieve that, mode converter was used to convert the mode profile of the input mode to that of the target mode. Then, the converted mode profiles are multiplexed into an FMF for transmission. Therefore, this technique is also known as convert-and-combine technique.

The convert-and-combined technique is commonly performed by matching the phase profile of the input mode to the target mode using binary phase plate (BPP) or spatial light modulator (SLM). Phase pattern on the BPP or SLM will introduce a phase shift of π to specific region of the input mode so that its phase profile is matched to that of the target mode. BPP is a passive component which is simpler to operate as compared to SLM. The phase pattern on the BPP is fixed and the alignment of the BPP with respect to the input mode profile is required to obtain a good converted mode profile.

However, BPP is fabricated to operate at a specific design wavelength and it has limited operating wavelength range. This is because a phase shift of π induced by the BPP is a function of the phase pattern thickness and the operating wavelength. If the operating wavelength deviates from the design wavelength, the induced phase shift will deviate from π, assuming that the phase pattern thickness is constant. Then, the converted phase profile will not match the target profile and the conversion is inefficient. Therefore, the phase pattern thickness needs to be adjusted accordingly with respect to the change in the operating wavelength to maintain the phase shift of π.

Despite that, a tilted BPP could be a convenient solution to maintain the phase shift of π without the need to change the phase pattern thickness. By tilting the BPP to different angles with respect to the light propagation direction, the optical path length across a tilted BPP will be longer than that across a non-tilted BPP (oriented perpendicular to the light propagation direction). This will enable a tilted BPP to perform efficient mode conversion at operating wavelengths beyond the design wavelength of the BPP and expand the operating wavelength range of the BPP. In spite of that, mode conversion performance of tilted BPP has never been reported in literature. Hence, it will be beneficial to conduct a research study into this matter which can improve our understanding on the functionality and performance of tilted BPP.

On the other hand, a mode converter with low fabrication cost, low insertion loss, high conversion purity, simple to operate, small physical size and good stability is desirable in the (de)multiplexer of MDM system. Wong et al. reported the observation of change in LP_{11} mode profile at the output of an angled-facet two-mode fiber (AFTMF) when the facet angle increases (Wang, Wang, & Claus, 1992). The intensity profile of a refracted two-lobe LP_{11} mode from the angled-facet output becomes highly asymmetry when the facet angle increases. This suggests that an AFTMF might be able to convert a two-lobe LP_{11} mode in the FMF into a single-lobe beam at the angled-facet output. Successful demonstration of LP mode down-conversion by an AFTMF can greatly simplify the setup of MDM de-multiplexer, where the LP_{11} mode can be directly converted into LP_{01} mode without additional optical components. This will lead to MDM de-multiplexer with small physical footprint. Besides, it is possible to extend this design for $LP_{21} \rightarrow LP_{11}$ mode down-conversion. In spite of that, the potential of AFTMF to function as a passive mode converter for down-conversion has never been explored. Therefore, investigation into the performance of AFTMF for LP mode down-conversion might lead to a useful mode converter. In addition, the investigation can provide better understanding on the effect of facet angle on the characteristic of the output mode profile.

When light propagates along an optical fiber, its power is distributed among several spatial modes in the fiber. The number of these spatial modes depends on the fiber's parameters (Buck, 2004). The polarisation and orientation of the spatial modes varies in the fiber due to imperfection in fiber or due to external perturbation on the fiber during the transmission. This phenomenon has been exploited to manipulate the polarisation of LP_{01} mode in SMF by using a three-paddle coil-based polarisation controller (PC) (Lefevre, 1980; Ulrich, Rashleigh, & Eickhoff, 1980). The SMF is bent and twisted by the PC to induce birefringence in the fiber. When the PC is tuned, the birefringence will be induced and this subsequently leads to the change in polarisation angle of the LP_{01} mode. From another point of view, tuning the PC has changed the power composition of LP_{01x} and LP_{01y} modes due to mode coupling. This consequently modifies the resultant polarisation angle of the LP_{01} mode. Such PC has provided a convenient way to control the polarisation state of LP_{01} in SMF.

Recently, Hong et al. has reported the use of FMF three-paddle coil-based PC to rotate the mode orientation and polarisation angle of LP_{11} mode in the FMF (Hong, Fu, Yu, Tang, & Liu, 2016). In another work, Cui et al. demonstrates the polarisation manipulation of LP_{01}, LP_{11a} and LP_{11b} modes in an elliptical core FMF with a coil-based PC (Cui et al., 2017). Despite that, literature on the use of coil-based PC employing FMF is scanty. Further investigation into such device will provide a valuable insight on the device for various applications in MDM system.

1.4 Objectives

The main objectives of this work are as follows:

(i) To fabricate fused silica BPP by using photolithography and dry etching technique.

(ii) To investigate the effect of BPP tilt angle on its $LP_{01} \rightarrow LP_{11}$ mode conversion performance.

(iii) To investigate $LP_{11} \rightarrow LP_{01}$ mode conversion performance of AFTMF.

(iv) To investigate the performance of a three-paddle coil-based polarisation controller for simultaneous polarisation manipulation of LP_{01} and LP_{11} modes in FMF.

1.5 Thesis Outline

This thesis is divided into six chapters as follows:

Chapter 1 starts with a brief introduction on the development in the field of telecommunication that leads to the demand for SDM technologies. Then, motivations that lead to the research work to be presented in this thesis are discussed. This is followed by the research objectives and outline of this thesis.

Chapter 2 presents the theoretical background of spatial modes in FMF. Besides, a review on the development of key SDM components will be presented.

Chapter 3 reports the details on the fabrication and characterisation of fused silica BPP. Then, the investigation on the mode conversion performance of a tilted BPP with different phase pattern thicknesses will be presented. In addition, a technique to estimate the mode purity of LP_{11} mode in an FMF based on one-dimensional (1-D) mode profile will be discussed.

Chapter 4 reports the simulation results of AFTMF with different facet angle. Based on the simulation results, an AFTMF was fabricated to experimentally verify its $LP_{11} \rightarrow LP_{01}$ mode conversion performance.

Chapter 5 reports the investigation on the polarisation manipulation performance of a three-paddle two-mode fiber polarisation controller.

Chapter 6 concludes the thesis and discusses the outlook of the works presented in this thesis.

CHAPTER 2: THEORY AND LITERATURE REVIEW

In this chapter, the analysis of light propagation in a step-index few-mode fiber (FMF) will be discussed in Section 2.1. Firstly, the electric and magnetic fields components of the propagating light in cylindrical coordinate (E_z, E_r, E_ϕ, H_z, H_r and H_ϕ) are obtained by solving the wave equations and Maxwell's curl equations in the fiber core and cladding regions. Then, the eigenvalue equation for the FMF will be deduced by applying the boundary conditions at the core and cladding boundary. Solutions of the eigenvalue equation are the exact modes that can be guided in a fiber (TE, TM, EH and HE modes). The exact modes supported by a fiber depends on the fiber parameters. Following that, the application of weakly guiding approximation in the eigenvalue equations that leads to linearly polarised (LP) modes will be discussed. Finally, the review on the SDM fibers, (de)multiplexers and amplifiers will be presented in Section 2.2.

2.1 Light Propagation in Few-Mode Fiber

Both ray optics and electromagnetic optics are fundamental tools for the analysis of light propagation in an optical fibers. In general, analysis by using ray optics is adequate if the wavelength of light is smaller than the dimension of the object with which the light interacts. For example, ray optics can conveniently be used to analyse propagation of visible or infrared light in a multimode fiber with core diameter more than a few tens of micrometres. However, when the diameter of the fiber core is reduced near to the wavelength of light as in the case of single-mode fiber and few-mode fiber, the wave nature of light becomes prominent and analysis by ray optics becomes inaccurate. In such case, electromagnetic optics is required where the analysis is performed by solving Maxwell's equations (Synder & Love, 1983). Nevertheless, ray diagram is often useful to provide qualitative illustration on the interpretation of wave equation solutions.

2.1.1 Exact Modes

When a light propagating in an optical fiber, its electric and magnetic fields are governed by the following wave equations:

$$\nabla^2\mathbf{E} + (nk)^2\mathbf{E} = 0 \tag{2.1}$$

$$\nabla^2\mathbf{H} + (nk)^2\mathbf{H} = 0 \tag{2.2}$$

where n is the refractive index (RI) of the propagation medium, $k = (2\pi)/\lambda$ is the free space wavenumber and λ is the free space wavelength. By solving the wave equations, characteristics of light along the fiber can be determined. For step-index fiber with core radius, a, the RI distribution is:

$$n = \begin{cases} n_1 & \text{for } r < a \\ n_2 & \text{for } r > a \end{cases} \tag{2.3}$$

The electric and magnetic vector fields in cylindrical coordinate system can be written as:

$$\mathbf{E} = E_r\hat{\boldsymbol{r}} + E_\phi\hat{\boldsymbol{\phi}} + E_z\hat{\mathbf{z}} \tag{2.4}$$

$$\mathbf{H} = H_r\hat{\boldsymbol{r}} + H_\phi\hat{\boldsymbol{\phi}} + H_z\hat{\mathbf{z}} \tag{2.5}$$

The Laplacian operator is:

$$\nabla^2 = \frac{1}{r}\frac{\partial}{\partial r}\left(r\frac{\partial}{\partial r}\right) + \frac{1}{r^2}\frac{\partial^2}{\partial \phi^2} + \frac{\partial^2}{\partial z^2} \tag{2.6}$$

By applying the Laplacian operator, the wave equations can be rewritten as follows:

$$\nabla^2\mathbf{E} + (nk)^2\mathbf{E} = \left(\nabla^2 E_r - \frac{2}{r^2}\frac{\partial E_\phi}{\partial \phi} - \frac{E_r}{r^2} + (nk)^2 E_r\right)\hat{\boldsymbol{r}} + \left(\nabla^2 E_\phi + \frac{2}{r^2}\frac{\partial E_r}{\partial \phi} - \frac{E_\phi}{r^2} + (nk)^2 E_\phi\right)\hat{\boldsymbol{\phi}} + (\nabla^2 E_z + (nk)^2 E_z)\hat{\boldsymbol{z}} = 0 \tag{2.7}$$

$$\nabla^2\mathbf{H} + (nk)^2\mathbf{H} = \left(\nabla^2 H_r - \frac{2}{r^2}\frac{\partial H_\phi}{\partial \phi} - \frac{H_r}{r^2} + (nk)^2 H_r\right)\hat{\boldsymbol{r}} + \left(\nabla^2 H_\phi + \frac{2}{r^2}\frac{\partial H_r}{\partial \phi} - \frac{H_\phi}{r^2} + (nk)^2 H_\phi\right)\hat{\boldsymbol{\phi}} + (\nabla^2 H_z + (nk)^2 H_z)\hat{\boldsymbol{z}} = 0 \tag{2.8}$$

Each of the vector components in equation (2.7) needs to be equal to zero in order to satisfy the equation. It can be seen that $\hat{\boldsymbol{r}}$ and $\hat{\boldsymbol{\phi}}$ components contain both E_r and E_ϕ but the $\hat{\boldsymbol{z}}$ component only contains E_z. Therefore, it is more convenient to solve the differential equation of $\hat{\boldsymbol{z}}$ component first to determine E_z. Similarly, the $\hat{\boldsymbol{z}}$ component in equation (2.8) can be solved to obtain H_z.

Solving the differential equation of the $\hat{\boldsymbol{z}}$ component in equations (2.7) and (2.8) gives E_z and H_z in the fiber core region as:

$$E_z = AJ_\nu(\kappa r)e^{j(\beta z + \nu\phi)} \tag{2.9}$$

$$H_z = BJ_\nu(\kappa r)e^{j(\beta z + \nu\phi)} \tag{2.10}$$

where $\kappa = \sqrt{(n_1 k)^2 - \beta^2}$, $J_\nu(\kappa r)$ is the ν-th order Bessel function of the first kind, j is the unit imaginary number, n_1 is the RI of the fiber core, ν is an integer and β is the propagation constant.

On the other hand, for cladding region, the expressions of E_z and H_z are:

$$E_z = CK_\nu(\gamma r)e^{j(\beta z+\nu\phi)} \tag{2.11}$$

$$H_z = DK_\nu(\gamma r)e^{j(\beta z+\nu\phi)} \tag{2.12}$$

where $\gamma = \sqrt{\beta^2 - (n_2 k)^2}$, $K_\nu(\gamma r)$ is the ν-th order modified Bessel function of the second kind and n_2 is the RI of the fiber cladding.

By applying the expression of E_z and H_z (equations (2.9) − (2.12)) in the following Maxwell's equations (equations (2.13) and (2.14)), E_r, E_ϕ, H_r and H_ϕ can be determined:

$$\nabla \times \mathbf{H} = -j\omega\epsilon\mathbf{E} \tag{2.13}$$

$$\nabla \times \mathbf{E} = j\omega\mu\mathbf{H} \tag{2.14}$$

where ω is the angular frequency, ϵ is the permittivity of the propagation medium and μ is the permeability of the propagation medium.

Firstly, the $\hat{\boldsymbol{r}}$, $\hat{\boldsymbol{\phi}}$ and $\hat{\boldsymbol{z}}$ components of the two equations in cylindrical coordinates are:

$$\frac{1}{r}\frac{\partial H_z}{\partial \phi} - \frac{\partial H_\phi}{\partial z} = -j\omega\epsilon E_{\boldsymbol{r}} \tag{2.15}$$

$$\frac{\partial H_r}{\partial z} - \frac{\partial H_z}{\partial r} = -j\omega\epsilon E_{\boldsymbol{\phi}} \tag{2.16}$$

$$\frac{1}{r}\frac{\partial (rH_\phi)}{\partial r} - \frac{1}{r}\frac{\partial H_r}{\partial \phi} = -j\omega\epsilon E_{\boldsymbol{z}} \tag{2.17}$$

$$\frac{1}{r}\frac{\partial E_z}{\partial \phi} - \frac{\partial E_\phi}{\partial z} = j\omega\epsilon H_{\boldsymbol{r}} \tag{2.18}$$

$$\frac{\partial E_r}{\partial z} - \frac{\partial E_z}{\partial r} = j\omega\epsilon H_{\boldsymbol{\phi}} \tag{2.19}$$

$$\frac{1}{r}\frac{\partial (rE_\phi)}{\partial r} - \frac{1}{r}\frac{\partial E_r}{\partial \phi} = j\omega\epsilon H_z \tag{2.20}$$

where equations (2.15) − (2.17) are corresponding to equation (2.13) while equations (2.18) – (2.20) are corresponding to equation (2.14). Solving equations (2.15) and (2.19) allows us to obtain E_r and H_ϕ in terms of E_z and H_z. On the other hand, we can obtain E_ϕ and H_r in terms of E_z and H_z by solving equations (2.16) and (2.18).

By using the relationship $\partial/\partial z = j\beta$, E_r, E_ϕ, H_r and H_ϕ can be expressed in terms of E_z and H_z as follows:

$$E_r = \frac{j}{K^2}\left(\beta\frac{\partial E_z}{\partial r} + \omega\mu\frac{1}{r}\frac{\partial H_z}{\partial \phi}\right) \tag{2.21}$$

$$E_\phi = \frac{j}{K^2}\left(\frac{\beta}{r}\frac{\partial E_z}{\partial \phi} - \omega\mu\frac{\partial H_z}{\partial r}\right) \tag{2.22}$$

$$H_r = \frac{j}{K^2}\left(-\omega\epsilon\frac{1}{r}\frac{\partial E_z}{\partial \phi} + \beta\frac{\partial H_z}{\partial r}\right) \tag{2.23}$$

$$H_\phi = \frac{j}{K^2}\left(\omega\epsilon\frac{\partial E_z}{\partial r} + \frac{\beta}{r}\frac{\partial H_z}{\partial \phi}\right) \tag{2.24}$$

where

$$K^2 = \begin{cases} \kappa^2 = (n_1k)^2 - \beta^2 & for\, r < a \\ \gamma^2 = \beta^2 - (n_2k)^2 & for\, r > a \end{cases} \tag{2.25}$$

$$\epsilon = \begin{cases} \epsilon_1 & for\, r < a \\ \epsilon_2 & for\, r > a \end{cases} \tag{2.26}$$

Substituting equations (2.9) − (2.12), (2.25) and (2.26) into equations (2.21) − (2.24), the fields in core and cladding regions are as follows:

Core region:

$$E_r = \frac{j}{\kappa^2}\left(A\beta\kappa J_\nu'(\kappa r) + B\omega\mu\frac{j\nu}{r}J_\nu(\kappa r)\right) \tag{2.27}$$

$$E_\phi = \frac{j}{\kappa^2}\left(A\frac{\beta}{r}j\nu J_\nu(\kappa r) - B\omega\mu\kappa J_\nu'(\kappa r)\right) \tag{2.28}$$

$$H_r = \frac{j}{\kappa^2}\left(-A\omega\epsilon_1\frac{j\nu}{r}J_\nu(\kappa r) + B\beta\kappa\, J_\nu'(\kappa r)\right) \tag{2.29}$$

$$H_\phi = \frac{j}{\kappa^2}\left(A\omega\epsilon_1\kappa\, J_\nu'(\kappa r) + B\frac{\beta}{r}j\nu J_\nu(\kappa r)\right) \tag{2.30}$$

Cladding region:

$$E_r = \frac{-j}{\gamma^2}\left(C\beta\gamma K_\nu'(\gamma r) + D\omega\mu\frac{j\nu}{r}K_\nu(\gamma r)\right) \tag{2.31}$$

$$E_\phi = \frac{-j}{\gamma^2}\left(C\frac{\beta}{r}j\nu K_\nu(\gamma r) - D\omega\mu\gamma K_\nu'(\gamma r)\right) \tag{2.32}$$

$$H_r = \frac{-j}{\gamma^2}\left(-C\omega\epsilon_2\frac{j\nu}{r}K_\nu(\gamma r) + D\beta\gamma K_\nu'(\gamma r)\right) \tag{2.33}$$

$$H_\phi = \frac{-j}{\gamma^2}\left(C\omega\epsilon_2\gamma K_\nu'(\gamma r) + D\frac{\beta}{r}j\nu K_\nu(\gamma r)\right) \tag{2.34}$$

Next, we need to determine the coefficients in equations (2.27) − (2.34), namely *A*, *B*, *C* and *D* by applying the boundary condition at the core-cladding interface of the fiber. The tangential components of **E** and **H** (E_z, H_z, E_ϕ and H_ϕ) should be continuous at $r = a$ in order to satisfy the boundary condition. Based on equations (2.9) − (2.12), the following relationships are obtained:

$$E_{z,core} = E_{z,cladding}$$

$$AJ_\nu(\kappa a)e^{j(\beta z+\nu\phi)} = CK_\nu(\gamma a)e^{j(\beta z+\nu\phi)}$$

$$AJ_\nu(\kappa a) = CK_\nu(\gamma a)$$

$$C = \frac{J_\nu(\kappa a)}{K_\nu(\gamma a)}A \tag{2.35}$$

$$H_{z,core} = H_{z,cladding}$$

$$BJ_\nu(\kappa a)e^{j(\beta z+\nu\phi)} = DK_\nu(\gamma a)e^{j(\beta z+\nu\phi)}$$

$$BJ_\nu(\kappa a) = DK_\nu(\gamma a)$$

$$D = \frac{J_\nu(\kappa a)}{K_\nu(\gamma a)}B \tag{2.36}$$

By substituting equations (2.35) and (2.36) into equations (2.32) and (2.34), we will obtain E_ϕ and H_ϕ in terms of A and B. Due to the field continuity at $r = a$:

$$E_{\phi,core} = E_{\phi,cladding} \tag{2.37}$$

$$H_{\phi,core} = H_{\phi,cladding} \tag{2.38}$$

Substituting the corresponding E_ϕ and H_ϕ in terms of A and B into equations (2.37) and (2.38) will give:

$$A\beta\nu\left(\frac{1}{(\kappa a)^2}+\frac{1}{(\gamma a)^2}\right)+jB\omega\mu\left(\frac{J_\nu'(\kappa a)}{\kappa a J_\nu(\kappa a)}+\frac{K_\nu'(\gamma a)}{\gamma a K_\nu(\gamma a)}\right)=0 \tag{2.39}$$

$$A\omega\left(\frac{\epsilon_1 J_\nu'(\kappa a)}{\kappa a J_\nu(\kappa a)}+\frac{\epsilon_2 K_\nu'(\gamma a)}{\gamma a K_\nu(\gamma a)}\right)+jB\beta\nu\left(\frac{1}{(\kappa a)^2}+\frac{1}{(\gamma a)^2}\right)=0 \tag{2.40}$$

Equations (2.39) and (2.40) can be written in matrix form as follows:

$$\begin{bmatrix} \beta\nu\left(\frac{1}{(\kappa a)^2}+\frac{1}{(\gamma a)^2}\right) & j\omega\mu\left(\frac{J_\nu'(\kappa a)}{\kappa a J_\nu(\kappa a)}+\frac{K_\nu'(\gamma a)}{\gamma a K_\nu(\gamma a)}\right) \\ \omega\left(\frac{\epsilon_1 J_\nu'(\kappa a)}{\kappa a J_\nu(\kappa a)}+\frac{\epsilon_2 K_\nu'(\gamma a)}{\gamma a K_\nu(\gamma a)}\right) & j\beta\nu\left(\frac{1}{(\kappa a)^2}+\frac{1}{(\gamma a)^2}\right) \end{bmatrix}\begin{bmatrix} A \\ B \end{bmatrix}=\begin{bmatrix} 0 \\ 0 \end{bmatrix} \tag{2.41}$$

To obtain nontrivial solutions for A and B, the determinant of the coefficient matrix needs to be zero:

$$\begin{vmatrix} \beta\nu\left(\frac{1}{(\kappa a)^2}+\frac{1}{(\gamma a)^2}\right) & j\omega\mu\left(\frac{J_\nu'(\kappa a)}{\kappa a J_\nu(\kappa a)}+\frac{K_\nu'(\gamma a)}{\gamma a K_\nu(\gamma a)}\right) \\ \omega\left(\frac{\epsilon_1 J_\nu'(\kappa a)}{\kappa a J_\nu(\kappa a)}+\frac{\epsilon_2 K_\nu'(\gamma a)}{\gamma a K_\nu(\gamma a)}\right) & j\beta\nu\left(\frac{1}{(\kappa a)^2}+\frac{1}{(\gamma a)^2}\right) \end{vmatrix}=0$$

$$\begin{aligned}&\left[\beta\nu\left(\frac{1}{(\kappa a)^2}+\frac{1}{(\gamma a)^2}\right)\right]\left[j\beta\nu\left(\frac{1}{(\kappa a)^2}+\frac{1}{(\gamma a)^2}\right)\right]\\ &\quad-\left[j\omega\mu\left(\frac{J_\nu'(\kappa a)}{\kappa a J_\nu(\kappa a)}+\frac{K_\nu'(\gamma a)}{\gamma a K_\nu(\gamma a)}\right)\right]\left[\omega\left(\frac{\epsilon_1 J_\nu'(\kappa a)}{\kappa a J_\nu(\kappa a)}+\frac{\epsilon_2 K_\nu'(\gamma a)}{\gamma a K_\nu(\gamma a)}\right)\right]=0\end{aligned}$$

$$\left[\beta\nu\left(\frac{1}{(\kappa a)^2}+\frac{1}{(\gamma a)^2}\right)\right]^2 - \omega^2\mu\left(\frac{J_\nu'(\kappa a)}{\kappa a J_\nu(\kappa a)}+\frac{K_\nu'(\gamma a)}{\gamma a K_\nu(\gamma a)}\right)\left(\frac{\epsilon_1 J_\nu'(\kappa a)}{\kappa a J_\nu(\kappa a)}+\frac{\epsilon_2 K_\nu'(\gamma a)}{\gamma a K_\nu(\gamma a)}\right) = 0 \tag{2.42}$$

By applying the relationships of $n^2 = \epsilon/\epsilon_0$, $c = \lambda f = (\mu\epsilon_0)^{-0.5}$, $\omega = 2\pi f$ and $k = (2\pi)/\lambda$, equation (2.42) can be rewritten as:

$$\left(\frac{J_\nu'(\kappa a)}{\kappa a J_\nu(\kappa a)}+\frac{K_\nu'(\gamma a)}{\gamma a K_\nu(\gamma a)}\right)\left(\frac{J_\nu'(\kappa a)}{\kappa a J_\nu(\kappa a)}+\left(\frac{n_2}{n_1}\right)^2\frac{K_\nu'(\gamma a)}{\gamma a K_\nu(\gamma a)}\right) = \left[\frac{\beta\nu}{n_1 k}\left(\frac{1}{(\kappa a)^2}+\frac{1}{(\gamma a)^2}\right)\right]^2 \tag{2.43}$$

Equation (2.43) is known as the eigenvalue equation of step-index fiber. The equation will allow us to determine the parameters under which guided modes can occur in the fiber. The terms κa and γa are related to the normalised frequency, V by the following equation:

$$V^2 = (\kappa a)^2 + (\gamma a)^2 \tag{2.44}$$

where

$$V = ka\sqrt{n_1^2 - n_2^2} \tag{2.45}$$

When equations (2.43) and (2.44) are plotted in a graph of γa vs κa, intersects between the curves give the values of γa and κa which are the solutions that satisfy the boundary condition of the step-index fiber with specific operation parameters (RI of core and cladding, core radius and operating wavelength). Then, the value of β can be determined from the values of γ and κ based on equation (2.25). More than one value for β could be obtained when there is more than one guided mode. This way to obtain the value of β is known as the graphical method. In the following sub-sections, the eigenvalue equation will be analysed for the cases of $v = 0$ and $v \neq 0$ which will lead us to the four exact modes in step-index fiber, namely, TE, TM, EH and HE modes.

2.1.1.1 Meridional Modes (v = 0)

When $v = 0$, the ϕ-dependent factor in the solutions of wave equations becomes constant. Therefore, the corresponding guided modes are meridional modes which do not have ϕ variation. At the same time, the right-hand side of equation (2.43) becomes zero and the equation reduces to:

$$\left(\frac{J_v'(\kappa a)}{\kappa a J_v(\kappa a)} + \frac{K_v'(\gamma a)}{\gamma a K_v(\gamma a)}\right) = 0 \tag{2.46}$$

and

$$\left(\frac{J_v'(\kappa a)}{\kappa a J_v(\kappa a)} + \left(\frac{n_2}{n_1}\right)^2 \frac{K_v'(\gamma a)}{\gamma a K_v(\gamma a)}\right) = 0 \tag{2.47}$$

where $J_0'(x) = -J_1(x)$ and $K_0'(x) = -K_1(x)$ were applied. It can be shown that equations (2.46) and (2.47) are the eigenvalue equations corresponding to TE ($E_z = 0$) and TM ($H_z = 0$) modes in the step-index fiber respectively (IIzuka, 2002). By using the graphical method described in previous section, intersects between equations (2.44) and (2.46) as well as that between equations (2.44) and (2.47) will allow us to determine the TE and TM modes supported by a step-index fiber. TE and TM modes of different orders are designated by $TE_{v\mu}$ and $TM_{v\mu}$ respectively where $v = 0$ and $\mu = 1, 2, 3\ldots$ The TE and TM modes of different orders are corresponding to different sets of γ and κ that satisfy equations (2.46) and (2.47).

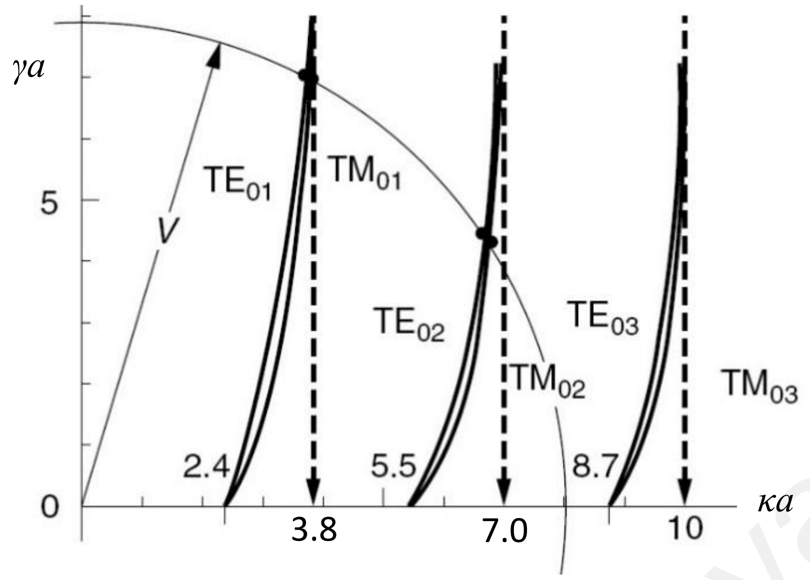

Figure 2.1: Relationship between *γa* and *κa* for the case of *v* = 0. (IIzuka, 2002)

Figure 2.1 shows an example of the curves for equations (2.44), (2.46) and (2.47) plotted in γa vs κa graph. From the figure, the curve of equation (2.44) intersects with that of eigenvalue equation corresponding to TE_{01}, TM_{01}, TE_{02} and TM_{02} modes. Therefore, these four modes can be guided in the fiber. It can be seen that the eigenvalue equations curves cross $\gamma a = 0$ at $\kappa a = 2.4$, 5.5 and 8.7. These are the cutoff values of the modes in which the corresponding TE and TM modes will only be guided if κa is larger than the cutoff values. For example, TE_{02} and TM_{02} modes will only be guided if $\kappa a > 5.5$. When $\kappa a < 5.5$, only TE_{01} and TM_{01} modes are guided in the fiber. At cutoff values, TE and TM modes become degenerate. It should be noted that there are regions along the κa axis at which the TE and TM modes do not exist because the values of κa in those regions do not satisfy equation (2.46) or (2.47). For example, $3.8 < \kappa a < 5.5$ and $7.0 < \kappa a < 8.7$. The difference in the curves of TE and TM modes is due to the $(n_2/n_1)^2$ factor in equation (2.47) as compared to equation (2.46). However, the difference is small because the factor is close to unity in most cases.

2.1.1.2 Skew Modes ($v \neq 0$)

If $v \neq 0$, the solutions of wave equations have ϕ variation and skew modes are excited in the fiber. The weakly guiding approximation is used to simplify equation (2.43) in order to obtain the solutions for the equation when $v \neq 0$. The approximation can be assumed when $n_2 \approx n_1$. The guided modes in a step-index fiber satisfy the relationship $n_2k < \beta < n_1k$. Under weakly guiding approximation, $n_1k \approx n_2k \approx \beta$ and $(n_2/n_1) \approx 1$. Therefore, equation (2.43) can be simplified to:

$$\frac{J_v'(\kappa a)}{\kappa a J_v(\kappa a)} + \frac{K_v'(\gamma a)}{\gamma a K_v(\gamma a)} = \pm v\left(\frac{1}{(\kappa a)^2} + \frac{1}{(\gamma a)^2}\right) \tag{2.48}$$

When the right-hand side of the eigenvalue equation has + sign, the modes corresponding to the solution of the equation is called EH modes. On the other hand, if the sign is negative, the modes corresponding to the solution is known as HE modes. These modes are called the hybrid modes because they contain both E_z and H_z components. In contrast, E_z and H_z are zero in the cases of TE and TM modes. EH and HE modes of different orders are designated by $EH_{v\mu}$ and $HE_{v\mu}$ respectively where v, μ = 1, 2, 3… The integer μ represents the μ-th solution of the corresponding eigenvalue equation.

Equations (2.49) − (2.52) show the Bessel function recurrence formulas:

$$J_v'(x) = J_{v-1}(x) - \frac{v}{x}J_v(x) \tag{2.49}$$

$$K_v'(x) = -K_{v-1}(x) - \frac{v}{x}K_v(x) \tag{2.50}$$

$$J_v'(x) = -J_{v+1}(x) + \frac{v}{x}J_v(x) \tag{2.51}$$

$$K_v'(x) = -K_{v+1}(x) + \frac{v}{x}K_v(x) \tag{2.52}$$

By applying equations (2.49) and (2.50) in equation (2.48), we will obtain the eigenvalue equation of the HE modes. On the other hand, applying equations (2.51) and (2.52) in equation (2.48) will give us the eigenvalue equation for EH modes. The equations are shown below where equations (2.53) and (2.54) are corresponding to HE and EH modes respectively:

$$\frac{J_{\nu-1}(\kappa a)}{\kappa a J_{\nu}(\kappa a)} - \frac{K_{\nu-1}(\gamma a)}{\gamma a K_{\nu}(\gamma a)} = 0 \tag{2.53}$$

$$\frac{J_{\nu+1}(\kappa a)}{\kappa a J_{\nu}(\kappa a)} + \frac{K_{\nu+1}(\gamma a)}{\gamma a K_{\nu}(\gamma a)} = 0 \tag{2.54}$$

When $v = 1$, equation (2.53) can be simplified to:

$$\frac{J_0(\kappa a)}{\kappa a J_1(\kappa a)} - \frac{K_0(\gamma a)}{\gamma a K_1(\gamma a)} = 0 \tag{2.55}$$

It can be shown from equation (2.55) that the cutoff values for HE modes are $\kappa a = 0$, 3.83, 7.02, 10.2… Figure 2.2 depicts the curves of equations (2.44) and (2.55) plotted in γa vs κa graph for HE modes with $v = 1$. The cutoff values of the $HE_{1\mu}$ modes are shown in the figure. When $v \geq 2$, equation (2.53) can be rewritten as follows:

$$\frac{J_{\nu-1}(\kappa a)}{\kappa a J_{\nu-2}(\kappa a)} + \frac{K_{\nu-1}(\gamma a)}{\gamma a K_{\nu-2}(\gamma a)} = 0 \tag{2.56}$$

In this case, the cutoff values for the HE modes are $\kappa a = 2.4$, 5.52, 8.65…

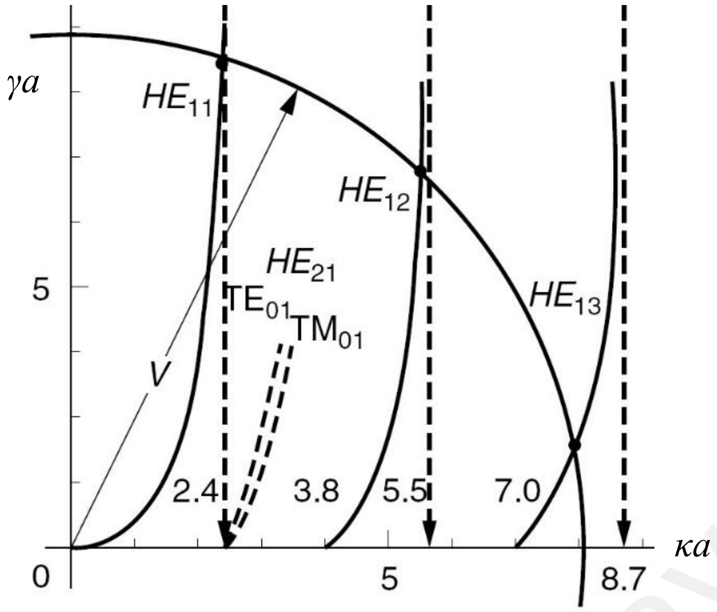

Figure 2.2: Relationship between *γa* and *κa* for the case of *v* ≠ 0. (IIzuka, 2002)

In the above discussion, the modes guided by a step-index fiber are determined from the intersection between equation (2.44) and the curves of eigenvalue equations plotted in the graph of *γa* vs *κa*. The eigenvalue equations can be written in terms of *b* and *V* instead of *γa* and *κa* by defining the normalised propagation constant, *b* as follows:

$$b = \left(\frac{\gamma a}{V}\right)^2 \tag{2.57}$$

From equations (2.44) and (2.56), *κa* can be written in terms of *b* and *V* as:

$$\kappa a = \sqrt{(1-b)}\,V \tag{2.58}$$

From equations (2.25) and (2.57), the relationship between *β* and *b* is given as follows:

$$\beta^2 = (n_1 k)^2[1 - 2\Delta(1-b)] \tag{2.59}$$

where $\Delta = (n_1 - n_2)/n_1$. By using binomial expansion, equation (2.59) can be simplified to:

$$\beta = n_1 k[1 - \Delta(1-b)] \tag{2.60}$$

Then, the eigenvalue equations in terms of b and V can be solved numerically under the constraint of equation (2.44) to obtain the graph of b vs V as shown in Figure 2.3. This graph provides a convenient mean to determine the mode(s) guided in a fiber by knowing the value of V corresponding to the operation parameters. There is a cutoff value of V corresponding to each mode which is denoted as V_c. When V is larger than V_c of the respective mode, the mode will be guided in the fiber. For example, $V_c = 0$ for HE_{11} mode while $V_c \sim 2.4$ for TE_{01}, TM_{01} and HE_{21} modes. When $0 < V < 2.4$, only HE_{11} mode can be guided in the step-index fiber. This is the condition to achieve single-mode operation. For $V \geq 2.4$, higher-order modes (HOMs) can be guided in the fiber core.

Figure 2.4 shows the number of possible modes, N that can be guided in a step-index fiber when V increases from zero to six. For example, when $0 < V < 3.8$, the fiber can guide TE_{01}, TM_{01} and HE_{21} modes other than the HE_{11} mode. Therefore, the number of possible modes that can be guided by the fiber is 4. From equation (2.45), for a step-index fiber with a fixed n_1, n_2 and a, the value of V can be adjusted by changing the wavelength of the propagating light.

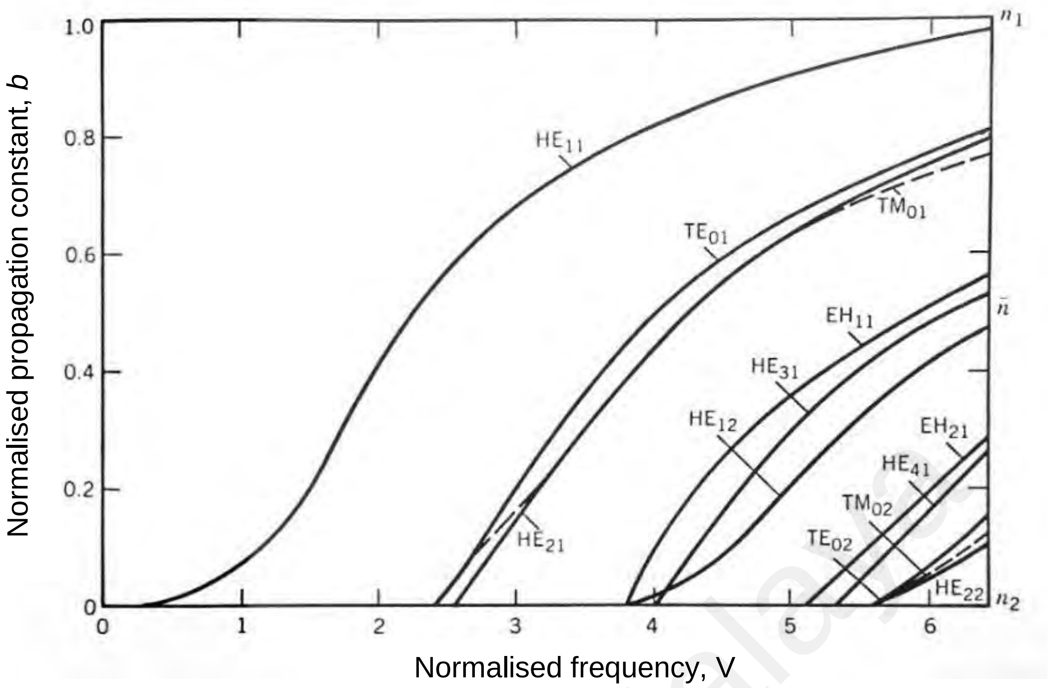

Figure 2.3: Relationship between normalised propagation constant, *b* and *V*-number for different exact modes. (Agrawal, 1997)

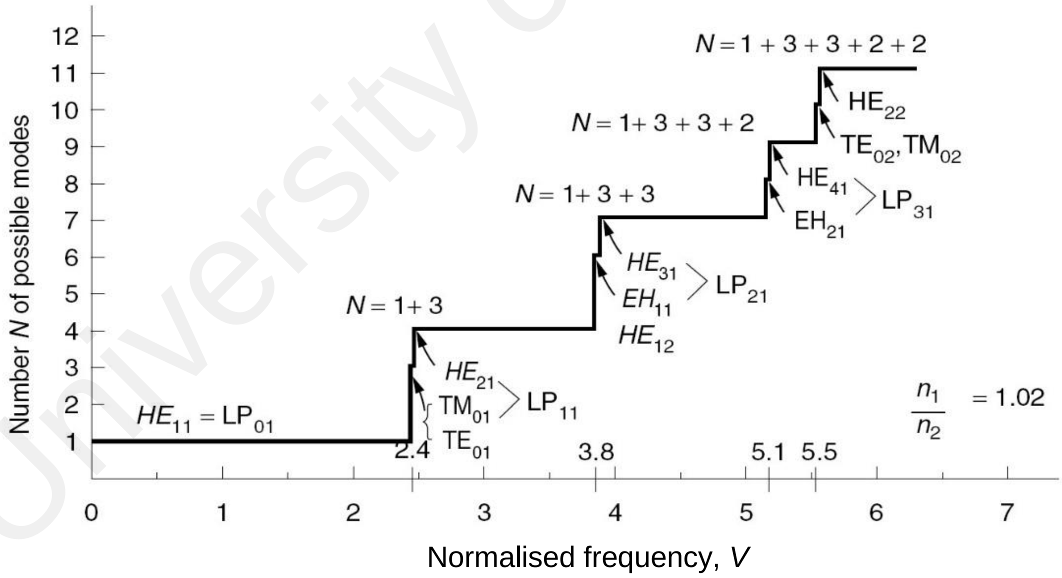

Figure 2.4: The number of possible modes at different *V*-number. (IIzuka, 2002)

2.1.2 Linearly Polarised Modes (LP Modes)

By applying $m = v - 1$ in equation (2.53) and $m = v + 1$ in equation (2.54), the equations can be rewritten as follows:

$$\frac{J_m(\kappa a)}{\kappa a J_{m+1}(\kappa a)} - \frac{K_m(\gamma a)}{\gamma a K_{m+1}(\gamma a)} = 0 \tag{2.61}$$

$$\frac{J_m(\kappa a)}{\kappa a J_{m-1}(\kappa a)} + \frac{K_m(\gamma a)}{\gamma a K_{m-1}(\gamma a)} = 0 \tag{2.62}$$

Then, moves the second terms of equations (2.61) and (2.62) to the right-hand side, inverting both sides and applying the recurrence formulas given by equations (2.63) and (2.64), it can be shown that the eigenvalue equations for $HE_{m+1,\mu}$ and $EH_{m-1,\mu}$ modes are identical.

$$J_{m+1}(x) + J_{m-1}(x) = \frac{2v}{x} J_m(x) \tag{2.63}$$

$$K_{m+1}(x) - K_{m-1}(x) = \frac{2v}{x} K_m(x) \tag{2.64}$$

The subscript of $HE_{m+1,\mu}$ and $EH_{m-1,\mu}$ was assigned by taking $v = m + 1$ for $HE_{v\mu}$ mode and $v = m + 1$ for $EH_{v\mu}$ mode. Under the weakly guiding approximation, $TE_{0\mu}$, $TM_{0\mu}$, $HE_{m+1,\mu}$ and $EH_{m-1,\mu}$ modes with identical eigenvalue equation can be categorised under the same mode group known as linearly polarised mode or $LP_{m\mu}$ mode. Typically, weakly guiding approximation is applied to fiber with relative index difference, $\Delta = (n_1 - n_2)/n_1$, less than 10^{-2}. Table 2.1 summarises the exact modes in each LP mode group. Although the exact modes grouped under the same LP mode share the same eigenvalue equation, their propagation constants are not exactly the same. For example, there is a slight variation in the propagation constant of HE_{21}, TE_{01} and TM_{01} grouped under LP_{11} mode as shown in Figure 2.3.

Table 2.1: LP modes and their corresponding exact modes and eigenvalue equations.

LP mode ($\mu \geq 1$)	**Eigenmode ($\mu \geq 1$)**	**Eigenvalue equation**
$LP_{0\mu}$ mode (m = 0)	$HE_{1\mu}$ mode	$\frac{J_0(\kappa a)}{\kappa a J_1(\kappa a)} - \frac{K_0(\gamma a)}{\gamma a K_1(\gamma a)} = 0$
$LP_{1\mu}$ mode (m = 1)	$TE_{0\mu}$ mode $TM_{0\mu}$ mode $HE_{2\mu}$ mode	$\frac{J_1(\kappa a)}{\kappa a J_0(\kappa a)} + \frac{K_1(\gamma a)}{\gamma a K_0(\gamma a)} = 0$
$LP_{m\mu}$ mode (m ≥ 2)	$EH_{m-1,\mu}$ mode $HE_{m+1,\mu}$ mode	$\frac{J_m(\kappa a)}{\kappa a J_{m-1}(\kappa a)} + \frac{K_m(\gamma a)}{\gamma a K_{m-1}(\gamma a)} = 0$

By using the eigenvalue equations given in Table 2.1, graphical method as discussed in the previous section can be used to determine the LP mode(s) supported by a step-index fiber. Figure 2.5 shows the relation between γa and κa for different LP modes. In the same graph, the circular curve corresponding to equation (2.44) also can be seen. Similarly, by numerically solving the eigenvalue equation of LP modes under the constraint of equation (2.44), the graph of b vs V can be plotted for LP modes. This is shown in Figure 2.6. From Figure 2.5 and Figure 2.6, the cutoff value of κa or V corresponding to the LP modes can be determined.

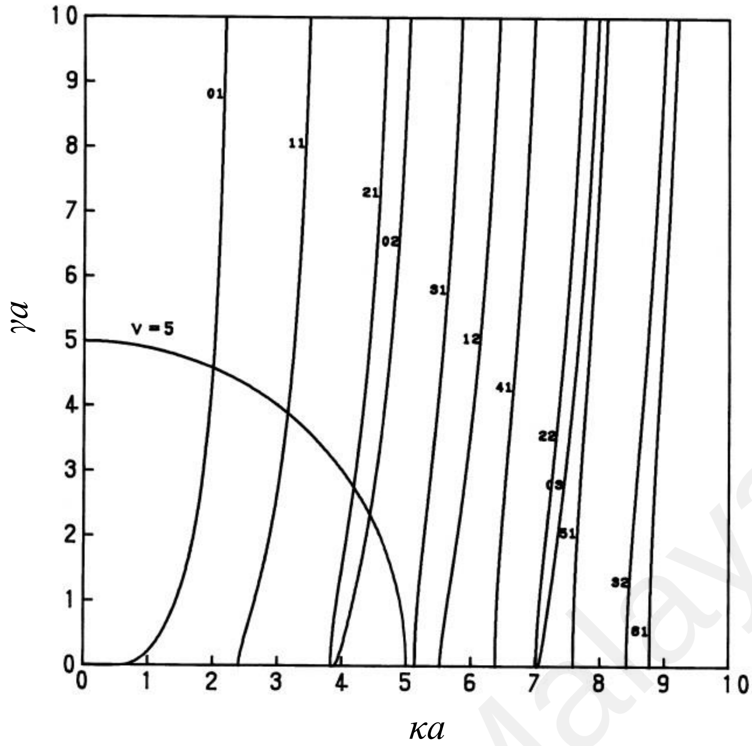

Figure 2.5: Relationship between *γa* and *κa* for LP modes. (Okamoto, 2006)

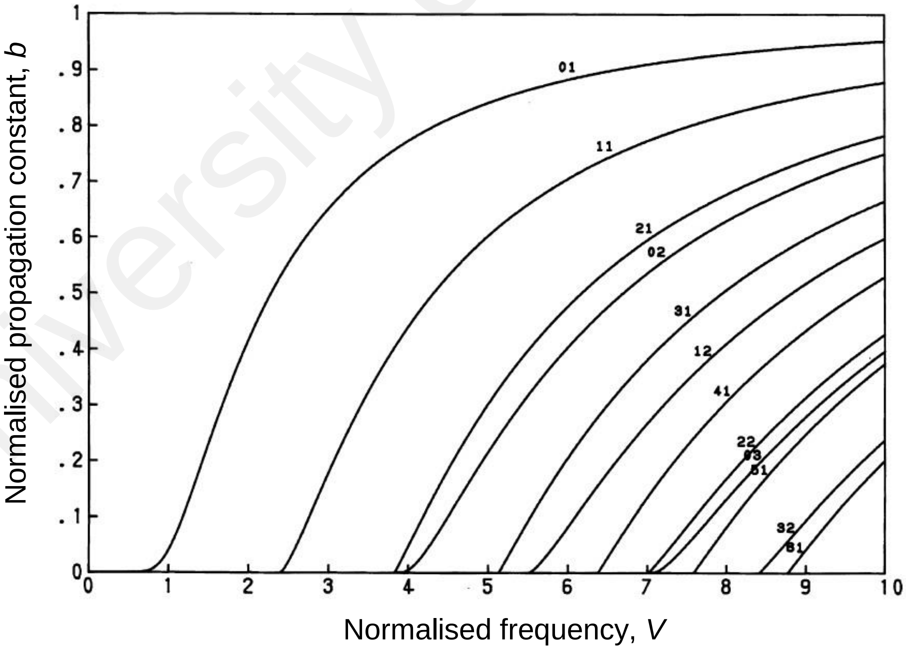

Figure 2.6: Relationship between normalised propagation constant, *b* and *V*-number for different LP modes. (Okamoto, 2006)

2.1.2.1 Intensity and Polarisation Profile of LP Modes

The intensity profiles of $\mathrm{LP}_{m\mu}$ modes can be described using the following general equations (Buck, 2004):

$$I_{m\mu} = \begin{cases} I_0 J_m^2\left(\frac{ur}{a}\right) cos^2(m\phi) & r \leq a \\ I_0\left(\frac{J_m(\kappa a)}{K_m(\gamma a)}\right)^2 K_m^2\left(\frac{wr}{a}\right) cos^2(m\phi) & r \geq a \end{cases} \tag{2.65}$$

where I_0 is the peak intensity. LP mode can be treated as the superposition of the corresponding exact modes in a fiber. Different ways of adding the exact modes might lead to degenerated LP modes having different orientation in terms of polarisation and intensity profile. For example, four degenerated LP_{11} modes shown in Figure 2.7 can be obtained as a result of the superposition associated with TM_{01}, TE_{01}, HE_{21}^{even} and HE_{21}^{odd} modes. The intensity and polarisation profiles of the exact modes are shown in Figure 2.8.

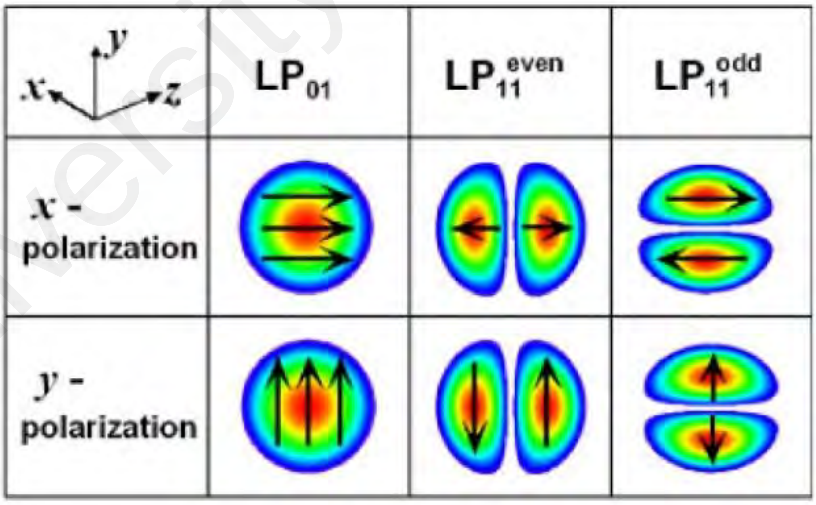

Figure 2.7: Intensity and polarisation profiles of LP_{01} and LP_{11} modes. (Kokubun, 2018)

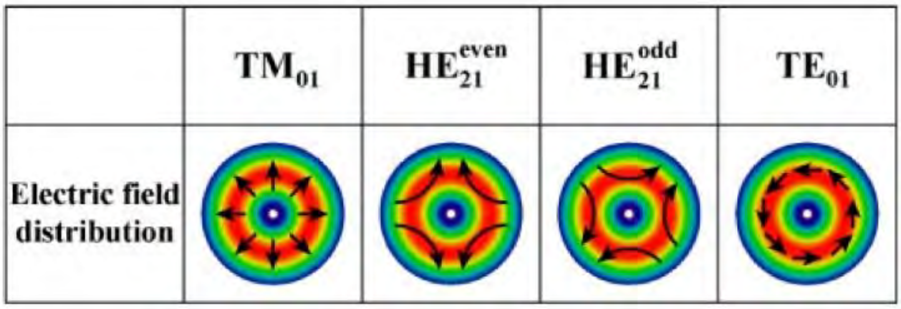

Figure 2.8: Intensity and polarisation profiles of the exact modes corresponding to LP_{11} mode. (Kokubun, 2018)

As discussed earlier, the graphical or numerical solution of the eigenvalue equation under the constraint of equation (2.44) allows us to obtain the values of γa and κa that satisfied the boundary condition of a step-index fiber. More than one set of solutions for γa and κa can be obtained when the fiber can support more than one LP mode as shown in Figure 2.5. By applying the values of γ and κ in equation (2.25), β corresponding to different LP modes supported by the fiber can be determined. Meanwhile, it is also possible to determine β from b by using equation (2.59) or (2.60) if the value of b is known. As seen in Figure 2.6, at a specific V, different LP modes have different value of b in the range of $0 - 1$. In general, lower-order mode has larger value in b as compared to HOMs.

Besides the propagation constant, each LP mode has its own effective RI, or simply effective index, n_{eff}. The effective index is related to the propagation constant by the following equation:

$$n_{\text{eff}} = \frac{\beta}{k} = \beta \frac{2\pi}{\lambda} \tag{2.66}$$

where k is the free space wavenumber and λ is the free space wavelength. Since different exact modes have slightly different propagation constant, they propagate at a different phase velocity and their relative phase difference changes during the propagation. This is known as the modal birefringence (Kogelnik & Winzer, 2012). As the LP modes are superposition of the corresponding exact modes, the change in the relative phase difference will lead to the change in the LP modes' intensity and polarisation profiles. For example, LP_{11y}^{odd} mode is the superposition of TM_{01} and HE_{21}^{even} modes. When it is excited in an FMF, the LP_{11y}^{odd} mode will evolve back and forth between LP_{11y}^{odd} and LP_{11x}^{even} modes while propagating along the FMF due to the change in the relative phase difference between the TM_{01} and HE_{21}^{even} modes (Kokubun, 2018). LP_{11y}^{odd} mode is obtained when TM_{01} and HE_{21}^{even} modes are in-phase while LP_{11x}^{even} mode is obtained when the exact modes are out-of-phase by π.

2.2 Key Components for Space-Division Multiplexing System

Ever since the SDM technology started to receive growing research interest a decade ago, new transmission records in terms of capacity and distance have been achieved in laboratories over the years. At the same time, performance of the optical fiber, (de)multiplexer and amplifier for SDM system have been refined to deal with various challenges such as modal crosstalk, differential mode delay (DMD), mode dependent loss (MDL) and insertion loss. The ultimate goal is to boost the transmission capacity of the optical fiber communication network by using feasible and economically attractive solution. The following sections will review the progress in the development of the optical fibers (FMF, MCF and MC-FMF), (de)multiplexers and amplifiers for SDM system.

2.2.1 SDM Fibers

Generally, the SDM fibers are weakly-guided (core-cladding index contrast < 10^{-2}). Therefore, the propagating spatial modes in these fibers can be treated as LP modes and analysed using the well-established theory of LP modes. Figure 2.9 shows a few examples of LP modes.

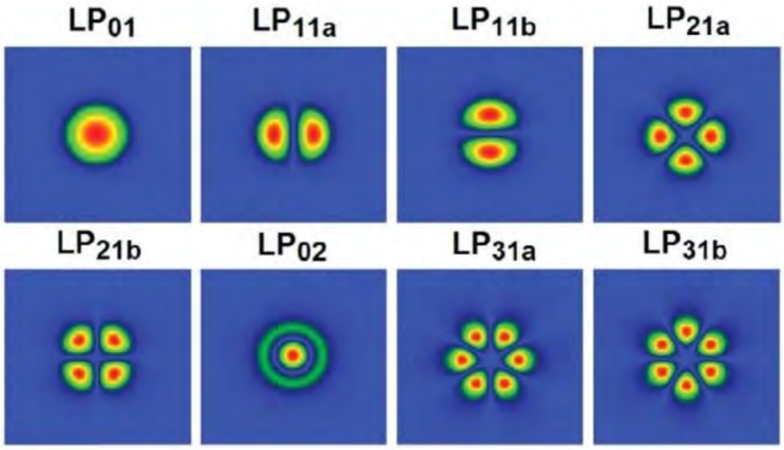

Figure 2.9: Profile of several LP modes. (Weng, He, & Pan, 2017)

Various SDM fibers have been proposed and developed to satisfy the requirements for SDM transmission (Kasahara et al., 2013; Kitayama & Diamantopoulos, 2017; Morioka et al., 2012; Saitoh & Matsuo, 2016; Sillard, 2011, 2015; Sillard, Bigot-Astruc, & Molin, 2014). Figure 2.10 shows some examples of SDM fiber cross-sections for LP modes. Generally, these fibers can be categorised into six groups labelled as A-I, A-II, A-III, B-I, B-II and B-III in the figure.

For fibers in group I and III (A-I, A-III, B-I and B-III), the total number of core in each fiber is denoted as *n* while *m* represents the total number of mode supported by each core. On the other hand, fibers in group II (A-II and B-II) operate based on the coupled-core approach where several closely positioned single-mode cores form a coupled-core to perform signal transmission. For these fibers, *n* represents the number of coupled-core in the fiber where each coupled-core is composed of several single-mode cores. Meanwhile, the number of modes supported by each coupled-core is denoted as *m*.

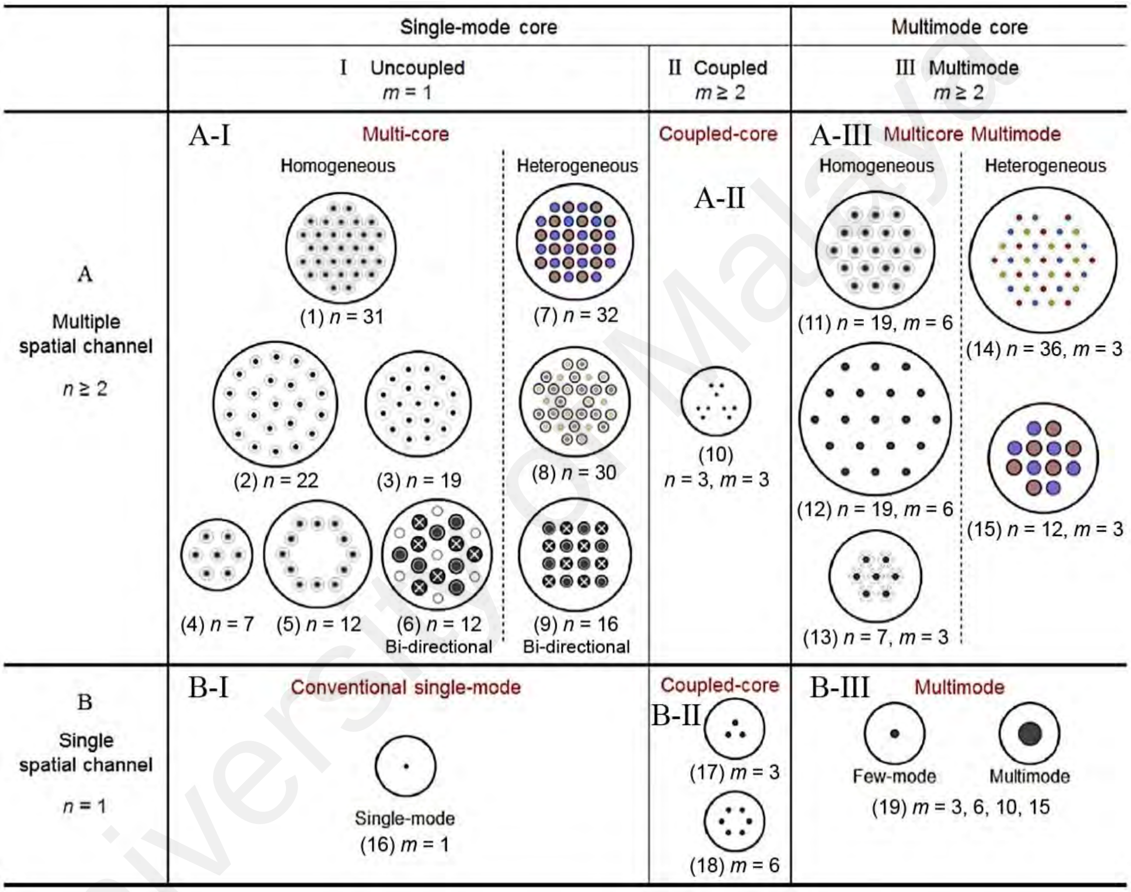

Figure 2.10: Cross-sections of various types of FMF, MMF and MCF. (Mizuno & Miyamoto, 2017)

Group A-I, A-II, A-III and B-II consisted of various types of MCFs. Heterogeneous MCFs have cores with different RI profiles as compared to homogeneous MCFs which have cores with identical RI profile. Employing cores with different RI profiles has been found to reduce the inter-core crosstalk due to the difference in propagation constant of LP modes propagate in adjacent cores.

Besides that, there are several other approaches to suppress inter-core crosstalk, for instance: (i) trench structure around the cores (Takenaga et al., 2011), (ii) air holes around the cores (Uden et al., 2014), (iii) reducing the number of adjacent cores (Matsuo et al., 2012; Takara et al., 2012; Takenaga, Matsuo, Saitoh, & Koshiba, 2013), (iv) employing non-uniform core spacing in MCF (Sakaguchi et al., 2014) and (v) propagation direction interleaving (PDI) configuration (Arikawa, Ito, Gabory, & Fukuchi, 2015; Kobayashi et al., 2013; A. Sano et al., 2013; A. Sano, Takara, Kobayashi, & Miyamoto, 2014).

In PDI configuration, a few of the adjacent cores propagate light in the opposite direction to reduce inter-core crosstalk. Meanwhile, it has been suggested that the coupled-core approach (group A-II and B-II) can reduce the DMD and MDL during the transmission (G. Li et al., 2014; Ryf, Essiambre, Gnauck, et al., 2012; Ryf, Fontaine, Guan, et al., 2014; Ryf, Fontaine, Montoliu, Randel, Chang, et al., 2014). On the other hand, fibers in the group of A-III and B-III has larger core size to support HOMs for MDM.

Ideally, LP modes in an FMF satisfy the orthogonality condition where the power of one mode will not be coupled into other modes during its propagation in the fiber. However, the orthogonality cannot be perfectly maintained a real fiber due to irregularities in its RI profile. The irregularities can be caused by: (i) material impurities, (ii) deformation of fiber cross-section due to bending, twisting or strain and (iii) structural defects along the fiber. This enables mode coupling where the guided modes exchange power while propagate along the fiber (Ho & Kahn, 2013; Schulze, Brüning, Schröter, & Duparré, 2015). Two LP modes are orthogonal if they satisfy the following equation (Buck, 2004):

$$\int_A \hat{\mathbf{E}}_\mu \times \hat{\mathbf{H}}_\nu^* \cdot \hat{\boldsymbol{z}}\, dA_c = \int_A \hat{\mathbf{E}}_\nu^* \times \hat{\mathbf{H}}_\mu \cdot \hat{\boldsymbol{z}}\, dA_c = 0 \tag{2.67}$$

where $\hat{\mathbf{E}}_{\mu,\nu}$ and $\hat{\mathbf{H}}_{\mu,\nu}$ are the electric and magnetic fields of mode μ or ν respectively where $\mu \neq \nu$, $\hat{\boldsymbol{z}}$ is the unit vector parallel to the fiber axis, A_c is the cross-sectional area of the fiber and the asterisks denote the complex conjugate of the corresponding field. Mode coupling among the spatial modes occurs when the above-mentioned condition is violated as a result of fiber imperfections.

The propagation and coupling of LP modes in an FMF can be described by the following equation assuming that loss is negligible (Ho & Kahn, 2013):

$$\frac{dA_\mu}{dz} = -j\beta_\mu A_\mu + \sum_{\nu \neq \mu} C_{\mu\nu}(z)\, A_\nu \tag{2.68}$$

where μ, ν = 1, 2, 3… represents the orthogonal modes in the fiber, $A_{\mu,\nu}$ is the complex coefficient describing the amplitude and phase of mode μ or ν, β_μ is the propagation constant for mode μ and $C_{\mu\nu}$ is the coupling coefficient between mode μ and ν. The first term on the right-hand side of the equation represents the propagation of mode μ without coupling. Meanwhile, the second term describes the coupling between mode μ and ν. It is the weighted sum of the guided modes v in which mode μ might be coupled. The coupling coefficient indicates the strength in which mode μ will be coupled to mode v.

Without mode coupling, the second term vanishes and the power of mode μ will remain constant, while the relative phase between mode μ and v will change due to the difference in β. In general, coupling between two modes is stronger when the difference in the propagation constant of the modes, $\Delta\beta$ is smaller. For example, mode coupling between the LP_{11} degenerate modes (LP_{11a} and LP_{11b} modes) is more readily occurs as compared to that between LP_{11} and LP_{01} modes. The non-degenerated modes such as LP_{01} and LP_{11} modes will be strongly coupled if periodic RI perturbation in an FMF satisfies the following phase matching condition:

$$\Delta n_{\mathrm{eff}} = \frac{\lambda}{\Lambda} \tag{2.69}$$

where $\Delta n_{\mathrm{eff}} = n_{\mathrm{eff},\mu} - n_{\mathrm{eff},\nu}$, $n_{\mathrm{eff},\mu}$and $n_{\mathrm{eff},\nu}$ are the effective indices of mode μ and v respectively, λ is the free space wavelength and Λ is the period of the perturbation. This can be deliberately achieved through micro bending of an FMF or inscription of fiber grating in which they have been exploited for the application of LP mode converter by using fiber Bragg grating (Ali et al., 2015) and long period grating (Youngquist, Brooks, & Shaw, 1984).

Mode coupling, DMD and MDL occur during propagation in the optical fibers are the main challenges in the implementation of MDM system (G. Li et al., 2014). In the MDM approach, the impairments are commonly compensated by using Multiple-Input Multiple-Output (MIMO) digital signal processing (DSP) at the receiver end (Peter J. Winzer, Ryf, & Randel, 2013). However, the DSP will become impractical when its algorithm complexity significantly grown due to the increasing number of modes being employed. Mode coupling that occurs randomly along an FMF poses a great challenge to the implementation of MDM because it disturbs the transmission of independent data channels based on fiber modes in FMF. Modal crosstalk between the data channels might lead to the degradation of the transmitted information at the receiver end.

Mode coupling can be suppressed by increasing $\Delta\beta$ of the bound modes in the FMF (Peckham et al., 2013). Meanwhile, when β of the highest-order bound mode is close to that of leaky modes, the bound mode can be easily coupled into the leaky modes when external perturbation is applied on the fiber. This leads to MDL of the mode as the power of the highest-order bound mode reduces. Therefore, the difference in the propagation constants between the highest-order bound mode and the leaky modes, $\Delta\beta_{\mathrm{leaky}}$, needs to be kept at a reasonable level to mitigate the MDL.

Group delay of different LP modes in an FMF can be plotted as a function of V-number. An example of such plot is shown in Figure 2.11. The group delay curves for different LP modes might cross at certain V-number. It is marked by the vertical line in Figure 2.11 and it is the point where the DMD of the LP modes is zero. However, it is not always possible to apply the V-number with zero DMD in the fiber design due to constraints such as the number of bound modes to be supported by the fiber or MDL. Besides, not all fiber design have group delay curves that cross each other. In such case, V-number at which the LP modes' group delay has smallest difference will be preferable in order to obtain FMF with low DMD.

As discussed in Section 2.1, the number of bound mode supported by a fiber is indicated by its V-number which is governed by equation (2.45). From the equation, it can be seen that the V-number is a function of: (i) operating wavelength, (ii) fiber core diameter and (iii) the RIs of fiber core and cladding. If the V-number is increased (by increasing the fiber core diameter), $\Delta\beta$ and $\Delta\beta_{\mathrm{leaky}}$ can be reduced. The decrease in $\Delta\beta_{\mathrm{leaky}}$ might lead to the increase in MDL. However, the increase in effective mode area, A_{eff}, as a result of larger core diameter can prevent nonlinearities due to high optical intensity in the core. On the other hand, if the V-number is increased by increasing the core RI, $\Delta\beta$ and $\Delta\beta_{\text{leaky}}$ will increase and MDL might be reduced. In contrast to the case of increasing core diameter, increase in core RI will decrease the A_{eff} of the bound modes. Therefore, trade-off between these parameters is necessary in the design of FMF to obtain fiber with the optimum mode coupling, DMD and MDL characteristics.

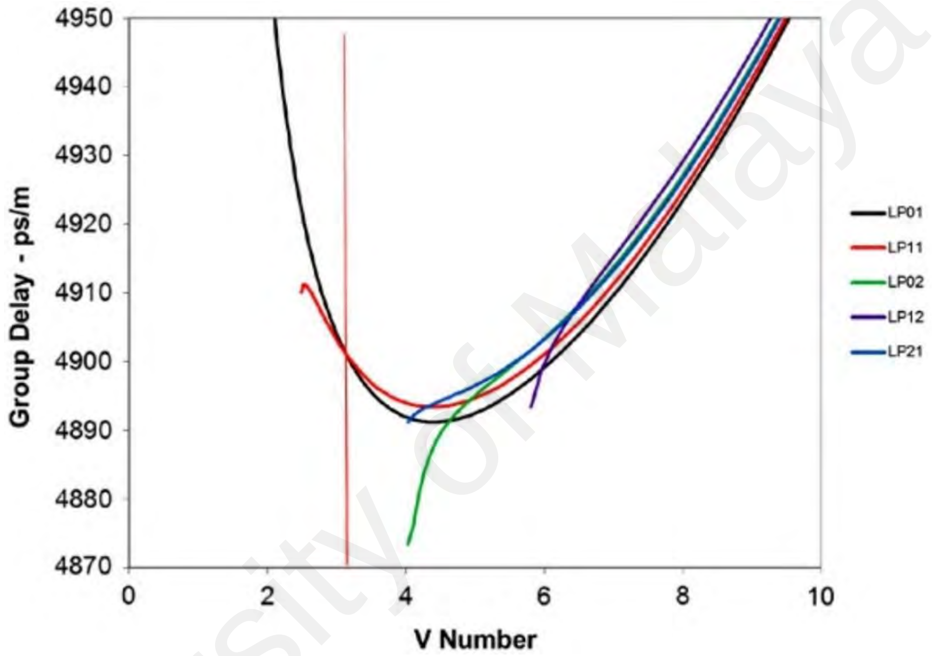

Figure 2.11: Group delay as a function of *V*-number for different LP modes of a step-index fiber. (Peckham et al., 2013)

The DMD of a fiber can be adjusted by manipulating the RI profile of the fiber core. For example, fiber core with (i) multi-step index profile (Sakamoto, Mori, Yamamoto, & Tomita, 2012), (ii) graded-index (GI) profile (M. Li et al., 2012; Mori et al., 2015; Sato, Maruyama, Kuwaki, Matsuo, & Ohashi, 2013) and (iii) GI core with trench structure around the core (Gruner-Nielsen et al., 2012; Maruyama, Kuwaki, Matsuo, & Ohashi, 2014; Sillard et al., 2016) have been demonstrated to give different DMD. One way to minimise the DMD across a transmission line is to use fiber with low DMD where the DMD can be manipulated by controlling the fiber design parameters. Another way is to form the transmission line by using concatenated fibers with opposite DMD signs (positive and negative) such that the total DMD of the line is compensated (Maruyama et al., 2014). Although mode coupling is generally undesired in MDM transmission, it has been suggested that mode coupling can be exploited to suppress DMD and MDL (G. Li et al., 2014; Xia, Bai, Ozdur, Zhou, & Li, 2011). Coupled-core fiber as shown in group II A and II B in Figure 2.10 have been used to demonstrate this approach (Ryf, Essiambre, Gnauck, et al., 2012; Ryf, Fontaine, Guan, et al., 2014; Ryf, Fontaine, Montoliu, Randel, Chang, et al., 2014).

2.2.2 SDM Multiplexers and De-multiplexers

Spatial multiplexer and de-multiplexer are key components in SDM system that enable multiplexing and de-multiplexing of multiple spatial mode channels in a single optical fiber. The (de)multiplexer can be categorised into three groups according to their physical appearance, namely fiber-based, waveguide-based and free-space-based (de)multiplexer.

The multiplexer and de-multiplexer for CM are also known as fan-in and fan-out devices respectively. In the multiplexing process for single-mode CM, optical signals from multiple SMFs are coupled into different cores of a MCF. At the receiver end, de-multiplexing process takes place by coupling the signals from the MCF cores back into SMFs. They could be manufactured from tapered fibers (Zhu et al., 2010), free-space optics (Klaus et al., 2012), grating coupler (Doerr & Taunay, 2011) or 3-D waveguides (Nicolas Riesen, Gross, Love, Sasaki, & Withford, 2017).

On the other hand, multiplexing and de-multiplexing process for MDM system involves the conversion of the spatial modes. Several MDM multiplexing schemes have been proposed. The following components have been developed for the purpose of (de)multiplexing in MDM system: (i) binary phase plate (Igarashi, Souma, Takeshima, &

Tsuritani, 2015; Igarashi, Souma, Tsuritani, & Morita, 2014; Koebele, Salsi, Milord, et al., 2011; Mohammed, Pitchumani, Mehta, & Johnson, 2006; Randel et al., 2011; Ryf, Randel, et al., 2012), (ii) spatial light modulator (Carpenter & Wilkinson, 2012; Koebele, Salsi, Sperti, et al., 2011; Salsi et al., 2012; von Hoyningen-Huene, Ryf, & Winzer, 2013), (iii) multi-plane light converter (Labroille et al., 2017; Labroille et al., 2014), (iv) grating coupler (Ding, Ou, Xu, & Peucheret, 2013; Koonen, Chen, van den Boom, & Raz, 2012), (v) photonic lantern (Birks, Gris-Sánchez, Yerolatsitis, Leon-Saval, & Thomson, 2015; N. K. Fontaine, Ryf, Bland-Hawthorn, & Leon-Saval, 2012; Leon-Saval, Argyros, & Bland-Hawthorn, 2010, 2013; Leon-Saval, Fontaine, & Amezcua-Correa, 2017; Leon-Saval et al., 2014; Ryf, Fontaine, Montoliu, Randel, Ercan, et al., 2014; Velázquez-Benítez et al., 2018; Weerdenburg et al., 2018), (vi) few-mode fiber Bragg grating (FM-FBG) (Ali et al., 2015; Gao, Sun, Chen, & Sima, 2015; Lee & Erdogan, 2001; Strasser, Pedrazzani, & Andrejco, 1997; Wu et al., 2012), (vii) long period fiber grating (LPG) (Al Amin et al., 2011; Dong & Chiang, 2015; Giles et al., 2012; Xie et al., 2013; Youngquist et al., 1984) and (viii) mode selective coupler (MSC) (Igarashi, Park, Tsuritani, Morita, & Kim, 2018; Ismaeel & Brambilla, 2016; Ismaeel, Lee, Oduro, Jung, & Brambilla, 2014; Love & Riesen, 2012; Song, Hwang, Yun, & Kim, 2002; Song & Kim, 2003). In general, these (de)multiplexers operate based on two approaches: (i) matching the transverse mode profiles of an FMF and (ii) matching the propagation constant of transverse modes in FMF. In the following sub-sections, MDM (de)multiplexers based on these two approaches will be discussed.

2.2.2.1 Matching Transverse Mode Profiles of FMF

Two (de)multiplexing schemes based on the matching of FMF transverse mode profiles have been developed. In the first scheme, mode converter is used to convert the input mode profile into a profile that matches with the target LP mode in FMF or SMF.

Then, the converted mode is coupled into the FMF or SMF. This scheme maps multiple SMFs directly into different LP modes in FMF or vice versa. In the multiplexing process, fundamental modes from multiple SMFs are first converted into different profiles that match with the LP modes of FMF. After that, the converted modes are coupled into the FMF for transmission. At the FMF output (receiver end), de-multiplexing process is performed to separate the LP modes. Following that, the LP modes could be converted back to fundamental mode before being coupled into SMFs for transmission out of the de-multiplexer. This scheme has been used in most of the early SDM experiments (Koebele, Salsi, Milord, et al., 2011; Koebele, Salsi, Sperti, et al., 2011; Randel et al., 2011; Ryf, Randel, et al., 2012; Salsi et al., 2012) where SLM and BPP are the commonly used mode converters.

SLM and BPP operate by modulating the phase profile of the input beam to match it with the profile of the desired LP mode. Commonly, SLM with Liquid Crystal on Silicon (LCoS) is used to achieve the phase modulation. Either a transmissive or reflective SLM can be used where the profile is programmed onto the liquid crystal array on the SLM (Salsi et al., 2012; von Hoyningen-Huene et al., 2013). The resolution of the profile generated by SLM depends on the size of the array pixels. On the other hand, BPP converts the phase profile of the input beam by using the phase pattern on one of its surface (Igarashi et al., 2014). The phase pattern consists of protruded regions which will introduce a phase shift of π in relative to the un-protruded region when light passing through the pattern. Different phase patterns are used to produce phase profile that matches with different LP modes. The operation of BPP is simpler as compared to SLM.

$LP_{01} \rightarrow LP_{11}$ mode conversion by using two adjoined glass slides has been reported by Thornburg et al. as early as 1994 (Thornburg, Corrado, & Zhu, 1994). One of the slides was deliberately tilted to introduce a relative phase shift of π to a part of the transmitted beam. It was suggested that the separation of the two slides has limited the purity of the converted LP_{11} mode. Following that, Mohammed et al. used an integrated phase element to perform $LP_{01} \rightarrow LP_{11}$ mode conversion (Mohammed et al., 2006). The phase element is similar to the BPP being used today where the phase pattern was made of polymer. The integrated design eliminates the separation in the mode converter based on two glass slides.

Igarashi et al. has investigated the effect of BPP phase pattern imperfection on the converted beam via simulation (Igarashi et al., 2014). The effect of phase pattern thickness uniformity and the slope width at the edge of the protruded and non-protruded regions has been simulated. The coupling efficiency of the converted beam into the i-th LP mode in an FMF is given by (Igarashi et al., 2014; Ryf, Randel, et al., 2012):

$$\eta_i = \left| \iint A(x,y) \cdot \psi_i^*(x,y)\, dx\, dy \right|^2 \tag{2.70}$$

where *A(x,y)* is the complex amplitude of the converted beam at the FMF input facet, $\psi_i(x,y)$ is the complex amplitude of the i-th LP mode and $\psi_i^*(x,y)$ is the complex conjugate. From simulation result, it is found that the size of the converted beam immediately before being launched into an FMF has an impact to the coupling efficiency into the desired LP mode. In the experiment, asymmetry converted beam was observed when the edge of the phase pattern has slope width of 200 μm. In contrast, symmetry converted beam was obtained when the slope width was less than 0.1 μm. The input beam size before being converted by the BPP was ~1 mm in both cases.

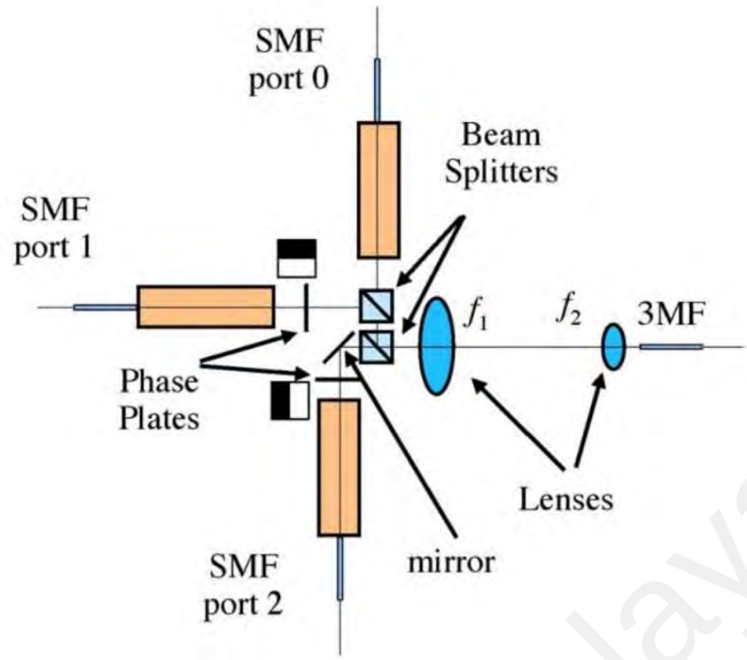

Figure 2.12: SDM setup using binary phase plates. (Ryf, Randel, et al., 2012)

Figure 2.12 shows the setup of an SDM multiplexer employing BPP. The optical signals in LP_{01} mode from the SMFs are first collimated by collimator at the end of each SMF. Then, the collimated output beams from two of the SMFs (Port 1 and 2) are transmitted through the BPPs to modulate their phase profiles to match with the degenerate LP_{11} modes (LP_{11a} and LP_{11b} modes) in the FMF. Meanwhile, the collimated output beam from the third SMF (Port 0) remains in the LP_{01} mode. After that, all the beams are combined by using beam splitters and they are launched into the three-mode fiber (3MF) by a lens system to excite the corresponding modes in the fiber. Similar setup can be used as a de-multiplexer with the light propagates in the reverse direction. The following paragraphs will discuss about the (de)multiplexers based on the second scheme.

The second scheme has been introduced to improve the insertion loss of the first scheme. Spot-based (de)multiplexer and photonic lantern are devices that operate based on the second scheme. In contrast to the first scheme, spot-based (de)multiplexer and photonics lantern do not use pure LP modes as independent data channels. Instead, each spatial transmission channel is a linear combination of the fiber modes.

In spot-based (de)multiplexer, optical signals from multiple SMFs are imaged onto specific spots on the input facet of the FMF core. The total number of spot that can be accommodated by an FMF depends on the number of LP modes supported by the fiber. The spot arrangement for FMF that supports two, four and five LP modes have been proposed by Ryf et al. and they are shown in Figure 2.13. The spot-based (de)multiplexer is also known as spot-based mode coupler. Ryf et al. has performed theoretical analysis for the device and shows that the spot diameter will affect the insertion loss (Ryf, Fontaine, & Essiambre, 2012).

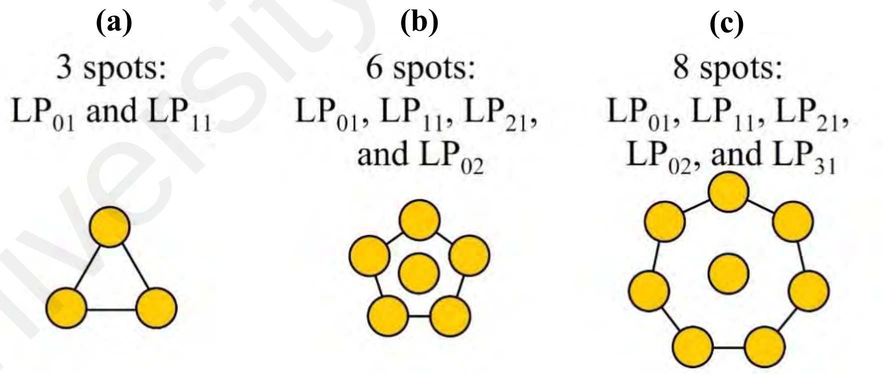

Figure 2.13: Spot arrangements on the FMF input facet to couple optical signals from: (a) 3, (b) 6 and (c) 8 SMFs. (Ryf, Fontaine, et al., 2012)

The 3-spot configuration has been demonstrated experimentally by Ryf et al. where free space optics (mirrors and lens) have been used to image the optical signals from SMFs onto the FMF input facet (Ryf, Mestre, et al., 2012). After that, the mirrors were replaced by a single prism to simplify the setup (Chen et al., 2013). Figure 2.14 shows the setup of the prism-based 3-spot multiplexer. As shown in Figure 2.14(a), the beam from SMFs are reflected by the prism surfaces towards lens system. Then, the 3 spots are imaged by the lens system onto the FMF. Figure 2.14(d) shows the mode profiles recorded at the FMF output when only one of the spots is launched into the FMF. It shows that the mode at the FMF output is not pure LP mode. Since the output mode profile is a linear combination of fiber modes, digital signal processing is necessary to recover the original signals transmitted through the FMF. It was shown that the 3-spot multiplexer has insertion loss which is ~3 dB lower than the multiplexer based on the first scheme.

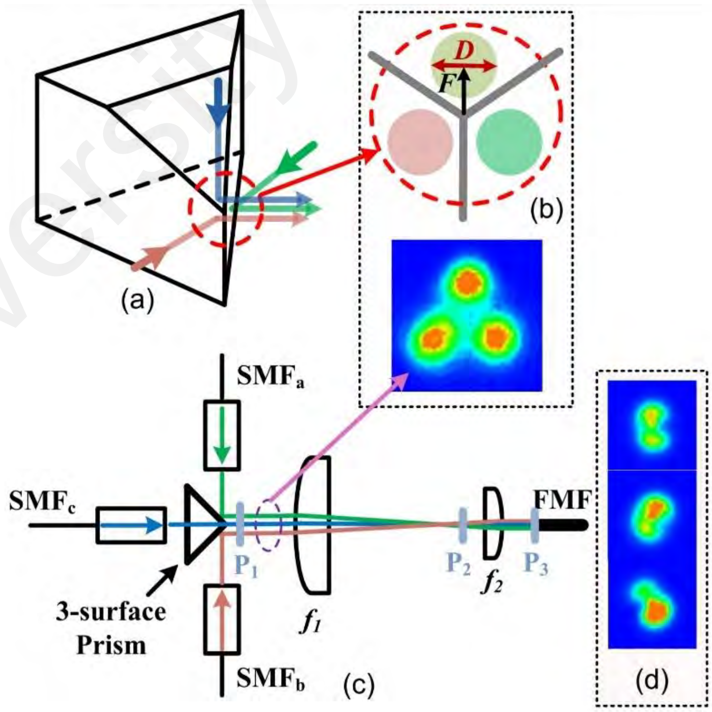

Figure 2.14: Prism-based 3-spot multiplexer. (Chen et al., 2013)

The optical components and setup for the spot-based (de)multiplexer become more complicated when the number of spot increases. Therefore, it was superseded by photonic lantern which does not require the free-space optics to couple the optical signals from SMFs into the FMF or vice versa. The photonic lantern was first developed for application in the field of astronomy (Noordegraaf, Skovgaard, Nielsen, & Bland-Hawthorn, 2009) and later found its use as (de)multiplexer of SDM system (N. K. Fontaine, 2013; N. K. Fontaine et al., 2012).

To fabricate a photonic lantern, a SMF bundle is inserted into a low-index glass capillary tube and one end of the tube with the SMFs is tapered to create a multimode core resulted from the fusion of the SMFs (Noordegraaf et al., 2010; Noordegraaf et al., 2009). The low-index glass capillary functions as the cladding of the multimode core. This type of photonic lantern has multiple SMFs on one end and a single multimode fiber at the other end. It is also possible to fabricate a photonic lantern for MCF by applying the tapering process at one end of a MCF covered by a low-index glass capillary tube (Birks, Mangan, Díez, Cruz, & Murphy, 2012). Due to the tapering process, the cores collapse to form a single multimode core with the capillary tube as the cladding. Other than that, waveguide-based photonic lantern can be fabricated in bulk glass by using ultrafast laser inscription (Spaleniak et al., 2013; Thomson, Birks, Leon-Saval, Kar, & Bland-Hawthorn, 2011). Figure 2.15 shows the different photonic lanterns described above. Adiabatic transition from the SMF bundle/multicore fiber into a multimode core will provide very low loss coupling between the two ends of the photonic lantern. Insertion loss lower than 0.5 dB has been reported for a 6-mode photonic lantern (Velazquez-Benitez et al., 2015).

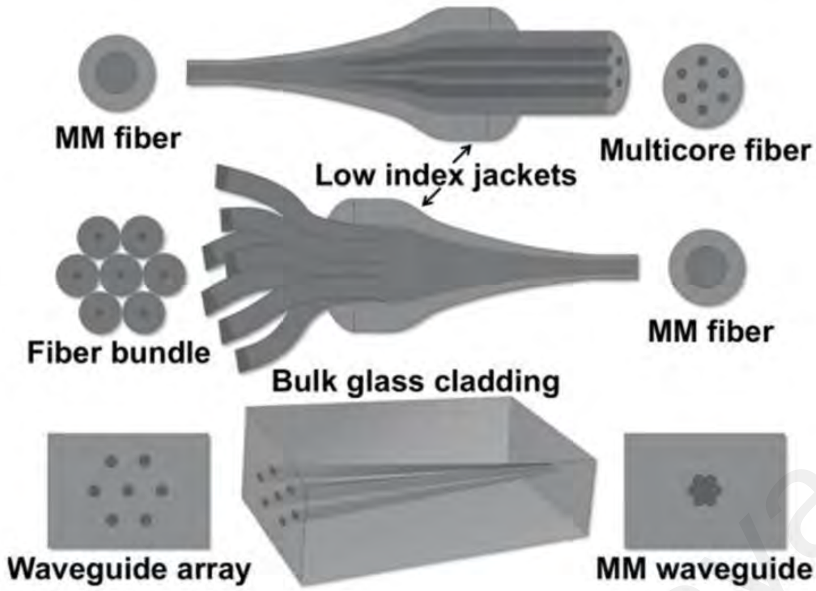

Figure 2.15: Photonic lantern in different forms. (Leon-Saval et al., 2013)

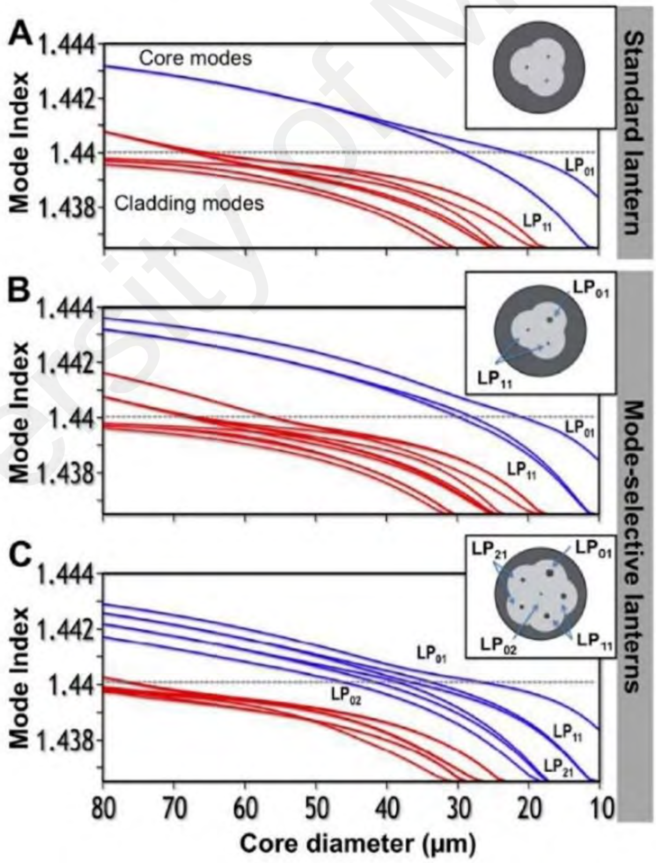

Figure 2.16: Evolution of mode index for core and cladding modes when the core diameter of the photonic lantern is adiabatically reduced to a multimode core: (A) Standard lantern, (B) 3-mode-selective lantern and (C) 6-mode-selective lantern. (Leon-Saval et al., 2017)

The SMF bundle in a photonic lantern might have same or different core sizes. It is known as standard lantern if the SMFs have the same core size and mode-selective lantern if the core size of SMFs is different as presented in Figure 2.16. In a standard lantern, the modes in the SMFs have same mode index or propagation constant since the SMFs have core with same size. When the modes from each SMF propagate across the adiabatic transition region, they will couple with each other to form non-degenerate supermodes which become linear combinations of the LP modes in the multimode core. This is similar to the operation of spot-based (de)multiplexer. The number of modes supported by the multimode core in a standard lantern is equal to the number of SMFs.

On the other hand, when SMFs with different core sizes are used, the mode indices for different LP modes are well separated across the adiabatic transition region when the core diameter of the lantern decreases from 80 to 10 μm. This allows each SMF to excite a specific LP mode in the multicore end. For example, the 3-mode-selective photonic lantern shown in Figure 2.16(B) has one of its SMF core larger than the other two. When light is launched into the lantern through the SMF with larger core, LP_{01} mode is excited in the multicore end. Meanwhile, LP_{11} mode is excited in the multicore end if light is launched into either of the SMFs with smaller cores. The two smaller cores excite different LP_{11} degenerate modes, namely LP_{11a} and LP_{11b}. Figure 2.17 shows the LP_{01} and LP_{11} mode profiles at the multimode output when light is launched into the different SMFs of a 3-mode-selective photonic lantern.

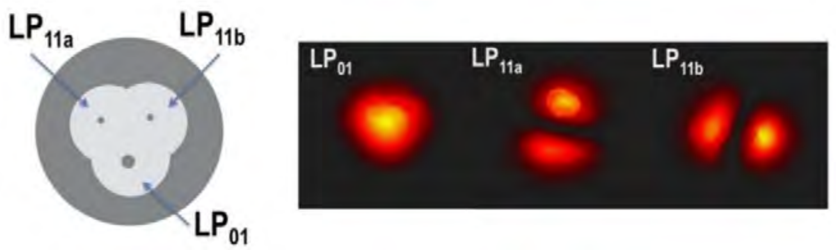

Figure 2.17: Cross-section of a 3-mode-selective photonic lantern and the LP modes observed at its multimode output. (Leon-Saval et al., 2017)

2.2.2.2 Matching Propagation Constants of Transverse Modes in FMF

This approach (de)multiplexes the optical signals between SMFs and FMF by satisfying the phase matching condition between the fundamental modes in SMFs and the HOMs in FMF. Among the (de)multiplexing techniques that employs this approach are: (i) FM-FBG, (ii) LPG, and (iii) MSC.

Phase matching condition and asymmetric cross-sectional RI distribution of a FM-FBG will lead to cross-mode coupling in the FMF. Therefore, FM-FBG with asymmetric cross-sectional RI distribution has been exploited to couple the power of the forward propagating mode into a desired mode in backward propagation direction (Ali et al., 2015; Wu et al., 2012). It is a potential mode converter in MDM (de)multiplexer. By using a four-mode FBG, $LP_{01} \leftrightarrow LP_{11}$, $LP_{01} \leftrightarrow LP_{21}$, $LP_{01} \leftrightarrow LP_{02}$, $LP_{11} \leftrightarrow LP_{21}$, $LP_{11} \leftrightarrow LP_{02}$ and $LP_{21} \leftrightarrow LP_{02}$ mode conversion have been demonstrated (Ali et al., 2015). However, this mode converter has a narrow operating wavelength range because the phase matching condition depends on the FM-FBG grating period. The operation bandwidth of the FM-FBG mode converter can be tuned by manipulation of the grating period with temperature or strain. The degree of asymmetry of RI distribution across the FMF core will affect the overlap integral between different modes. Therefore, it will affect the intensity of the cross-mode coupling. If the cross-sectional RI distribution is uniform, the overlap integral will be zero and cross-mode coupling will not occur. Tilted FM-FBG has similar function as the asymmetric cross-sectional RI distribution to introduce non-zero overlap integral between different modes in an FMF. Mode conversion by using a tilted FM-FBG has also been demonstrated (Gao et al., 2015; Lee & Erdogan, 2000, 2001; Strasser et al., 1997).

Meanwhile, mechanical LPG has also been used as mode converter in MDM (de)multiplexing (Al Amin et al., 2011). The LPG can be created on an FMF by squeezing a periodic mechanical grating on the FMF to generate periodic microbend on the fiber

(Blake, Kim, & Shaw, 1986; Giles et al., 2012; Sakata, Sano, & Harada, 2014; Youngquist et al., 1984). Similar to the FM-FBG, the phase matching condition and non-zero overlap integral are the necessary conditions to obtain the mode conversion. Mode conversion is achieved when the period of the LPG is matched with the modal beat length of the two modes involved. The modal beat length is a function of operating wavelength and the effective indices of the modes. The conversion efficiency depends on the depth of the microbend which is related to the pressure applied on the FMF by the mechanical grating. The number of microbend generated by the mechanical grating will also affect the conversion efficiency. Other than mechanical grating, mode conversion by LPG inscribed in a TMF manufactured using CO_2 laser (Dong & Chiang, 2015; Xie et al., 2013) and ultraviolet (UV) laser (Ramachandran, Wang, & Yan, 2002) has also been demonstrated.

When a pre-tapered SMF is fused with an FMF, the power of fundamental mode in the SMF can be coupled into the HOM in FMF if the phase matching condition is satisfied (Love & Riesen, 2012; N. Riesen & Love, 2012; Song et al., 2002; Song & Kim, 2003; Sorin, Kim, & Shaw, 1986). The SMF is pre-tapered to a specific diameter before being fused to the FMF so that the propagation constant of the fundamental mode in SMF is manipulated to match with the desired HOM in the FMF (Ismaeel et al., 2014). On the other hand, it was observed that the polarisation of the LP_{01} mode in SMF might affect the orientation/degeneracy of the LP_{11} mode in the FMF to which it was coupled (Ismaeel & Brambilla, 2016). However, it was found that the effect can be eliminated by controlling the coupling length between the SMF and FMF. Meanwhile, the coupling length between the SMF and FMF is also critical in getting the optimum coupling efficiency. Structured MSC as shown in Figure 2.18 has been proposed to selectively excite the LP_{11} degenerate modes in an FMF (B. Huang, Xia, Matz, Bai, & Li, 2013). The angular separation between the SMFs around the FMF, φ, the coupling length of the

SMFs, L, and core size of the SMFs, a, are the important parameters that will affect the coupling efficiency.

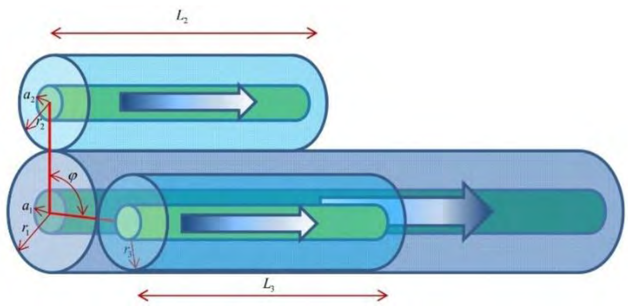

Figure 2.18: Structured MSC to achieve selective excitation of degenerate LP_{11} modes. (B. Huang et al., 2013)

MDM multiplexer based on fiber MSC can be achieved by splicing the FMF on multiple MSCs in series as shown in Figure 2.19. Each MSC will couple the fundamental mode from SMF into a desired mode in the FMF. In the de-multiplexing process, modes in the FMF are coupled back to the SMFs through the MSC. However, Love and Reisen have suggested the coupling of HOM from FMF back to that the fundamental mode in SMF might be inefficient due to the rotated asymmetry HOM profile in the FMF (Love & Riesen, 2012). They have proposed the use of MSC de-multiplexer composed of three cores (similar to that shown in Figure 2.18) to efficiently de-multiplex a HOM back to fundamental mode in the SMFs. Recently, Igarashi et al. have demonstrated a MDM system by using fiber MSC (de)multiplexer (Igarashi et al., 2018). The optical signals were multiplexed into six modes (LP_{01}, LP_{11a}, LP_{11b}, LP_{21a}, LP_{21b} and LP_{02}) in the FMF. The insertion loss was 2.2 dB for LP_{21} modes while it was less than 1.5 dB for other modes.

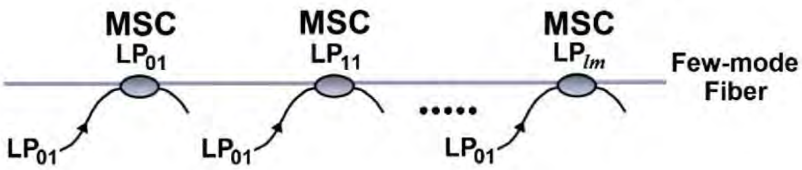

Figure 2.19: Schematic of SDM multiplexer based on cascaded MSCs. (Love & Riesen, 2012)

The fiber MSC has the advantage of low insertion loss and all-fiber design which can be easily integrated with the optical fiber network. Coupling efficiency greater than 90% has been demonstrated when fundamental mode was coupled into HOMs in FMF for operating wavelength range of 1500 – 1600 nm (Ismaeel et al., 2014). Adiabatically tapered MSC has been proposed to enhance the operating bandwidth but fabrication of such fiber device remains a challenge (N. Riesen & Love, 2013). In spite of that, it has been made in 3-D integrated photonic chip based on ultrafast laser inscription technique. Operating bandwidth across S, C and L bands has been achieved with average insertion loss of 1.8 dB (Nicolas Riesen et al., 2017).

2.2.3 SDM Amplifiers

Other than optical fiber, optical amplifier is also an important component in SDM transmission system. Multicore and multimode erbium-doped fiber amplifier (EDFA) have been developed for such purpose (Abedin et al., 2011; Chen et al., 2016; N. K. Fontaine et al., 2016; Jin et al., 2015; Jung et al., 2011; Jung et al., 2014; Sakaguchi et al., 2014; Takahashi et al., 2013). A challenge in SDM EDFA amplifier is the control of core- and mode-dependent gain so that the power across different cores and modes can be equalised by using the amplifier. Meanwhile, Raman amplifier has also been employed to increase the intensity of optical signals in both multimode and multicore transmission (Antonelli, Mecozzi, & Shtaif, 2013; Kobayashi et al., 2013; Ryf et al., 2015; Ryf, Essiambre, Hoyningen-Huene, & Winzer, 2012; Ryf, Sierra, et al., 2011). It offers the advantages of gain flatness and low noise figure as compared to EDFA. Multicore fiber remote optical pump amplifier is another potential candidate for practical application in SDM system (Takara et al., 2014).

CHAPTER 3: UP-CONVERSION OF LP MODE BY FUSED SILICA BPP

In this chapter, investigation on the use of fused silica binary phase plate (BPP) for efficient up-conversion of LP mode will be reported. A technique to extend the operation wavelength range of the BPP for efficient mode conversion and excitation will be proposed and demonstrated. Besides, a method to estimate the modal purity of a LP_{11} mode profile based on the comparison of theoretical and measured one-dimensional(1-D) LP_{11} mode profile will be presented.

In Section 3.1, the theoretical background of mode conversion by a BPP will be discussed. Then, the processes to fabricate the fused silica BPP used in this work will be provided in Section 3.2.1. In Section 3.2.2, the methodology to excite LP_{11} mode in a TMF by using the BPP mode conversion system will be presented. Besides, the procedure to investigate the effect of operating wavelength, phase pattern thickness and BPP tilt angle on the TMF output beam will be discussed. Finally, the results and discussion will be presented in Section 3.3.

3.1 Theoretical Background of Mode Conversion by BPP

A fused silica BPP performs phase modulation on the incoming fundamental mode to generate a transverse mode field distribution similar to the desired higher order mode (HOM) in few-mode fiber (FMF). This is achieved by the phase pattern on the BPP which consists of protruded and non-protruded area(s). Figure 3.1 shows the phase patterns to generate different HOM profiles. The grey areas on the patterns are protruded area which will introduce a relative phase shift of π to the transmitted light. The phase pattern thickness, *d*, is defined as the height of the protruded area relative to the non-protruded area as depicted in Figure 3.2. It has significant influence on the operating wavelength at which a BPP can perform efficient mode conversion and excitation in FMFs. Meanwhile, due to imperfection in fabrication process, normally the edge of the protruded edge is not perfectly vertical. Instead, it has a width of s as shown in Figure 3.2. It has been shown that beam converted by BPP with $s < 0.1$ μm is more symmetry than that generated by BPP with $s \sim 200$ μm (Igarashi et al., 2014).

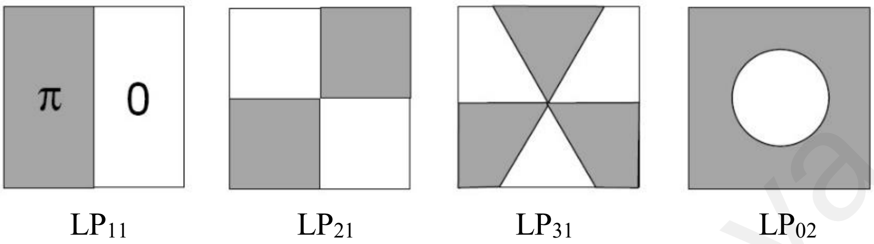

Figure 3.1: Phase patterns on BPP for selective conversion to different LP modes. (Igarashi et al., 2014)

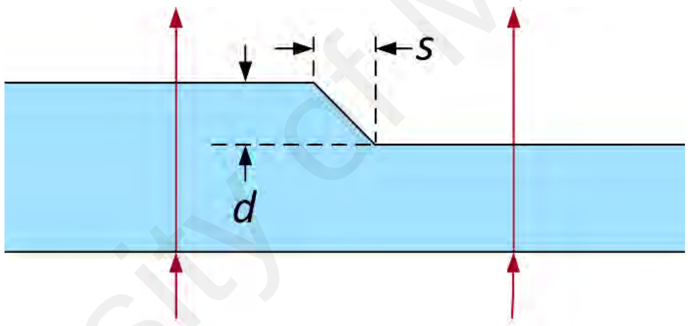

Figure 3.2: Cross-sectional view of the BPP for LP_{11} mode conversion.

Light passes through the protruded area(s) encounters longer optical path length as compared to that passes through the non-protruded area(s). This leads to relative phase difference between the light transmitted through the two areas. A relative phase difference of π is required to achieve an efficient mode conversion. From geometrical optics, the optical path length, OPL, is given by:

$$\mathrm{OPL} = n_i d_i \tag{3.1}$$

where n_i is the refractive index (RI) of the propagation medium and d_i is the distance travelled by the light in the medium. Referring to Figure 3.2, when the ray on the left travels across the protruded area in the BPP for a distance of d, the ray on the right travels the same distance in free space. Their optical path length is different because the ray of the left travels more in the glass medium that has a higher RI than that of free space. Therefore, optical path difference, OPD, between the left and right ray after travelling the distance of d as shown in Figure 3.2 is:

$$\mathrm{OPD} = nd - n_0 d = (n - n_0)d \tag{3.2}$$

where n and n_0 are the RIs of BPP and free space respectively while d is equivalent to the phase pattern thickness. Upon travelling across the mediums with different RI for a distance of d, the two rays will gain a phase difference of $\Delta\phi$ with respect to each other which is given by:

$$\Delta\phi = \frac{2\pi}{\lambda}(n - n_0)d \tag{3.3}$$

where λ is the operating wavelength. To introduce phase shift of π between the left and right rays, let $\Delta\phi = \pi$ and equation (3.3) becomes:

$$\lambda_D = 2d(n - n_0) \tag{3.4}$$

where λ_D is the design wavelength of the BPP. The design wavelength is the operating wavelength in which the phase difference of π can be achieved when the normal axis of the BPP is aligned to the light propagation direction. Equation (3.4) is used to determine the design wavelength for a specific phase pattern thickness, d. For the case of tilted BPP, the tilt angle, θ_1 needs to be taken into consideration in the determination of d. Thus, equations (3.1) – (3.4) need to be generalised to include the variable θ_1 when the BPP is tilted. Derivation of the relationship between θ_1, λ and d will be shown in the following section.

3.1.1 Relationship between θ_1, λ and d based on Geometrical Optics

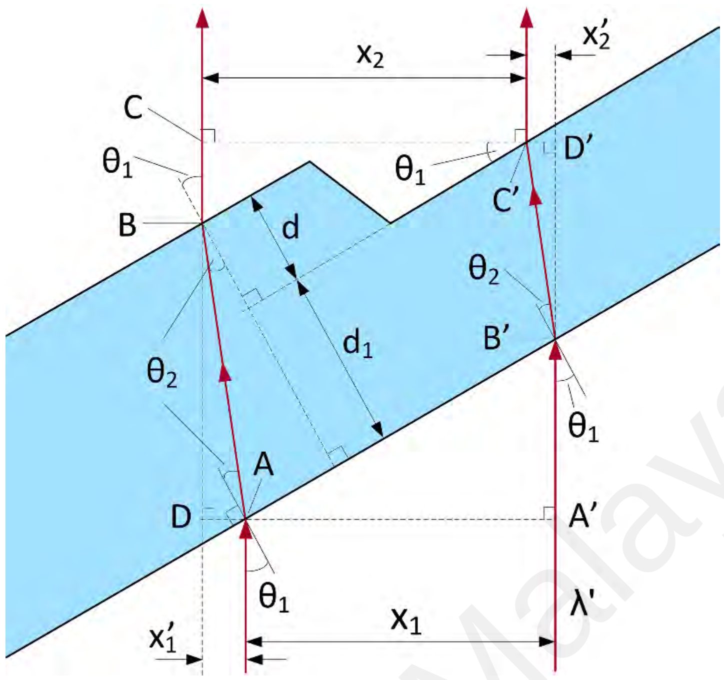

Figure 3.3: Rays propagate across the protruded and non-protruded area of a tilted BPP.

Figure 3.3 illustrates the paths of the left and right rays propagate across a BPP tilted to an angle of θ_1, an angle between the normal axis of BPP and the light propagation direction. The left ray represents the light that passes through the protruded area while the right ray represents the light that passes through the non-protruded area. The dashed lines AA' and CC' are perpendicular to the rays in free space. The sections of rays before AA' and after CC' are assumed to have the same OPL. On the other hand, the section of left and right rays between the two dashed lines, namely AC and A'C', have different OPL due to the protruded and non-protruded areas of the tilted BPP. The OPL of the left ray between AA' and CC' is:

$$\mathrm{OPL_{left}} = n\mathrm{AB} + \mathrm{BC} \tag{3.5}$$

while the OPL of the right ray between AA' and CC' is:

$$\mathrm{OPL_{right}} = \mathrm{A'B'} + n\mathrm{B'C'} \tag{3.6}$$

Then:

$$\begin{aligned} \mathrm{OPD} &= \mathrm{OPL_{left}} - \mathrm{OPL_{right}} \\ &= n(\mathrm{AB} - \mathrm{B'C'}) + (\mathrm{BC} - \mathrm{A'B'}) \end{aligned} \tag{3.7}$$

From Figure 3.3, it can be shown that:

$$\mathrm{AB} = \frac{(d + d_1)}{\cos \theta_2} \tag{3.8}$$

$$\mathrm{BC} = \mathrm{x}_2 \tan \theta_1 - \frac{d}{\cos \theta_1} \tag{3.9}$$

$$\mathrm{A'B'} = \mathrm{x}_1 \tan \theta_1 \tag{3.10}$$

$$\mathrm{B'C'} = \frac{d_1}{\cos \theta_2} \tag{3.11}$$

Substituting equations (3.8) – (3.11) into equation (3.7), we get:

$$\mathrm{OPD} = \frac{nd}{\cos \theta_2} - \frac{d}{\cos \theta_1} + (\mathrm{x}_2 - \mathrm{x}_1) \tan \theta_1 \tag{3.12}$$

It is necessary to eliminate x_1 and x_2 from equation (3.12). From Figure 3.3:

$$\begin{aligned} \mathrm{CD'} &= \mathrm{DA'} \\ \mathrm{x}_2 + \mathrm{x}_2' &= \mathrm{x}_1 + \mathrm{x}_1' \\ \mathrm{x}_2 - \mathrm{x}_1 &= \mathrm{x}_1' - \mathrm{x}_2' \end{aligned} \tag{3.13}$$

From the triangles ABD and B'C'D', x_1' and x_2' are:

$$\mathrm{x}_1' = \mathrm{AB} \sin(\theta_1 - \theta_2) \tag{3.14}$$

$$\mathrm{x}_2' = \mathrm{B'C'} \sin(\theta_1 - \theta_2) \tag{3.15}$$

Substitute equations (3.8), (3.11), (3.14) and (3.15) into equation (3.13):

$$\begin{aligned} \mathrm{x}_2 - \mathrm{x}_1 &= \frac{d}{\cos \theta_2} \sin(\theta_1 - \theta_2) \\ &= \frac{d}{\cos \theta_2} (\sin \theta_1 \cos \theta_2 - \cos \theta_1 \sin \theta_2) \end{aligned} \tag{3.16}$$

From Snell's law:

$$\sin \theta_1 = n \sin \theta_2 \tag{3.17}$$

Applying equations (3.16) and (3.17) in equation (3.12), it can be shown that:

$$\mathrm{OPD} = d(n \cos \theta_2 - \cos \theta_1) \tag{3.18}$$

Then, the phase difference between the left and right rays after propagated across the tilted BPP is:

$$\begin{aligned} \Delta\phi &= \frac{2\pi}{\lambda}(\mathrm{OPD}) \\ &= \frac{2\pi}{\lambda}[d(n \cos \theta_2 - \cos \theta_1)] \end{aligned} \tag{3.19}$$

To introduce phase shift of π between the left and right rays, let $\Delta\phi = \pi$ and equation (3.19) becomes:

$$d = \frac{\lambda'}{2(n \cos \theta_2 - \cos \theta_1)} \tag{3.20}$$

where λ' is the matched wavelength at tilt angle of θ_1. The matched wavelength is the wavelength at which a phase shift of π can be introduced by a BPP tilted to θ_1. Equation (3.20) shows that it is possible to obtain phase difference of π between the transmitted beams through protruded and non-protruded areas by tilting the BPP. If the equation is not satisfied, phase shift of π cannot be achieved and the fundamental mode cannot be efficiently converted into the desired HOM. Based on equation (3.20), we propose a technique to extend the operating wavelength range of a BPP in which efficient mode conversion and excitation can be achieved based on a tilted BPP. From the equation, the shortest matched wavelength is equivalent to the design wavelength ($\theta_1 = 0^{\circ}$) for a given phase pattern thickness. When the tilt angle increases, the matched wavelength becomes longer than the design wavelength.

3.2 Methodology

3.2.1 Fabrication of Fused Silica BPP

Two LP_{11} fused silica BPP with different phase pattern thicknesses were fabricated to examine the mode conversion performance of a tilted BPP. The fabrication process is illustrated in Figure 3.4. Circular fused silica plates with substrate thickness of 2 mm were used in the fabrication. The refractive index of the plates is 1.444. In general, the fabrication employed the photolithography process and inductively-coupled plasma (ICP) dry etching to form the phase pattern on the fused silica plate.

Firstly, the circular fused silica plate was cleaned by acetone, isopropyl alcohol (IPA) and de-ionised (DI) water to remove dirt and impurities on the surface of the plate. Then, the plate was loaded into the vacuum chamber of a direct-current (DC) sputtering system. Inside the vacuum chamber, the plate was covered by a shutter before the actual deposition began. The vacuum chamber was first pumped down to $\sim 10^{-3}$ Torr by a rotary pump. This is followed by the evacuation using a turbomolecular pump to achieve a pressure of $\sim 10^{-6}$ Torr.

Then, argon gas was flowed into the chamber at a rate of 5 sccm where the gas increased the chamber pressure to 3.5 mTorr. When the gas flow rate and chamber pressure have stabilised as observed from the flow and pressure meters, the DC power supply was switched on to generate an Argon plasma between the plate and the high purity chromium target. The shuttle that covered the plate was opened after the plasma became stable as observed from the reading of current on the power supply.

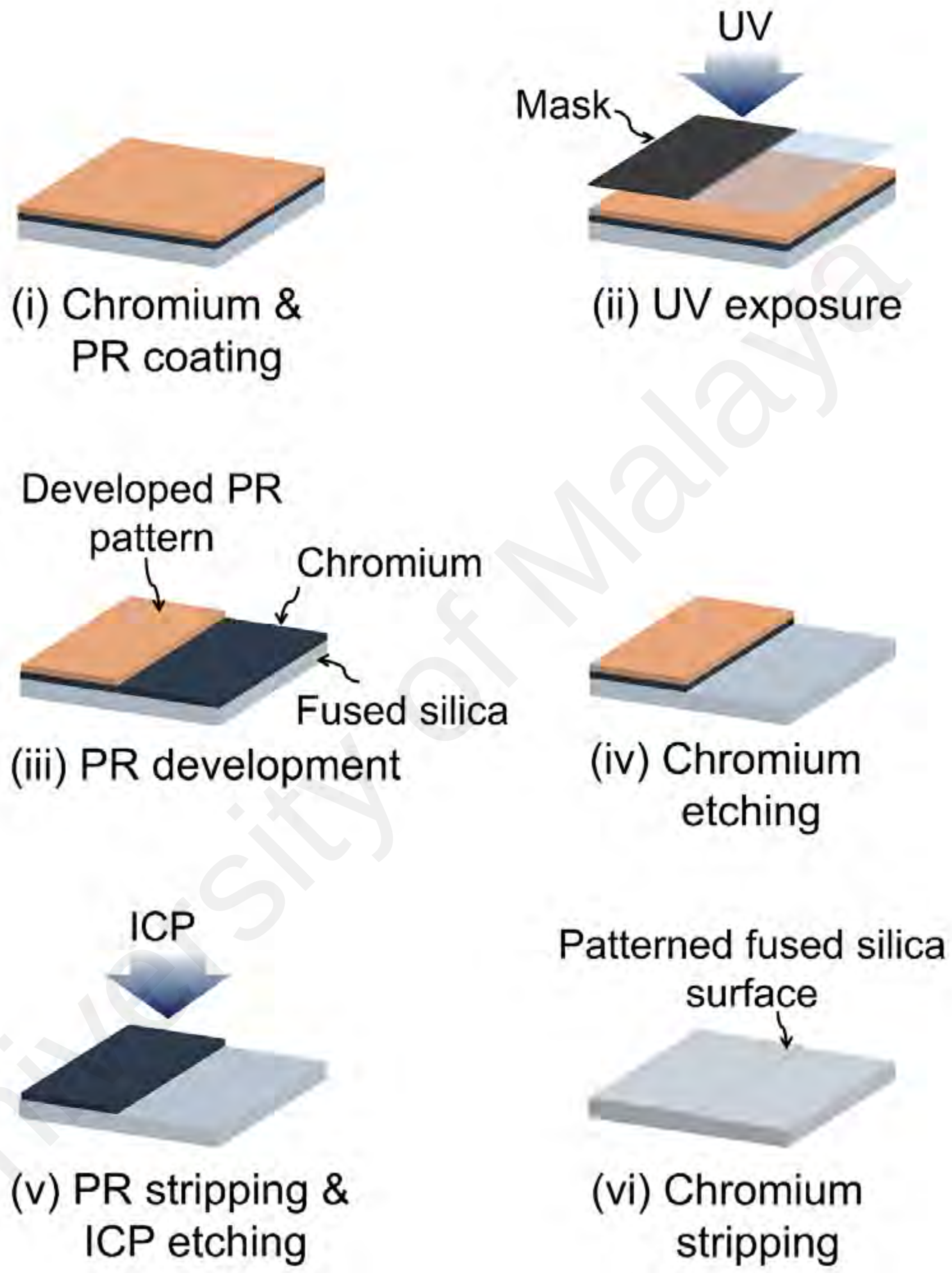

Figure 3.4: Fabrication process steps of a fused silica BPP.

In the sputtering system, the target and the plate were connected to the cathode and anode of the power supply respectively. This generated an electric field that attracted the Argon ions in the plasma towards the target. Bombardment of the Argon ions on the target ejected chromium particles from the target towards the plate. This eventually led to the formation of chromium thin film on the plate.

The power supply was switched on for about 8 minutes to deposit a chromium thin film of ~150 nm on the plate. After the DC power supply was switched off, Argon gas cycle purge was performed to evacuate the residual chromium particles floating in the chamber. Following the cycle purge, the chromium-deposited circular fused silica plate was removed from the vacuum. The thickness of the chromium thin film was controlled to be around 150 nm so that it is sufficiently thin to be conveniently removed after the photolithography process that follows, but thick enough to shield the plate during the ICP dry etching stage.

Figure 3.5: DC sputtering system used to deposit chromium layer on the circular fused silica glass plate.

Next, spin-coating technique was used to deposit a layer of positive photoresist (PR) on top of the chromium thin film. Upon the deposition of PR, the plate was soft-baked on a hot plate set to 80 ºC to dry the PR for 2 minutes. The surface of the plate with PR coating was facing upward to avoid contamination and damage to the coating while the opposite surface without coating was in direct contact with the hot plate. The purpose of the soft-baking process is to remove the solvent from the PR and enhance its adhesion on the chromium coating. This completed the first stage shown in Figure 3.4(i).

After that, the plate was transferred to a photolithography mask aligner. On the mask aligner, the plate was aligned by a 4-axis alignment system under a photomask with patterns shown in Figure 3.1. Upon the completion of the alignment process, the PR-coated plate was exposed to ultraviolet (UV) light from a mercury lamp for 18 seconds. The mercury lamp emitted broadband UV light in the range of 275 – 650 nm which peaked at 365 nm. Since the PR coating was covered by the photomask's pattern, part of the PR was not exposed to the UV light (Figure 3.4(ii)).

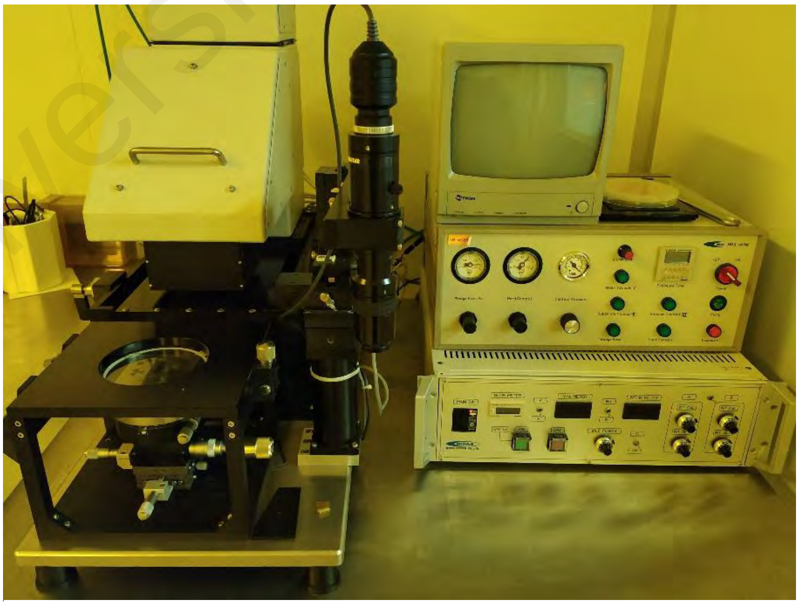

Figure 3.6: Photolithography system used to transfer the phase patterns onto the PR coating.

Chemical wet etching processes were performed after the UV exposure (Figure 3.4(iii)). Firstly, the plate was immersed in PR developer. The PR coating exposed to the UV light was dissolved by the developer while the unexposed part remained on the chromium surface. After 1 minute, the plate was taken out from the developer, rinsed by DI water and blow-dried by nitrogen gas to remove the residual developer. Then, the plate was transferred into the chromium etchant to remove the chromium coating that was not covered by the PR (Figure 3.4(iv)). After 3 minutes, the plate was taken out from the etchant, rinsed with DI water and blow-dried with nitrogen gas to remove the residual etchant. The chromium coating shielded by the PR remained intact after the process. Following that, the remaining PR on the plate was stripped by immersing the plate in PR remover for 3 minutes (Figure 3.4(v)). Finally, the plate was again rinsed by DI water and blow-dried by nitrogen gas after the stripping process to remove the residual PR remover. This completed the photolithography process where the pattern has been transferred from the photomask onto the chromium layer. Figure 3.7 shows the plate coated with the chromium phase pattern after the above processes.

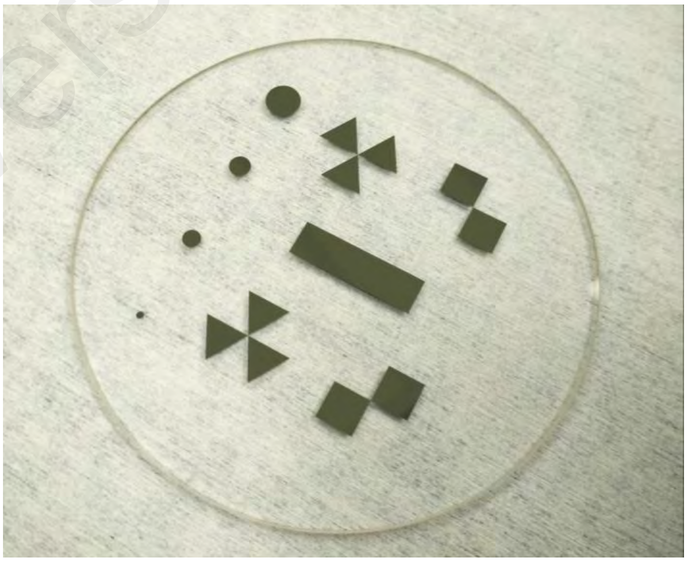

Figure 3.7: The circular fused silica plate after the photolithography and chemical wet etching process.

Following that, the plate was loaded into the vacuum chamber of the ICP etching system. The chamber's pressure was then pumped down to 10^{-5} Torr by rotary and turbomolecular pump. After that, hexafluoroethane (C_2F_6) and hydrogen gas were flowed into the chamber at flow rates of 30 sccm and 8 sccm respectively. This led to a chamber pressure of 10 mTorr. A radio frequency (RF) power generator was used to generate C_2F_6 and H_2 plasmas above the plate. Meanwhile, the stage that hold the plate in the chamber was negatively-biased to attract the ions from the C_2F_6 plasma towards the plate. The area on the plate which was not protected by the chromium pattern was etched by the C_2F_6 plasma through physical and chemical process. This will lead to the formation of protruded pattern on the plate upon the completion of ICP dry etching process (Figure 3.4(v)). The etch depth of the plate can be controlled by adjusting the etching rate and period of the dry etching process.

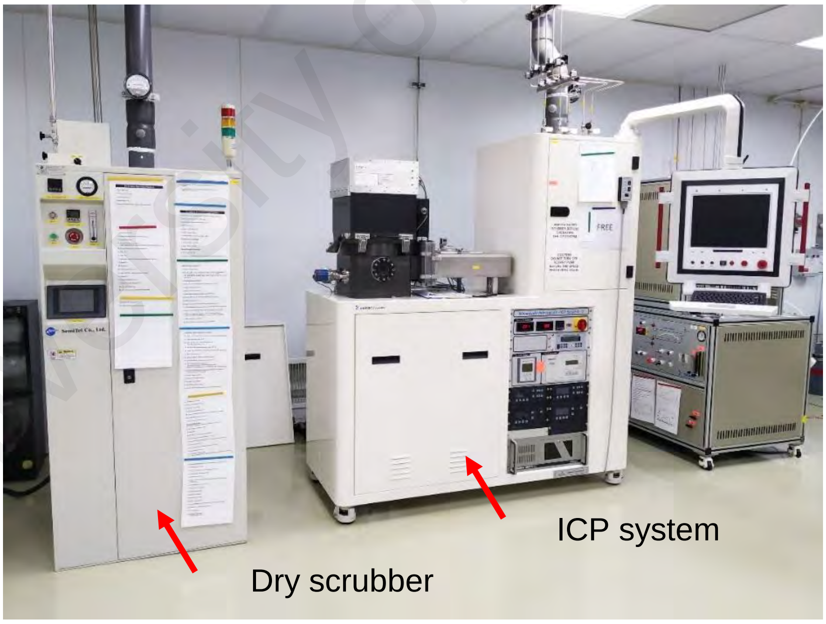

Figure 3.8: The ICP system used to perform dry etching on the circular fused silica glass plate and the scrubber to filter the greenhouse gases.

In the physical etching process, energetic ions from the plasma bombard the plate and remove the fused silica particles. Meanwhile, the chemical etching process occurs when the reactive species in the plasma diffuse towards the fused silica surface and react with the fused silica. The reaction will form light and volatile species which will desorb from the plate back to the ambient. Oxygen radicals are among the by-products of the chemical etching process. The radicals will react with the chromium layer to form chromium oxide which might evaporate from the layer. This will reduce the thickness of the chromium layer.

To mitigate this problem, H_2 gas was flown into the chamber to react with the oxygen radicals and converts the radicals into water molecules. This is expected to minimise the etching of the chromium layer caused by the oxygen radicals and avoid the need to deposit a thick layer of chromium on the plate. Besides cost saving consideration, a thinner chromium layer can ease the wet etching process by chromium etchant before and after the ICP dry etching process.

Fluorocarbon and hydrofluorocarbon by-products which are known to be potent greenhouse gases might be produced from the dry etching process due to the use of C_2F_6 gas. Therefore, the gas evacuated by the vacuum pump from the ICP chamber was filtered by a dry scrubber to remove the greenhouse gases. After the etching process, the chromium pattern on the plate was removed by immersing the plate in chromium etchant for 3 minutes (Figure 3.4(vi)). Then, the plate was cleaned by DI water and blow-dried using nitrogen gas. This completed the fabrication process of BPP on the fused silica plate.

The height of the protruded area relative to the non-protruded area is equivalent to the phase pattern thickness, *d*. The phase pattern thicknesses of the fused silica BPPs fabricated by the above procedures were measured by using a stylus surface profiler (Veeco, Dektak15). In the measurement, the plate was first positioned on the sample stage of the profiler where the plate's surface consisted of the phase pattern was facing upward.

The profiler was connected to a computer and the stylus on the profiler was lowered near to the plate's surface through the control software in the computer. A camera located above the stylus allows real-time monitoring of the plate's surface on the computer when the stylus is near to the plate. Then, the x-y position of the sample stage was manually adjusted until the edge of the phase pattern to be measured was within the line scanning length of the stylus. The line scanning length and the scanning resolution was set at 1000 μm and 0.1 μm/sample respectively. The measurement was performed at multiple spots along the edge with a gap of ~250 μm between adjacent measurements. This is illustrated in Figure 3.9.

After each measurement, the stage was moved laterally for ~250 μm before the next scanning was started. Five adjacent measurements were made and the average phase pattern thickness was determined. Besides, the standard deviation of the measurements was calculated. Due to imperfection in the fabrication process, the phase pattern thickness might slightly vary along the edge. Through the measurement, the section of the phase pattern's edge with small standard deviation was identified and used in the following experimental work.

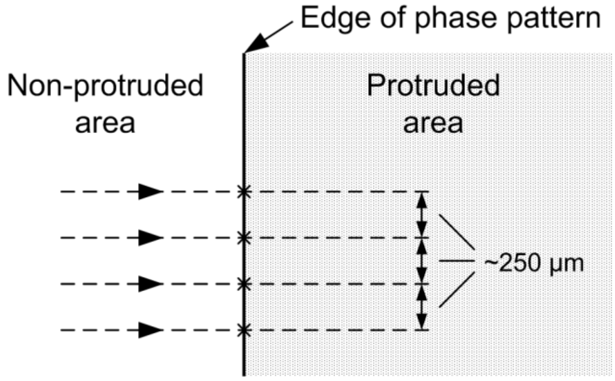

Figure 3.9: Line scanning of stylus surface profiler at multiple spots along the edge of phase pattern.

A typical result of line scanning across the edge of the phase pattern is shown in Figure 3.10. From the result, the phase pattern thickness is determined by taking the difference between the height of the non-protruded and protruded area. Based on the measurement, the two BPPs fabricated in this work have average phase pattern thickness, d_{avg} of 1.733 µm and 1.729 µm respectively. The standard deviation for the measurements is 0.002 µm for both BPPs. In the following discussion, the BPP with d_{avg} of 1.733 µm and 1.729 µm will be denoted as BPP-1 and BPP-2 respectively.

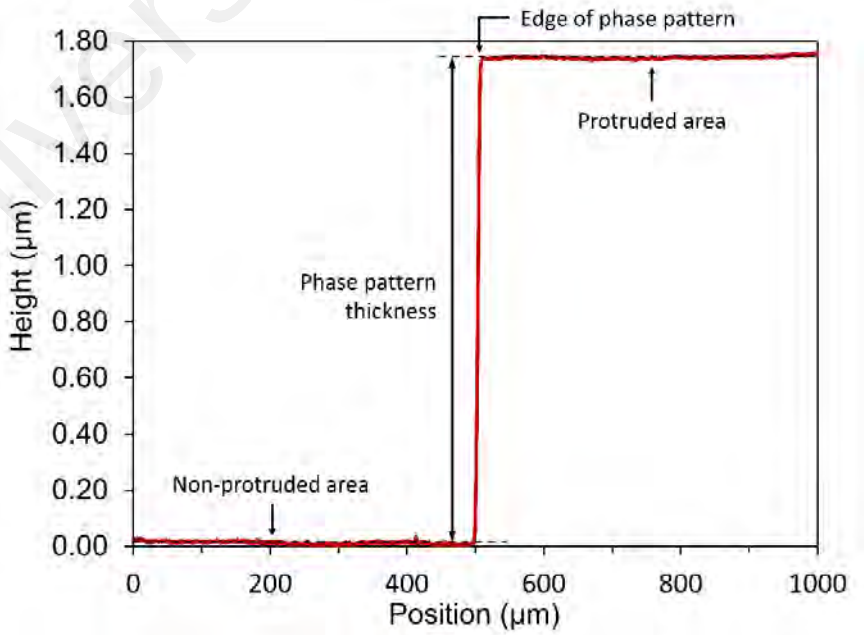

Figure 3.10: Typical profile of line scanning across the phase pattern edge by the stylus surface profiler.

3.2.2 Selective Mode Conversion and Excitation by Fused Silica BPP

Based on the average phase pattern thicknesses (1.733 µm and 1.729 µm) of the two LP_{11} BPPs, the matched wavelengths of the BPPs at different tilt angles were calculated by equation (3.20). Then, the experimental setup shown in Figure 3.11 is used to verify the mode conversion performance of the tilted BPP when the operating wavelength was deviated from the calculated matched wavelength. Only one BPP was used in the experiment at one time.

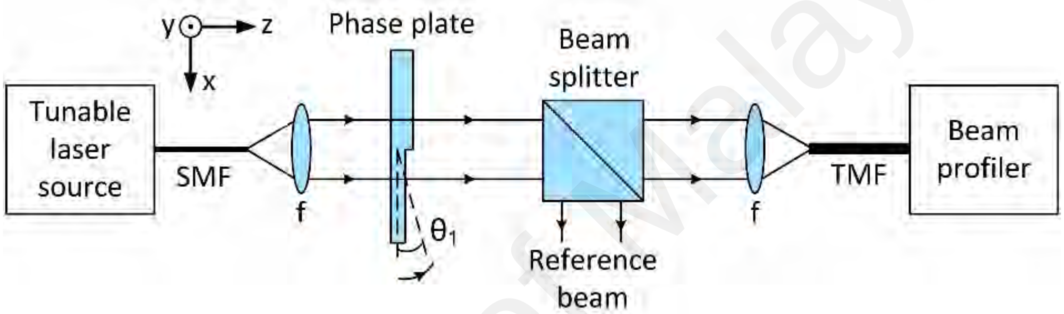

Figure 3.11: Schematic of the experimental setup used for the characterization of tilted BPP mode conversion performance.

Prior to the experiment, the relative position of the fiber and lenses was aligned to obtain: (i) a collimated beam between the two lenses shown in Figure 3.11 and (ii) maximum power at the TMF output. A tunable laser source (Santec, ECL-210; TLS) was employed as the light source because it can provide a monochromatic light with a linewidth as low as 1.6 pm in the wavelength range of 1530 – 1610 nm. Laser from the TLS was guided by a SMF towards an objective lens which collimated the output beam of the SMF. The SMF was clamped by the fiber holder on a fiber launch system where the position of the fiber end face relative to the objective lens was adjusted by a 3-axis linear stage. Since SMF only supports LP_{01} mode, the collimated beam has field distribution similar to the LP_{01} mode. The collimated beam was coupled by a second objective lens into the core of a step-index TMF held on a second fiber launch system.

This excited the LP_{11}^{even} mode in the TMF. The focal length of the objective lenses is 6.24 mm. The fiber launch systems were locked on an optical breadboard by screws. The distance between the SMF and the first lens was adjusted to obtain the collimated beam. Meanwhile, the position of the SMF in x- and y-direction was adjusted so that the beam collimated by the first lens propagated straight (in z-direction) towards the second lens. On the other hand, the position of the TMF relative to the second lens was adjusted while monitoring the TMF output power by a power meter (ILX Lightwave, OMM-6810B) in order to achieve the maximum output power.

Following the alignment process, the BPP and a 50:50 non-polarising beam splitter (BS) were added into the setup between the two lenses. The BPP was held by a stainless steel holder which was positioned on top of a linear stage. The stage was used to adjust the lateral position (x-direction) of the BPP. Lines with different angular orientation with respect to the z-direction were marked on the linear stage to provide guidance for BPP orientation. The BPP was oriented to different tilt angles by following the lines. The collimated LP_{01}-like beam transmitted through the BPP tilted to a specific angle was converted into a two-lobe LP_{11}-like beam. After that, the converted beam passed through the BS where half of the beam power was tapped as reference beam for monitoring purpose by a mode profiler. The remaining power of the beam transmitted through the BS was focused and coupled by the second objective lens into the TMF to excite the LP_{11} mode in the fiber. A mode profiler (Newport, LBP2-IR) was used to characterise the output beam of the TMF. The profiler has a phosphor-coated charge-coupled device (CCD) sensor which allows it to detect electromagnetic radiation in the wavelength range of 1440-1605 nm. The sensor has a pixel number of 640 × 480 where the size of each pixel is 9.9 × 9.9 μm.

With the TLS operating wavelength set to the matched wavelength of the corresponding tilt angle, the lateral position of the BPP was adjusted until a LP_{11}-like beam with highest symmetricity was observed at both the TMF output and the BS reference beam. It is necessary to monitor both the TMF output beam and the BS reference beam because the TMF output beam might be different from the converted beam of BPP due to cross-coupling of LP modes in the TMF. When the adjustment was done, the LP_{11}-like beam at the TMF output was recorded by the mode profiler. Then, the TLS operating wavelength was changed while maintaining the tilt angle of the BPP and the alignment and position of other components in the experimental setup. The operating wavelength was adjusted within the range of ± 0.5 nm about the matched wavelength at an interval of 0.1 nm. At different operating wavelength, the TMF output beam profile was recorded. Following that, the recorded beam profiles were analysed to estimate the change in LP_{11} mode composition when the operating wavelength deviated from the matched wavelength. The above procedures were repeated for four BPP tilt angles (0º, 2.5º, 5.0º and 7.5º) and two BPP with different average phase pattern thicknesses (1.733 μm and 1.729 μm).

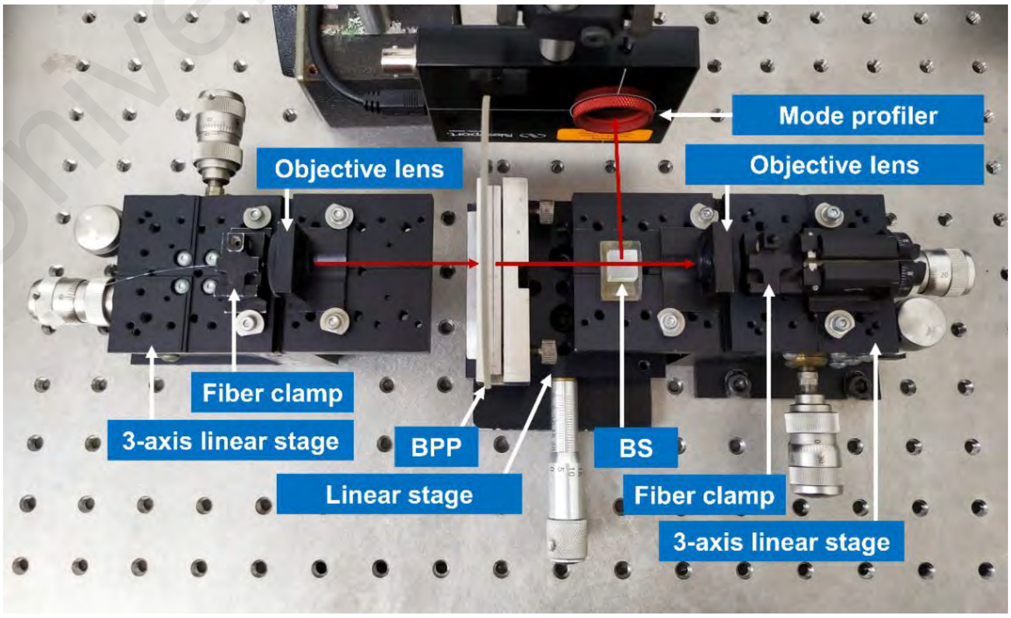

Figure 3.12: BPP mode conversion system.

3.3 Results and Discussions

3.3.1 Mode Conversion and Excitation Performance of Tilted Fused Silica BPP

Based on the average phase pattern thicknesses of the two BPPs, the matched wavelengths at different tilt angles were calculated by equation (3.20). The change in the matched wavelength with respect to the BPP tilt angle is depicted in Figure 3.13. When the BPP tilt angle increased from 0º to 7.5º, the matched wavelength increased as much as 9.16 nm and 9.14 nm for BPP-1 and BPP-2 respectively.

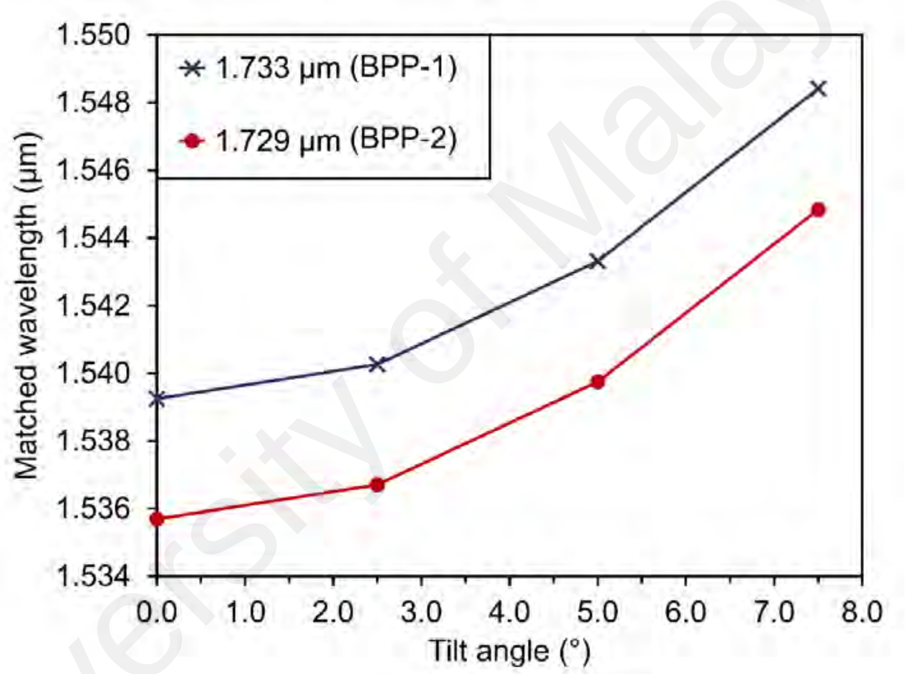

Figure 3.13: Relationship between the matched wavelength and BPP tilt angle for different phase pattern thicknesses.

Then, by using the experimental procedure discussed in Section 3.2.2, the mode conversion performance of the tilted BPP at the calculated matched wavelength was evaluated by analysing the output beam of a TMF under the excitation of the converted beam. Firstly, the TMF output beams at different operating wavelengths for the case of BPP-1 tilted at $\theta_1 = 5°$ are shown on the right of Figure 3.14. When the phase pattern's edge of the BPP was not in the beam propagation path, the LP_{01} mode was not converted into LP_{11}-like beam by the BPP. Therefore, LP_{01} mode was excited in the TMF and observed at the TMF output (Figure 3.14(a)). After that, the BPP was laterally aligned such that its phase pattern's edge intercepted with the beam propagation path to convert the beam into a symmetry LP_{11}-like beam. At the matched wavelength of 1543.32 nm, symmetry LP_{11} mode was observed at the TMF output when the TMF was excited by the converted beam (Figure 3.14(c)). Based on numerical method-based modal content analysis as described in Section 4.2.3, the mode profile shown in Figure 3.14(c) is estimated to have LP_{11} mode purity > 98%. However, when the TLS operating wavelength was deviated from the matched wavelength while maintaining the physical alignment and position of all components in the experimental setup, the output beam was observed to become asymmetry (Figure 3.14(b) and (d)).

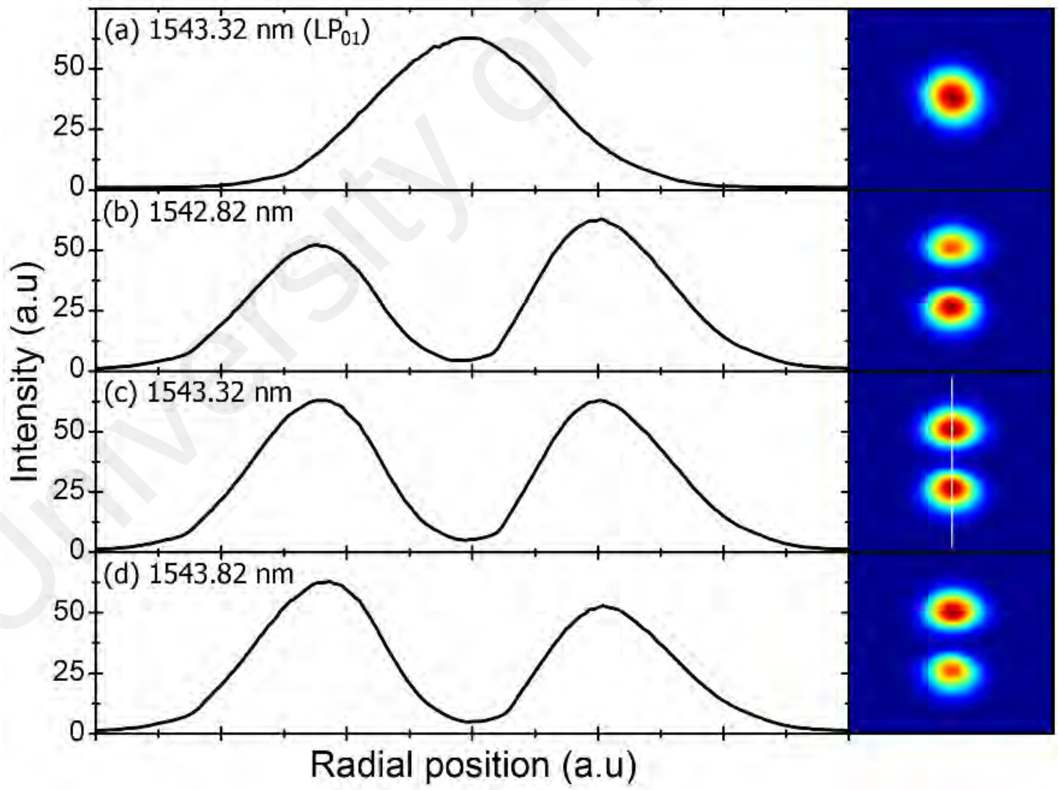

Figure 3.14: 1-D and 2-D intensity profiles of LP_{01} and LP_{11} mode at TMF output obtained under different operating wavelength (BPP-1 at θ_1 = 5.0°).

The 1-D profiles shown on the left of Figure 3.14 represent the intensity profile along a line that crossed the peak(s) of the beams. This is illustrated by the white line in the two-dimensional (2-D) profile in Figure 3.14(c). It can be seen that the intensity of the two peaks is almost the same for LP_{11} mode at matched wavelength. In contrast, the intensity profile becomes asymmetry when the TLS operating wavelength deviated from the matched wavelength (Figure 3.14(b) and (d)). The asymmetry intensity profile indicates that part of the converted beam's power was coupled into the LP_{01} mode in the TMF. Since the parameters and condition of the experimental setup were fixed except for the TLS operating wavelength, the asymmetry intensity profile suggests that the deviation in operating wavelength led to inefficient conversion and excitation of LP_{11} mode in the TMF. While the results in Figure 3.14 correspond to BPP-1 tilted at $\theta_1 = 5.0°$, similar evolution in the TMF output beam profile was observed in other cases where different tilt angle ($\theta_1 = 0°, 2.5°, 7.5°$) and BPP (BPP-2) were used.

To quantify the LP_{11} mode symmetricity observed at the TMF output for the cases of different operating wavelength, tilt angle and BPP, the lobes intensity difference, LID, is introduced in this work. It is defined by the following equation:

$$\text{Lobes intensity difference, LID} = \left(\frac{P_1 - P_2}{P_1 + P_2}\right)^2 \tag{3.21}$$

where P_1 and P_2 are the peak intensity of the two lobes of a LP_{11} beam. P_1 and P_2 were determined from the 1-D intensity profiles of the LP_{11} beams recorded by mode profiler. The LIDs calculated for LP_{11} beam profiles recorded at different tilt angles, TLS operating wavelengths and phase pattern thicknesses are shown in Figure 3.15. For asymmetry LP_{11} beam, difference between P_1 and P_2 is larger and therefore the value of LID is higher as compared to the LID for symmetry LP_{11} beam. This can be seen in Figure 3.15 where the LID increases when the TLS operating wavelength deviated from the matched wavelength of the corresponding tilt angle. When the matched wavelength is applied on the TLS, symmetry LP_{11} beam is observed and the LID is near to zero.

For the cases of different tilt angle and BPP, the wavelengths at which the lowest LID occur are determined and marked by the blue crosses with respect to the corresponding tilt angle on the secondary y-axis. The wavelengths are equivalent to the experimentally-determined matched wavelength at the different BPP tilt angle. Meanwhile, the calculated matched wavelengths at different tilt angle are shown in the same figure by the solid blue lines. As observed in the figure, the measured matched wavelengths are located on the solid blue lines. This indicates that the experimental observation agrees well with the values calculated by equation (3.20). Results in Figure 3.15 validated equation (3.20) derived in Section 3.1.1 which suggest that the BPP operating wavelength range for efficient mode conversion and excitation can be extended by tilting the BPP to an angle relative to the light propagation direction.

Although tilting the BPP with a fixed phase pattern thickness can allow the BPP to operate at longer matched wavelength, there is a limit on the shortest achievable matched wavelength for the BPP. This is because tilting the BPP to $\theta_1 > 0^o$ can only increase the OPD across the BPP but not the opposite. Therefore, shortest matched wavelength of the BPP for efficient mode conversion and excitation is the design wavelength of the BPP.

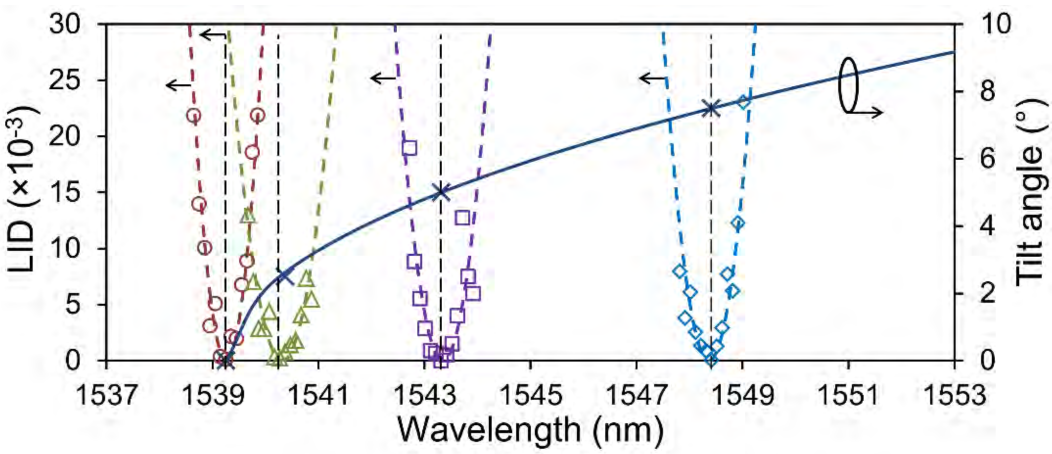

(a)

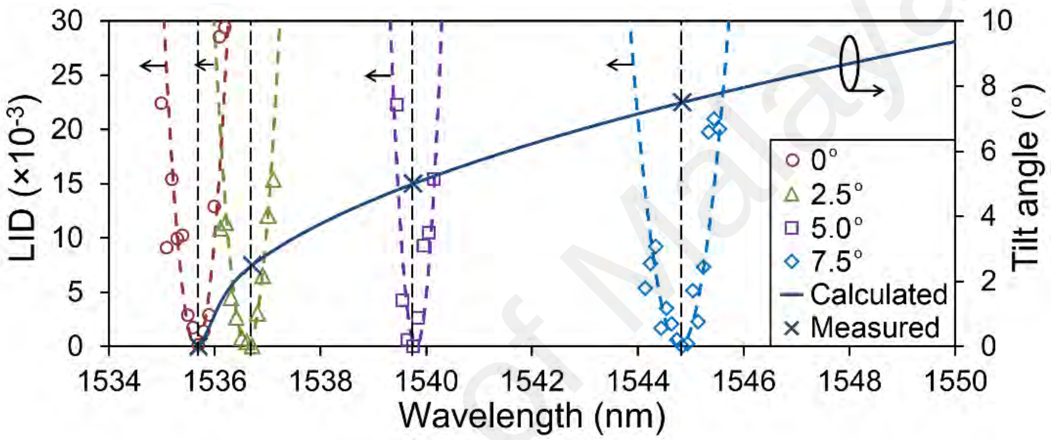

(b)

Figure 3.15: LID for LP_{11} mode obtained under different BPP, tilt angle and operating wavelength: (a) BPP-1 and (b) BPP-2.

While the largest tilt angle applied in this work is 7.5º, it is possible to further increase it and to expand the operating wavelength range of the BPP for efficient mode conversion and excitation. However, undesired reflection of the incident beam at the air-BPP and BPP-air interface might increase at larger tilt angle due to the Fresnel effect. This will reduce the beam power to be coupled into the TMF. Besides, Fresnel reflection is polarisation dependent at large incident angles (Table 3.1). This will lead to different transmitted power for incident beam with different polarisations. Hence, the tilt angle should be limited to a reasonable range to avoid such complication.

Table 3.1: Polarisation dependent loss due to Fresnel reflection at different tilt angle.

Tilt angle (°)	Reflectance (%)					
	air-BPP interface		BPP-air interface		Total	
	x-pol.	y-pol.	x-pol.	y-pol.	x-pol.	y-pol.
0	3.3	3.3	3.3	3.3	6.6	6.6
7.5	3.2	3.4	3.1	3.5	6.3	6.9
10.0	3.2	3.4	3.0	3.6	6.2	7.0
20.0	2.7	3.9	2.1	4.8	4.8	8.7
30.0	2.0	4.8	0.5	8.3	2.5	13.1

As discussed in Section 3.1, the slope width, *s*, of the BPP might affect the symmetricity of the converted beam when it is too large. The slope width of the BPP used in this work is approximately 4 μm (measurement by stylus surface profiler). This is about two order of magnitude smaller than the slope width reported by Igarashi et al. (~200 μm) at which symmetricity of the converted beam has been affected by the large slope width. Meanwhile, when the BPP tilt angle is increased from 0° to 7.5°, the overlapping width between the incident beam and the slope increases from 4 μm to about 4.2 μm as illustrated in Figure 3.16(a) and (b). The increment is small compared to the incident beam diameter of about 2 mm. Therefore, the influence of BPP slope width is assumed to be small in this work.

The BPP has been tilted in counter-clockwise direction in this work (Figure 3.16(b)) but the same mode conversion and excitation performance can be achieved by tilting the BPP in clockwise direction (Figure 3.16(c)). This is possible because the OPD is same in both cases as long as the same tilt angle is applied. The overlapping width of the incident beam and the slope will reduce when the BPP is tilted in clockwise direction. However, its effect on the mode conversion and excitation performance of the BPP is negligible based on the discussion in the previous paragraph. In spite of that, the tilt in clockwise

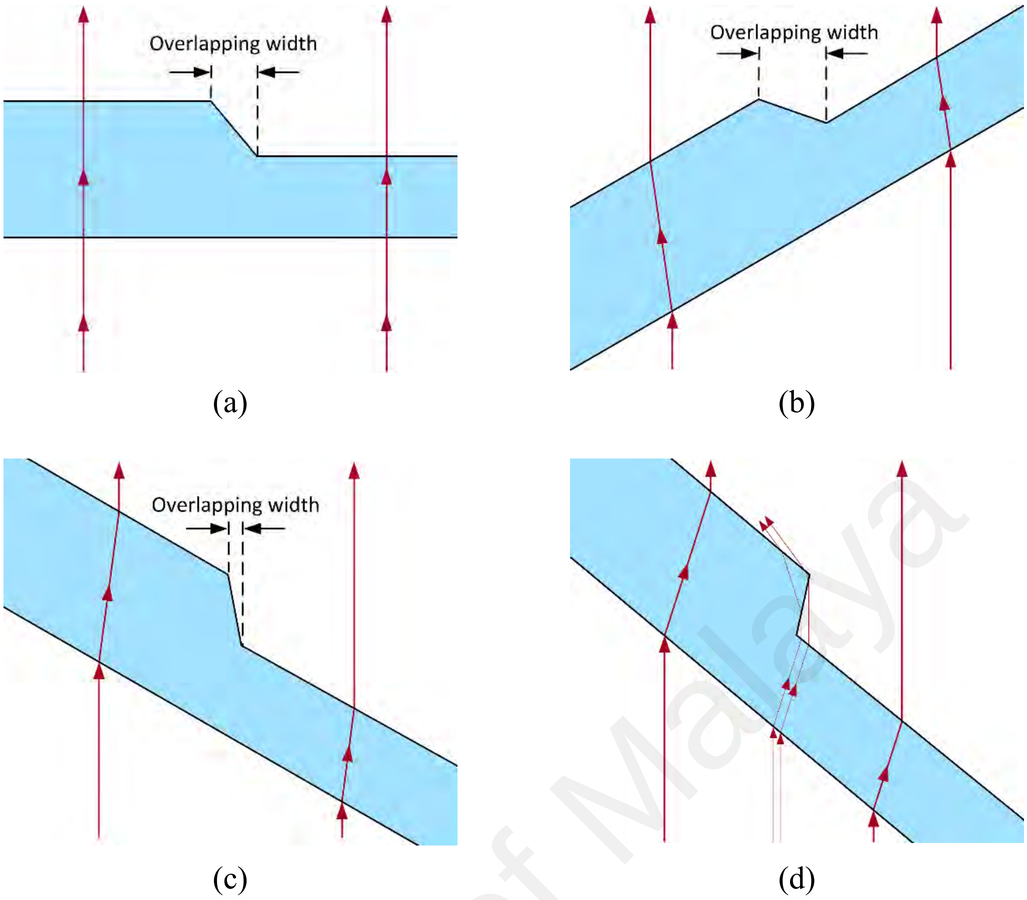

Figure 3.16: Overlapping width of the incident beam and the phase pattern's edge with slope width of *s* for: (a) non-tilted BPP, (b) BPP tilted in counter-clockwise direction, and (c,d) BPP tilted in clockwise-direction.

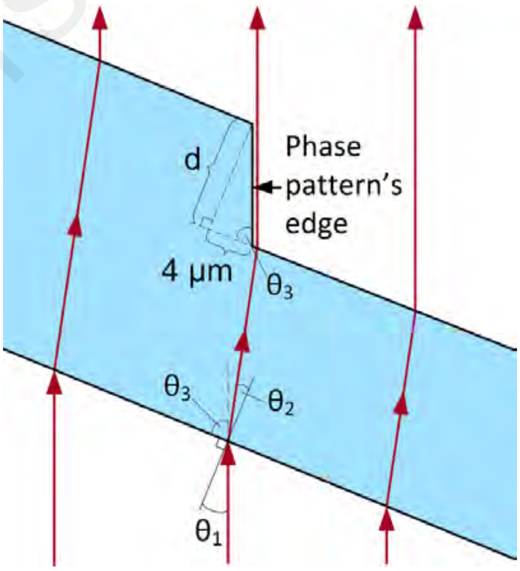

Figure 3.17: The maximum allowable tilt angle for a BPP tilted in clockwise direction.

direction might refract a portion of light away from the principle light propagation direction if the tilt angle is too large (Figure 3.16(d)). This should be avoided to prevent power loss.

The maximum allowable tilt angle to avoid the situation in Figure 3.16(d) is when the phase pattern's edge aligns parallel to the light propagation direction where the overlapping width is reduced to zero. This is depicted in Figure 3.17 where the slope width, s is taken as 4 μm. From the figure, the following relationships can be obtained:

$$\tan\theta_3 = \frac{d}{(4\ \mu\mathrm{m})} \tag{3.22}$$

$$\theta_1 + \theta_3 = 90^{\mathrm{o}} \tag{3.23}$$

For BPP-1 and BPP-2 with d = 1.733 μm and 1.729 μm, the θ_3 calculated by equation (3.22) is 23.4°. Then, by using equation (3.23), θ_1 = 66.6°. Therefore, if the BPPs used in this work are tilted in clockwise direction, 66.6° is the maximum allowable tilt angle to avoid the situation in Figure 3.16(d).

On the other hand, the beam transmitted across the tilted BPP might be shifted laterally away from the centre axis of the incident beam due to refraction in the BPP as denoted by x_1' and x_2' in Figure 3.3. By using equations (3.8), (3.11), (3.14) and (3.15), the following relationships can be obtained:

$$x_1' = (d + d_1)\left[\frac{\sin(\theta_1 - \theta_2)}{\cos\theta_2}\right] \tag{3.24}$$

$$x_2' = d\left[\frac{\sin(\theta_1 - \theta_2)}{\cos\theta_2}\right] \tag{3.25}$$

Then, the lateral shifts (x_1' and x_2') in the beam propagation path calculated by equations (3.24) and (3.25) are about 27 μm, 54 μm and 81 μm at tilt angle of 2.5°, 5.0° and 7.5° respectively. Since the shifts are small compared to the beam diameter of about 2 mm, its effect is assumed to be negligible. Although the shift for the ray transmitted through the protruded area (x'_1) is larger than that through the un-protruded area (x'_2), their difference is less than 0.1 µm for the phase pattern thicknesses (1.733 µm and 1.729 µm), tilt angles and tilt direction applied in this work (0°, 2.5°, 5.0° and 7.5° in counter-clockwise direction). It is possible to reduce the lateral shift distance by almost a half if the overall thickness of the BPP is reduced from 2 mm to 1 mm while maintaining the phase pattern thickness. From Figure 3.3, the overall thickness of the BPP, $D = (d + d_1)$ where d is the phase pattern thickness. When D is reduced while d remains the same, d_1 will decrease. According to equation (3.24), x'_1 will become smaller when d_1 decreases. As shown in equations (3.18) and (3.19), reduction in d_1 will not affect the OPD and phase shift introduced by the BPPs as long as d remains the same.

3.3.2 Estimation of LP_{11} Mode Purity via the Comparison of LID between Simulated and Measured 1-D LP_{11} Intensity Profile

The normalised E-field distribution functions for LP_{01} and LP_{11} modes are given by the following equations (Buck, 2004):

$$\tilde{E}_{01} = \begin{cases} E_{01} J_0\left(\frac{u \cdot r}{a}\right) & r \leq a \\ E_{01}\left(\frac{J_0(u)}{K_0(w)}\right) K_0\left(\frac{w \cdot r}{a}\right) & r \geq a \end{cases} \tag{3.26}$$

$$\tilde{E}_{11} = \begin{cases} E_{11} J_1\left(\frac{u \cdot r}{a}\right)\cos(\phi) & r \leq a \\ E_{11}\left(\frac{J_1(u)}{K_1(w)}\right) K_1\left(\frac{w \cdot r}{a}\right)\cos(\phi) & r \geq a \end{cases} \tag{3.27}$$

where $\tilde{E}_{01}$ and $\tilde{E}_{11}$ are the E-field distributions of LP_{01} and LP_{11} mode respectively as the functions of radius, r and azimuthal position, ϕ. Meanwhile, J_l is the Bessel's function of the first kind, K_l is the Bessel's function of second kind with $u = ka(n_{core}^2 - n_v^2)^{1/2}$, $w = ka\left(n_v^2 - n_{cladding}^2\right)^{1/2}$ and $k = 2\pi/\lambda$. On the other hand, E_{01} and E_{11} are constant coefficients, n_{core} and n_{cladding} are the core and cladding RIs respectively, a is the fiber core radius (9.25 µm), n_v is the effective index of LP_{01} or LP_{11} modes, where $v \in \{01, 11\}$. The effective indices of LP_{01} and LP_{11} modes are 1.4474 and 1.4461 respectively while the RI of fiber core and cladding are 1.4484 and 1.4434 respectively. By taking the absolute square of the normalised E-field distribution function given in equations (3.26) and (3.27), the normalised 2-D LP_{01} and LP_{11} mode intensity profiles can be simulated where the total power of the simulated modes is normalised to unity and satisfied the following equation:

$$P_{01} = \iint_{A_\infty} \left|\tilde{E}_{01}\right|^2 dA = P_{11} = \iint_{A_\infty} \left|\tilde{E}_{11}\right|^2 dA = 1 \tag{3.28}$$

where P_{01} and P_{11} are the power of the LP_{01} and LP_{11} modes respectively, A is the area of the fiber and A_∞ is the cross-sectional area of the fiber which extends to infinity. On the other hand, the intensity profile of an asymmetry LP_{11} mode which is due to the co-existence of both LP_{01} and LP_{11} modes is defined as:

$$\begin{aligned} I &= \left|a\sqrt{\rho}\,\tilde{E}_{01} + b\sqrt{(1-\rho)}\,\tilde{E}_{11}\right|^2 \\ &= \left|a^2\rho\,\tilde{E}_{01}^2 + b^2(1-\rho)\tilde{E}_{11}^2 + 2ab\sqrt{\rho(1-\rho)}\left(\tilde{E}_{01}\cdot\tilde{E}_{11}\right)\right| \end{aligned} \tag{3.29}$$

where ρ is the composition of LP_{01} mode with $\rho \in [0, 1]$ while a and b are the complex coefficient with $|a| = |b| = 1$. Then, the total power of the asymmetry LP_{11} beam is given by:

$$\begin{aligned} P_{total} &= \iint_{A_\infty} I\, dA \\ &= \rho \iint_{A_\infty} \left|\tilde{E}_{01}\right|^2 dA + (1-\rho) \iint_{A_\infty} \left|\tilde{E}_{11}\right|^2 dA \\ &= \rho P_{01} + (1-\rho)P_{11} \\ &= 1 \end{aligned} \tag{3.30}$$

Since LP_{01} and LP_{11} modes are orthogonal to each other, $\iint_{A_\infty} \tilde{E}_{01} \cdot \tilde{E}_{11}\, dA = 0$, and the third term in Equation (3.29) is null. Equation (3.30) shows that the total power of the asymmetry LP_{11} is normalised to unity when the power is calculated based on the intensity defined in equation (3.29). Therefore, regardless of ρ, the total power of the asymmetry intensity profile is constant. The corresponding 1-D intensity profiles for asymmetry LP_{11} beams with different LP_{01} composition ρ have been calculated based on equation (3.29) and shown in Figure 3.18. It can be seen that the symmetricity of LP_{11} beam reduces when the LP_{01} composition increases. The peak intensities of the 1-D intensity profiles have been determined and the LID of the simulated profiles is calculated. Then, the relation between the LP_{11} mode composition and the LID is plotted and shown in Figure 3.19.

The modal purity of the LP_{11} mode recorded in experiment can be estimated by matching its LID value with that shown in Figure 3.19. The maximum LID of the LP_{11} mode obtained from experiment is about 0.04 when the TLS operating wavelength deviated within the range of ± 0.5 nm from the matched wavelength. Based on the simulated result shown in Figure 3.19, LID value of 0.04 is corresponding to LP_{01}:LP_{11} mode composition of 0.0009:0.9991 which is equivalent to LP_{11} mode purity of about 30 dB. On the other hand, LIDs of LP_{11} mode obtained from experiment at matched wavelengths are in the range of 10^{-4} to 10^{-7}. This leads to LP_{11} mode purity ≥ 40 dB according to the relationship shown in Figure 3.19.

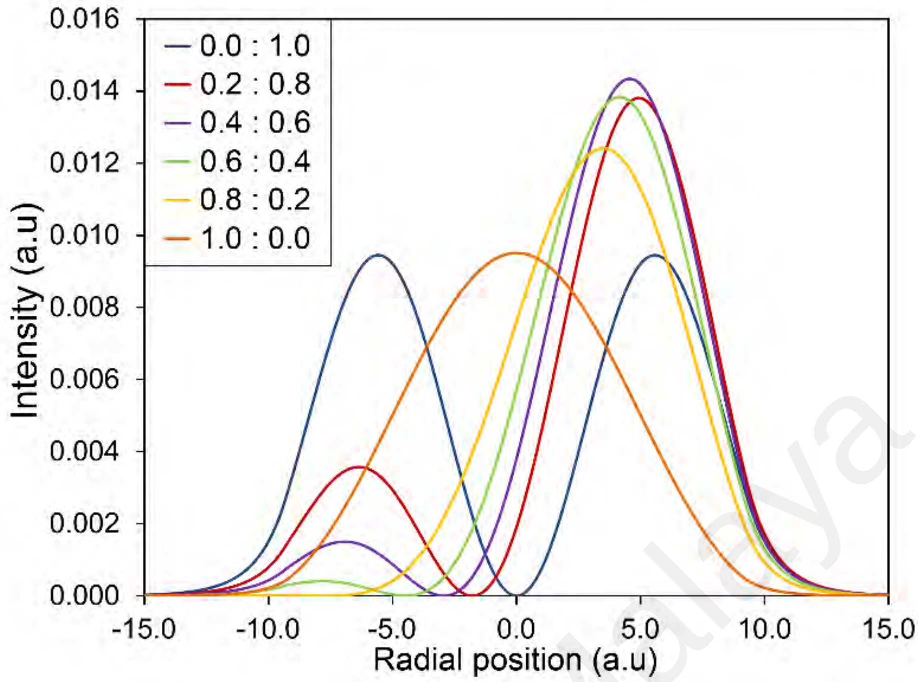

Figure 3.18: 1-D intensity profiles of asymmetry LP_{11} mode due to different LP_{01}:LP_{11} ratios.

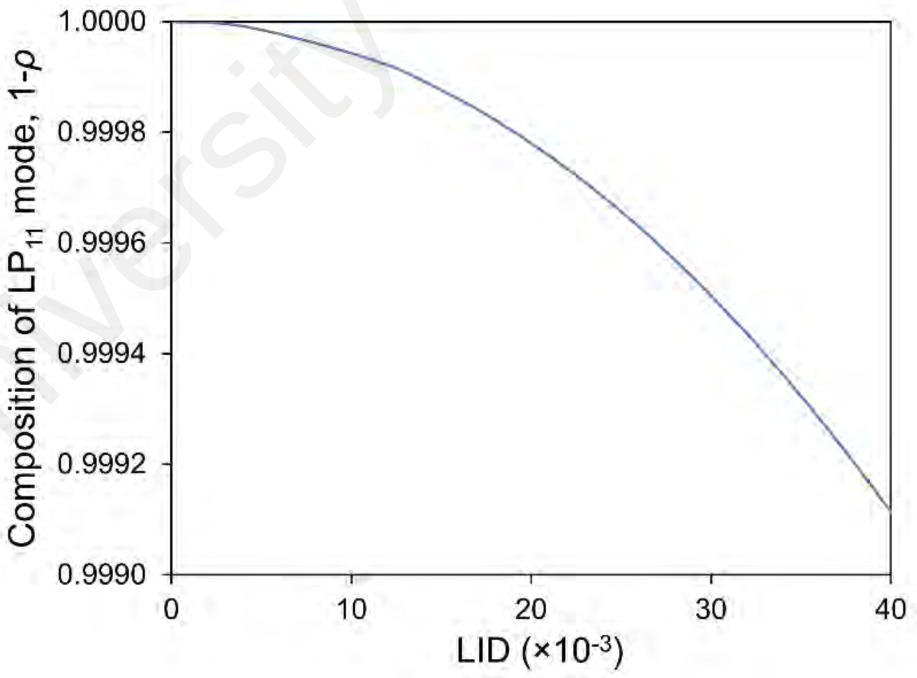

Figure 3.19: Relationship between the LP_{11} mode composition and the LID of an asymmetry LP_{11} mode profile.

3.4 Summary

In summary, a technique to extend the operating wavelength range of a BPP for efficient mode conversion has been proposed and demonstrated. The technique is based on the modification of OPD introduces by a BPP when the BPP is tilted to different angles. Firstly, the relationship between the BPP tilt angle, phase pattern thickness and matched wavelength at which a phase shift of π can be introduced by a tilted BPP has been derived based on geometrical optics. Then, two fused silica BPPs with phase pattern thicknesses of 1.733 μm and 1.729 μm were fabricated by photolithography, chemical wet etching and ICP dry etching processes. After that, the BPPs were used to verify the mode conversion performance of the tilted BPP technique.

From the experiment result, we observed that a BPP tilted to a specific angle can provide efficient $LP_{01} \rightarrow LP_{11}$ mode conversion at operating wavelength equal to the calculated matched wavelength for that tilt angle. When the operating wavelength deviated as much as ±0.5 nm from the matched wavelength, the symmetricity of the converted LP_{11} mode was observed to deteriorate. Tilting the BPP from 0° to 7.5° has allowed the BPP to extend its operating wavelength range for efficient mode conversion as much as 9.16 nm longer than the design wavelength. The effect of the slope width of the phase pattern, tilt direction of BPP and refraction in the tilted BPP on the mode conversion performance have been discussed.

Following that, 1-D intensity profile of impure LP_{11} modes with different LP_{01}:LP_{11} mode composition ratio were simulated. Comparison of the simulated intensity profile with that recorded from experiment allowed the estimation of the purity of LP_{11} mode obtained from experiment. Based on the comparison with the simulated intensity profile, the LP_{11} mode composition of the converted LP_{11} mode was close to 100% when the corresponding matched wavelength was applied at a specific tilt angle (high LP_{11} purity).

CHAPTER 4: DOWN-CONVERSION OF LP MODE BY AFTMF

Commonly, the end facet of a fiber is flat-cleaved to enable fusion splicing with another fiber. For certain applications, angled-cleaving is applied to reduce back-reflection at the fiber end facet. Wang et al. simulated the far-field intensity distribution of LP_{11} mode at the output of a two-mode fiber (TMF) with angled-facet (Wang, Wang, & Claus, 1993). It was observed that the two-lobe pattern at the TMF output becomes asymmetric when the facet angle increased to 30º. The two-lobe pattern might eventually reduce to a single-lobe beam if the facet angle is increased further. In this chapter, the feasibility of a TMF with angled output facet to perform efficient down-conversion of LP mode will be reported. By using the OptiFDTD simulator, simulations have been performed to determine the propagation characteristic of the beam at the output of TMF with different output facet angles. Based on the simulation result, an angled-facet TMF (AFTMF) was fabricated. Then, selective mode conversion and excitation with an AFTMF were experimentally demonstrated and characterised.

4.1 Simulation of Beam Propagation at TMF Output

Beam propagation at the output of TMFs with different output facet angles have been simulated by using OptiFDTD. Figure 4.1 depicts the model of AFTMF used in the simulation. The facet angle, θ is defined as the angle between the fiber axis and the normal axis of the facet. Meanwhile, the refracted angle of the TMF output beam, φ, is the angle between the propagation axis of the output beam and the normal axis of the facet. In the simulator, the diameter of the TMF core and cladding are 16 μm and 125 μm respectively. A graded-index TMF was used in the simulation in which the core has a gradually decreasing refractive index (RI) from 1.451 to 1.444 with increasing radial distance from the core centre.

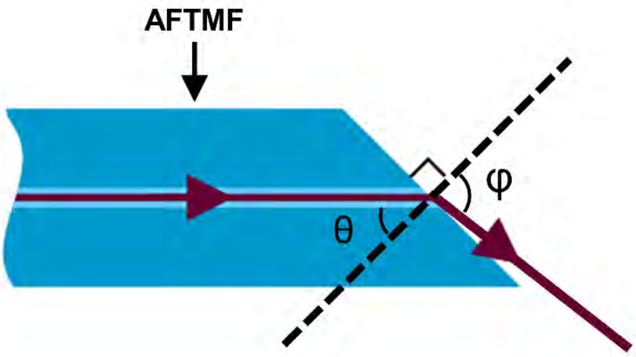

Figure 4.1: The AFTMF model used in the OptiFDTD simulation.

Based on the following equation, the RI at different radial distance in the core was calculated (Buck, 2004):

$$n(r) = n_1 \sqrt{1 - 2\Delta \left(\frac{r}{a}\right)^{\alpha}} \tag{4.1}$$

where n_1 and n_2 are the RI at the centre of the core and the cladding respectively, $\Delta \sim (n_1 - n_2) / n_1$, r is the radial distance from the core centre, a is the core radius and α is the profile parameter. The parameters being applied were: $\alpha = 2$, $a = 8$ µm, $n_1 = 1.451$ and $n_2 = 1.444$. This leads to an index profile shown in Figure 4.2.

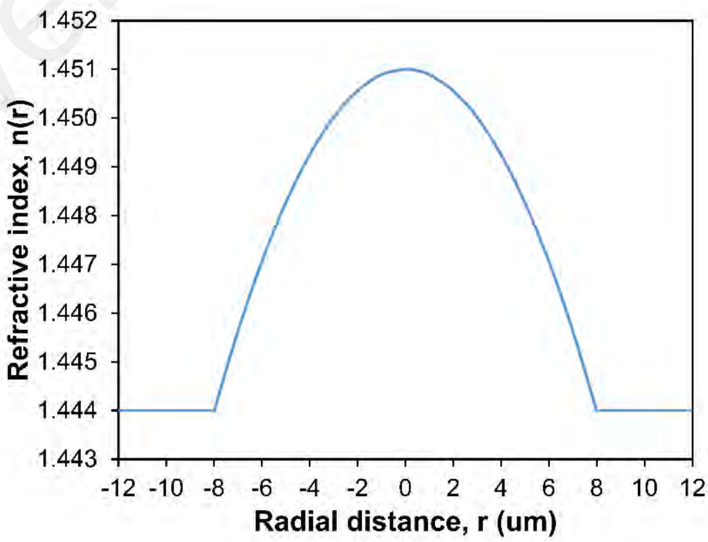

Figure 4.2: Parabolic graded index profile of a two-mode fiber.

In OptiFDTD, the graded-index profile of the core was approximated by a profile with discrete increment as shown in Figure 4.3. The discreteness can be reduced by increasing the number of step. However, larger number of step requires higher computing power. Besides, no significant difference has been observed in the simulated results when more than five steps were applied in the preliminary study. Therefore, five steps were applied to provide the gradual increment from 1.444 to 1.451 in this work. On the other hand, Figure 4.4 depicted the RI of the AFTMF model constructed in OptiFDTD where the region in blue colour surrounds the AFTMF representing air with RI of 1.0. Meanwhile, the green colour regions are corresponding to the cladding of the fiber with RI of 1.444.

The AFTMFs with different facet angles (0º – 43º) under the excitations of LP_{01} / LP_{11} modes have been used in the simulations. Figure 4.5 shows the propagation of beam in the AFTMF at different facet angles. In general, the refracted angle of the LP_{01} and LP_{11} output beam increases with increasing facet angle. Besides, it can be observed that one of the lobes in the LP_{11} output beam gradually diminished when the facet angle increases and eventually only one lobe remains. The lobes in the LP_{11} output beam will be labelled as Lobe 1 and Lobe 2 as shown in Figure 4.5 for the ease of discussion.

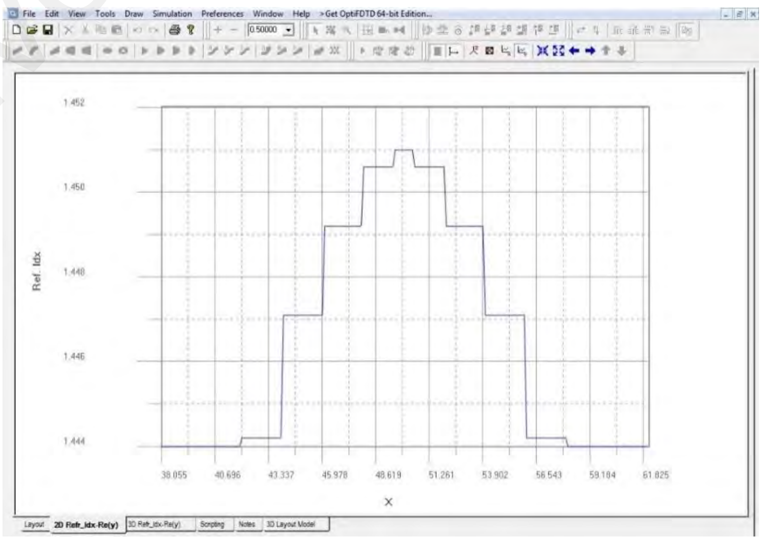

Figure 4.3: Interface of the OptiFDTD simulator showing the graded-index profile of the AFTMF core.

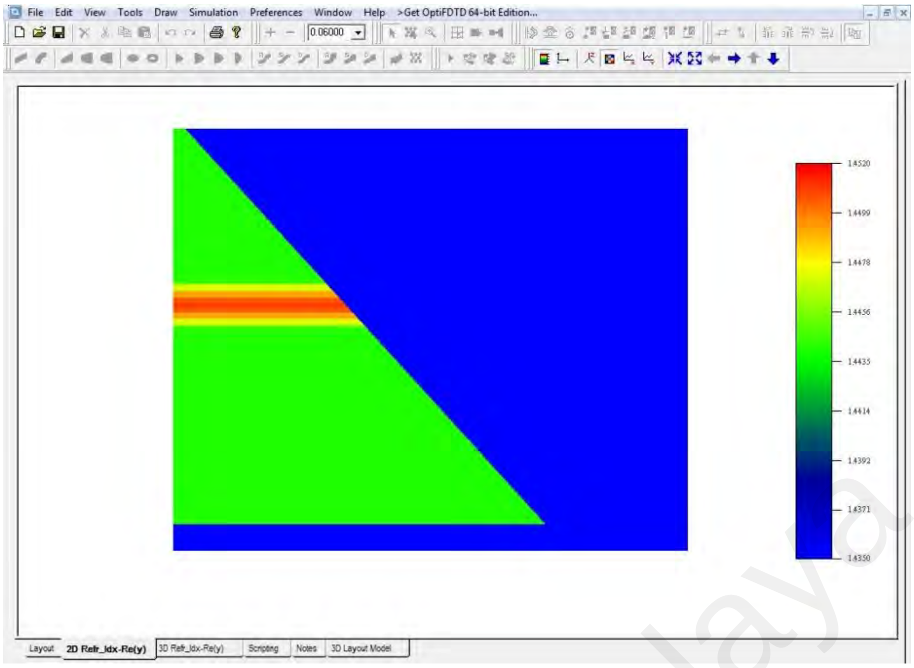

Figure 4.4: Interface of the OptiFDTD simulator showing the RI profile of the AFTMF.

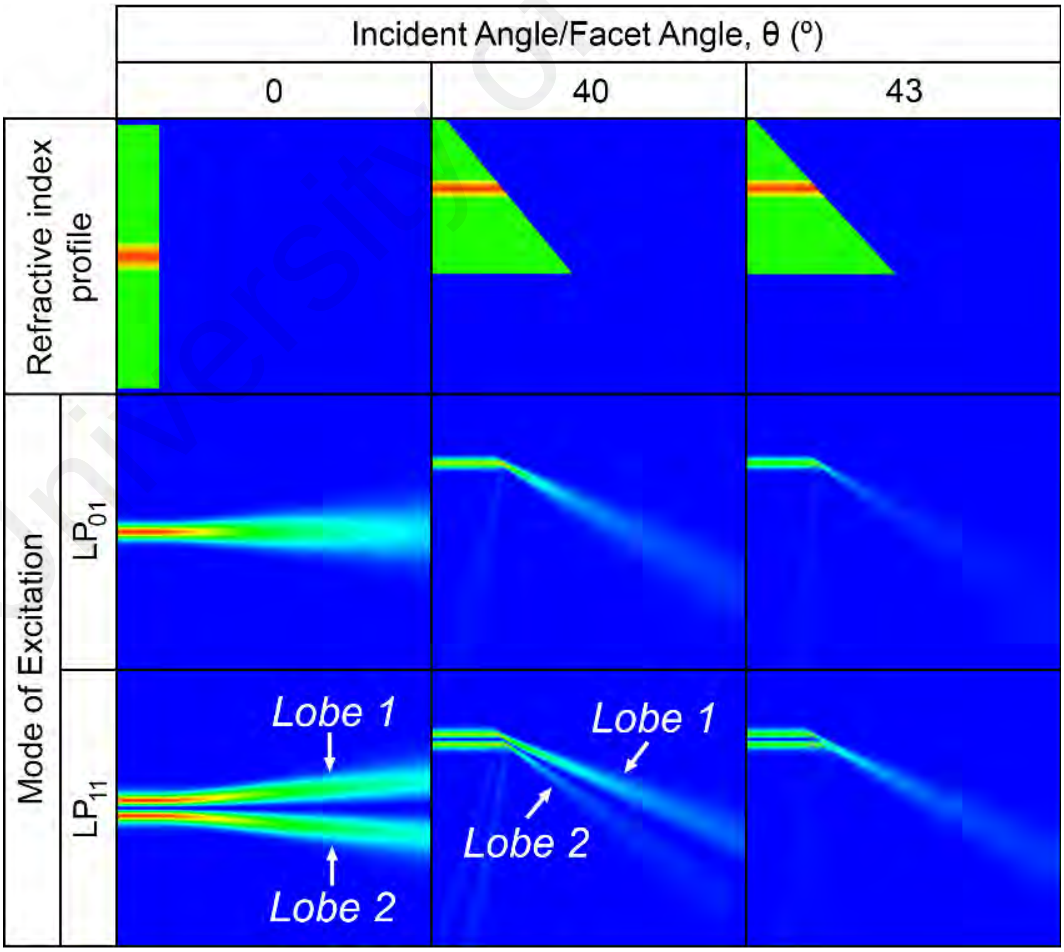

Figure 4.5: RI profile of TMF with different facet angles and the corresponding simulated beam propagation for the case of LP_{01} and LP_{11} mode excitation.

To determine the refracted angle, φ of the simulated beam at different facet angle, the simulated two-dimensional (2-D) beam propagation results were processed by image processing program in MATLAB. The algorithm performed a line scanning through the image at different z position as illustrated in Figure 4.6 to determine the point with highest intensity (marked by black '×' in Figure 4.6) along the scanning line. Linear equation corresponding to a straight line connected the crosses was deduced and the angle of the straight line relative to the fiber axis, θ' was determined. Then, the refracted angle of the beam is given by φ = θ + θ'.

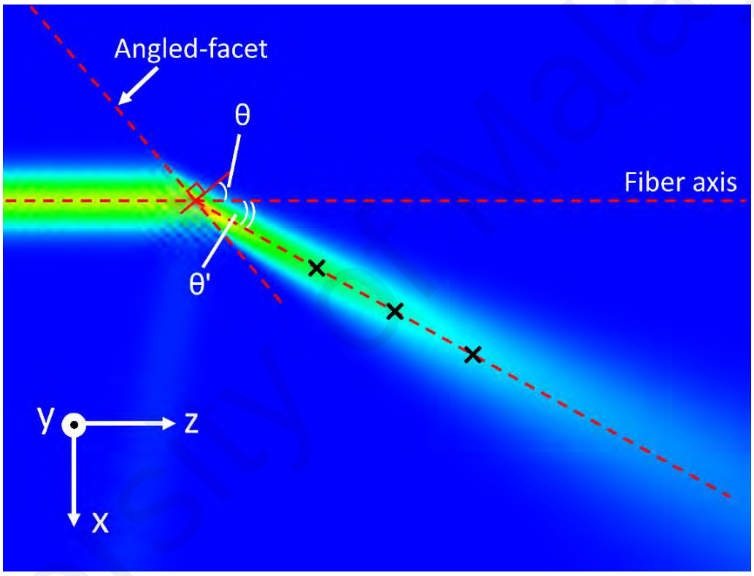

Figure 4.6: Determination of the refracted angle of the simulated AFTMF output beam with single lobe.

Illustration in Figure 4.6 is based on single-lobe output beam. However, for the output beam of LP_{11} mode, there are two local maxima intensity along each scanning line due to the two lobes. In this case, the refracted angle of each lobe was first determined. They are $(\theta + \theta_1)$ and $(\theta + \theta_3)$ as shown in Figure 4.7. Then, the refracted angle for the centre of the beam is defined as:

$$\theta_{centre} = \theta + \left(\frac{\theta_1 + \theta_3}{2}\right) \tag{4.2}$$

It is the middle point between the refracted angles for Lobe 1 and Lobe 2. At facet angle of 42.5º and higher, the two-lobe output beam turns into a single-lobe beam where Lobe 2 diminished while Lobe 1 becomes dominant. For these cases, the refracted angle is determined based on the method used for the case of LP_{01} output beam.

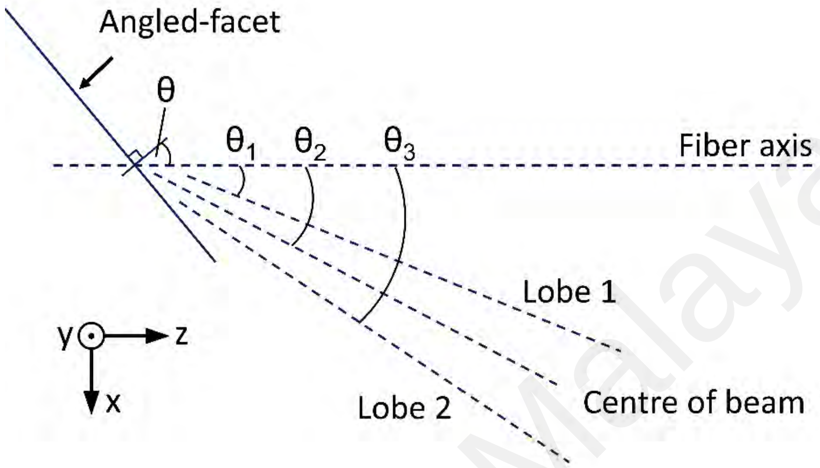

Figure 4.7: Determination of the refracted angle of the simulated AFTMF output beam with two-lobe pattern.

For the case of LP_{01} output beam, the point with highest intensity corresponds to the centre of the beam. The relationship between the refracted angle of LP_{01} output beam and AFTMF facet angle is shown by diamond shape markers in Figure 4.8. On the other hand, the refracted angles for Lobe 1, Lobe 2 and centre of the beam were determined for the case of LP_{11} output beam. The result is summarised in Figure 4.8.

From the inset of Figure 4.8, it can be seen that the refracted angle of Lobe 2 increases near to 85º at facet angle of 42º and becomes a single-lobe beam in the case of 42.5º, 43º and 43.5º. The refracted angle of the single-lobe beams which is marked by the curly brace in the inset is observe to follow the trend line of the Lobe 1 refracted angle. This suggests that Lobe 1 and Lobe 2 have superimposed to form a single-lobe beam.

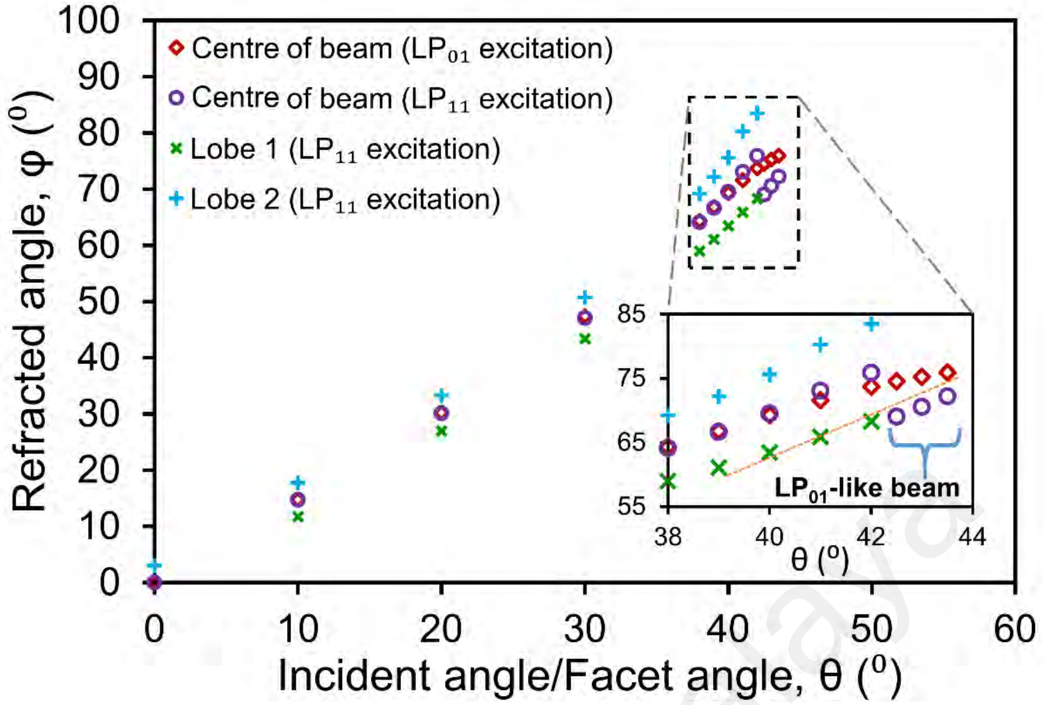

Figure 4.8: Relationship between the refracted angle and facet angle of AFTMF under LP_{01} and LP_{11} mode excitation.

Following that, an AFTMF with facet angle of 43º was fabricated to experimentally verify the simulation results. Due to Fresnel reflection, the output beam intensity decreases when the facet angle increases from 42.5° to 43.5° as observed in the simulation results. Meanwhile 43.6° is the critical angle where the output beam power will reduce to zero. Ideally, facet angle of 42.5° is the best option to achieve higher output beam intensity while maintaining the single-lobe output beam. However, due to the narrow angle range, the AFTMF is fabricated at facet angle of 43°. After the fabrication, the AFTMF was used to perform $LP_{11} \rightarrow LP_{01}$ down-conversion and the performance of the mode conversion and excitation system was examined. The fabrication of the AFTMF will be discussed in the following section.

4.2 Methodology

4.2.1 Fabrication of AFTMF

An AFTMF was fabricated by polishing one of the end facet of a TMF using a polishing machine (Ultrapol) as shown in Figure 4.9. To achieve the desired facet angle, θ, the TMF was attached on the fiber holder with the fiber axis oriented at an angle of ($90^{o} - \theta$) relative to a horizontal plane parallel to the abrasive film as illustrated in Figure 4.10. The polishing process started by employing rough abrasive film followed by finer films in order to obtain an optically flat angled-facet. During the polishing process, the abrasive film was placed on the rotating stage of the polishing machine. The vertical position of the fiber holder was lowered until the TMF tip touched the abrasive film. The TMF tip was grinded by the rotating film when they were in contact. The position of the fiber holder should not be too low so that the TMF was not bent during the polishing process. While keeping the TMF straight, the fiber holder was gradually lowered during the process until an angled-facet was formed on the TMF. Water was applied on the film through a nozzle to remove the debris during the polishing process.

The rotation speed of the abrasive film needs to be controlled within a reasonable rate to avoid vibration of TMF due to high speed rotation of the abrasive film. Meanwhile, high water flow rate should also be avoided because accumulation of water on the rotating film might disturb the TMF orientation and position and subsequently deteriorate the polishing quality. The water also plays the role to cool down the TMF surface being polished.

After the polishing process, the angled-facet was examined under optical microscope and the facet angle was determined from the optical micrograph. The micrographs of the end facet before and after polishing process are depicted in Figure 4.11. The fabrication process was repeated a few times to obtain the AFTMF with the desired facet angle.

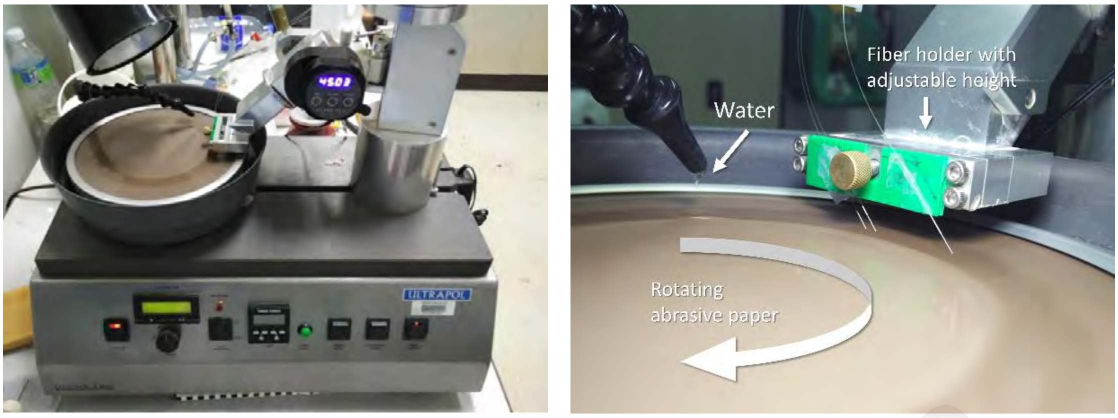

Figure 4.9: The fiber polishing machine and the TMF attached on the fiber holder.

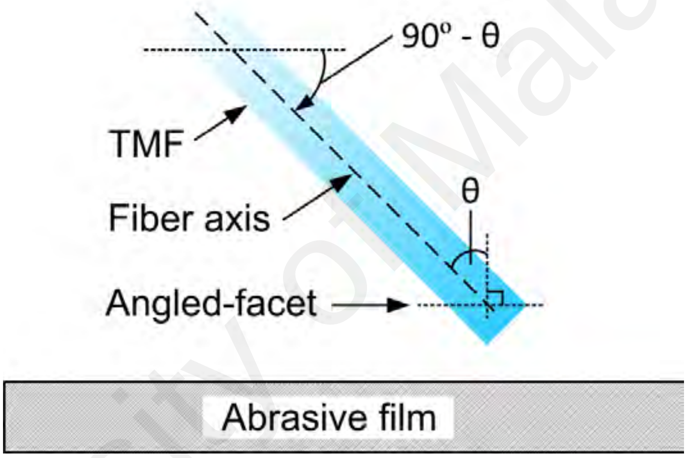

Figure 4.10: Schematic diagram of the TMF orientation on the abrasive film to obtain the angled-facet through polishing process.

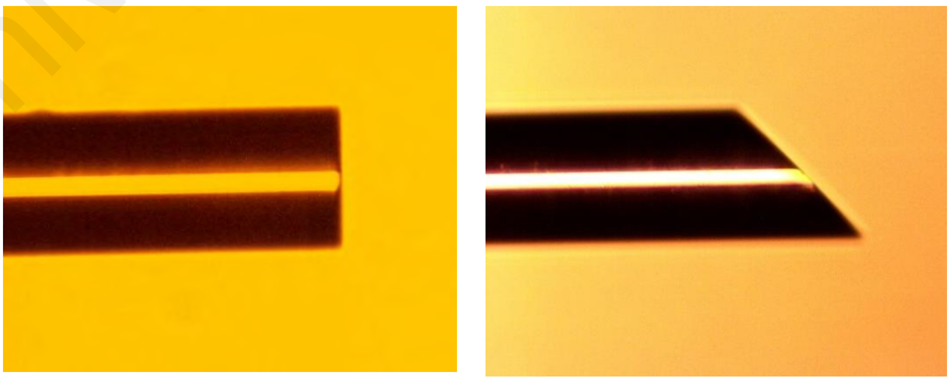

(a) (b)

Figure 4.11: Optical micrograph of the TMF (a) before and (b) after the polishing process.

4.2.2 Selective Mode Conversion and Excitation by AFTMF

To verify whether the AFTMF can convert the LP_{11} mode in the fiber into a single-lobe beam at its output, LP_{11} mode was first selectively excited in the AFTMF by using BPP in the experiment setup as illustrated in Figure 4.12. A tunable laser source (TLS) was used to provide laser in the wavelength of 1530 – 1580 nm. Laser from the TLS was guided by SMF towards a polarisation controller (PC) which was followed by an objective lens. The PC was used to adjust the polarisation of the LP_{01} mode in the SMF while the objective lens collimated the beam from the SMF. The collimated beam was transmitted through the BPP to perform $LP_{01} \rightarrow LP_{11}$ mode conversion before it passed through a polarising beam splitter (PBS). The PBS was used in conjunction with the PC to excite either x- or y-polarised LP_{11} mode in the AFTMF. After the PBS, the converted beam was coupled into the AFTMF through the flat end of the fiber by the second objective lens to excite LP_{11} mode in the AFTMF. The output beam of the AFTMF was characterised by a mode profiler and a power meter.

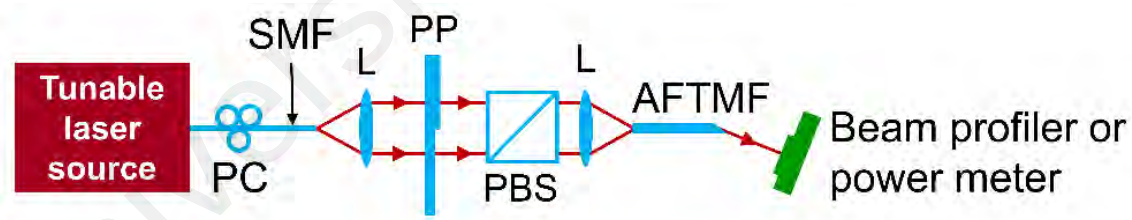

Figure 4.12: Schematic of the experimental setup to excite LP_{11} mode in the AFTMF.

In the characterization of output beam by mode profiler, the mode profile of the single-lobe output beam was first recorded at different z positions to determine the propagation direction and refraction angle of the output beam. The profiler was attached onto a linear stage and it was aligned such that the normal axis of the profiler was parallel to the AFTMF axis and z-axis as depicted in Figure 4.13. Then, the profiler was moved along the z-axis by using the linear stage and the mode profile at different z positions was recorded. The mode profile recorded at different z positions was analysed to determine the peak position of the beams obtained at different z positions.

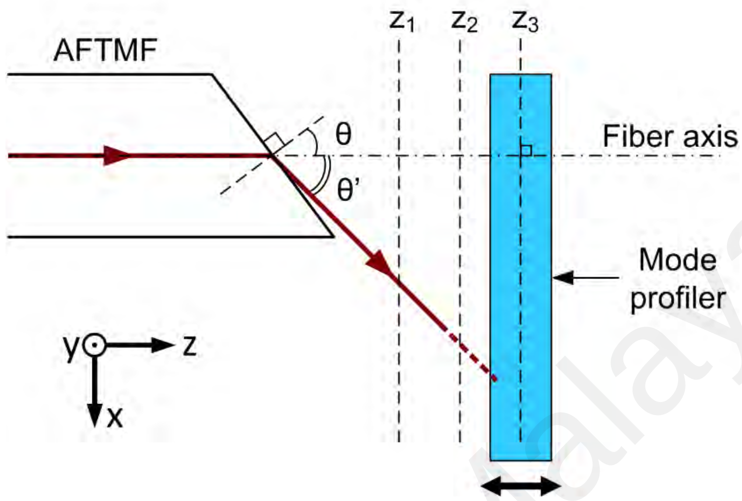

Figure 4.13: Mode profiler with its normal axis coaxial with the AFTMF axis.

Deviation in the angular orientation of the angled-facet will cause the output beam to propagate in upward or downward direction, away from the x-z plane in experiment (Figure 4.14). Therefore, the angled-facet end of the AFTMF was clamped on a fiber rotator to adjust the orientation of the angled-facet. The orientation was tuned until the peak of the beams recorded at different z positions have the same y-coordinate. Then, a straight line that connected the peak at different z positions was obtained. From the linear equation corresponding to the straight line, the slope of the line was determined. Then, the angle between the propagation direction of the beam and the fiber axis, θ', was deduced from the slope. The above procedure is similar to that illustrated in Figure 4.6.

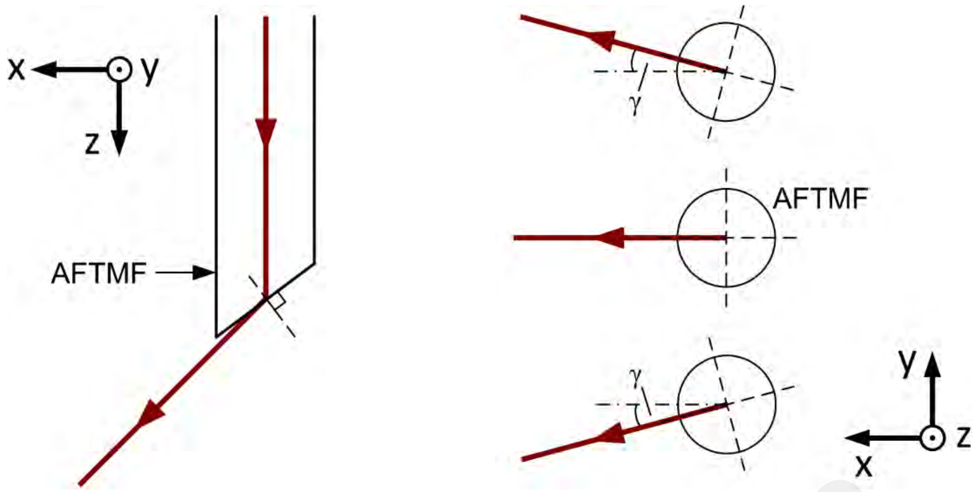

(a) (b)

Figure 4.14: (a) Top and (b) end view of AFTMF and the propagation path of its output beam.

Based on the θ' deduced from the above procedure, the orientation of the mode profiler was adjusted such that its normal axis was coaxial with the propagation axis of the refracted beam (Figure 4.15). To achieve this, the mode profiler was rotated to an angle θ' relative to the x-axis in clockwise direction. Then, the output mode profile of the AFTMF under LP_{11} excitation was recorded with the angled-facet positioned at ~5 mm away from the sensor of the profiler. Following that, the profiler was replaced by the power meter at the same position and orientation to measure the power of the output beam.

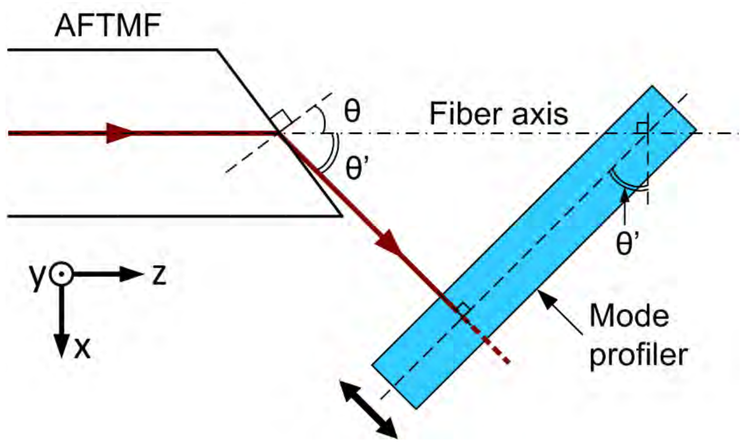

Figure 4.15: Mode profiler with its normal axis coaxial with the AFTMF output beam propagation axis.

Next, the single-lobe AFTMF output beam was coupled into a target FMF with flat input and output facets (Figure 4.16). The input end of the target FMF was clamped on a 5-axis stage to align its position in relative to the AFTMF output beam direction. The yaw adjustment of the stage allowed the tuning of the angle between the target FMF axis and the AFTMF fiber axis. The output mode profile and power of the target FMF were measured by using the mode profiler and power meter during the alignment. The alignment was made in such a way that LP_{01} mode with the optimum output power was observed at the target FMF output. Then, the mode profile and power were recorded. After that, the recording and measurement at the target FMF output were repeated for TLS operating wavelength ranged from 1530 nm to 1580 nm at an interval of 10 nm.

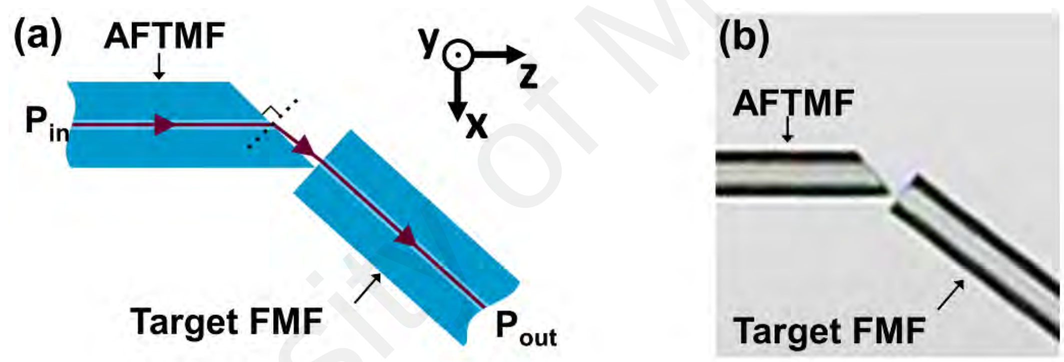

Figure 4.16: (a) Graphical illustration and (b) optical micrograph of the coupling between the AFTMF and the target FMF.

Following that, the target FMF and AFTMF were removed from the system. The AFTMF was removed by cleaving the fiber 20 cm away from the angled-facet. The remaining flat facet TMF with a length of ~80 cm was used as a reference TMF. By cleaving the AFTMF at 20 cm from the angled facet, the angled-facet can be re-used where the reserved length allows splicing of the angled-facet with other TMF. The profile and power of the reference TMF output beam were recorded and measured when the TLS operating wavelength was changed from 1530 nm to 1580 nm at an interval of 10 nm. Finally, the insertion and coupling loss of the AFTMF mode conversion and excitation setup were calculated based on the power readings at the output of the reference TMF, AFTMF and target FMF.

4.2.3 Modal Purity Analysis by using Numerical Method-based Modal Decomposition Technique

The recorded mode profiles at the target FMF output were analysed by using a numerical method-based modal decomposition technique to determine the modal purity of the output beam. The technique used in this work is based on that reported by Huang et al. (L. Huang et al., 2015) and it is discussed below.

An arbitrary propagating field in an FMF can be considered as the superposition of eigenmodes supported by the FMF. In mathematical form:

$$E(r, \phi) = \sum_{n=1}^{N} \rho_n e^{i\theta_n} \psi_n(r, \phi) \tag{4.3}$$

where $E(r, \phi)$ is the arbitrary propagating field, ρ_n and θ_n are the modal amplitude and phase of the n-th eigenmode respectively, and $\psi_n(r, \phi)$ is the field of the n-th eigenmode. The intensity profile corresponding to the arbitrary field is given by: $I(r, \phi) = |E(r, \phi)|^2$. Meanwhile, $|\rho_n|^2$ is the modal weight of the n-th eigenmode and $\sum_{n=1}^{N} |\rho_n|^2 = 1$ for a normalised arbitrary field.

The modal decomposition algorithm is aimed to obtain a set of ρ_n and θ_n that will lead to a reconstructed mode profile with minimum difference compared to the measured mode profile. The difference between the reconstructed and measured profile is evaluated based on the following merit function:

$$J = \left| \frac{\iint \Delta I_{re}(r, \phi)\, \Delta I_{me}(r, \phi)\, r\, dr\, d\phi}{\sqrt{\iint \Delta I_{re}^2(r, \phi)\, r\, dr\, d\phi \iint \Delta I_{me}^2(r, \phi)\, r\, dr\, d\phi}} \right| \tag{4.4}$$

where $\Delta I_j = I_j(r, \phi) - \bar{I}_j$ with j = re, me, I_{re} and I_{me} are reconstructed and measured intensity respectively, and $\bar{I}_j$ is the mean value of the reconstructed and measured intensity distribution.

The flow chart of the modal analysis is depicted in Figure 4.17. Firstly, the image of the measured mode profile was read and the intensity at each pixel was recorded. Then, statistically independent random positive and negative perturbation values for the modal amplitude and phase ($\delta\rho_{i\pm}$ and $\delta\theta_{i\pm}$) were generated by the algorithm. By applying the perturbation, new modal amplitude and phase were generated: $\rho_{i\pm} = \rho_i \pm \delta\rho_i$ and $\theta_{i\pm} = \theta_i \pm \delta\theta_i$ where ρ_i and θ_i are the pre-set initial value of modal amplitude and phase. The new $\rho_{i\pm}$ and $\theta_{i\pm}$ were applied in equation (4.3) to reconstruct two temporary intensity profile, $I_{re\pm}$. Following that, the merit function, $J_\pm$ of the reconstructed and measured profile was determined and δJ was deduced. Finally, the value of modal amplitude and phase were updated ($\rho_i = \rho_i + \beta_1\ \delta J\ \delta\rho_i$ and $\theta_i = \theta_i + \beta_2\ \delta J\ \delta\theta_i$) where β_1 and β_2 are the update gain. The process was repeated until the reconstructed mode profile achieved merit function above 95%.

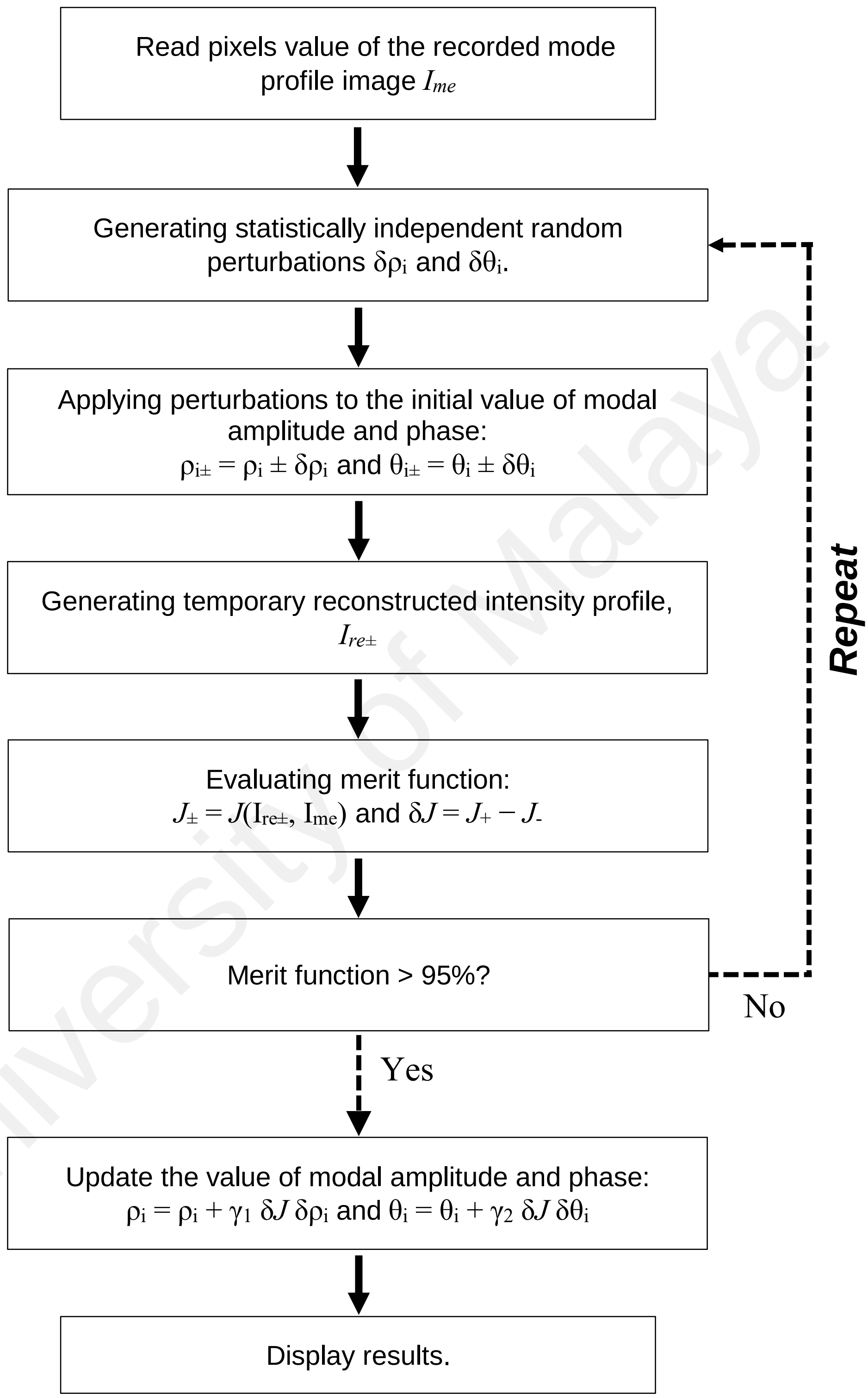

Figure 4.17: Flow chart of the modal analysis algorithm.

4.3 Results and Discussions

4.3.1 Characterisation of Mode Profile and Power

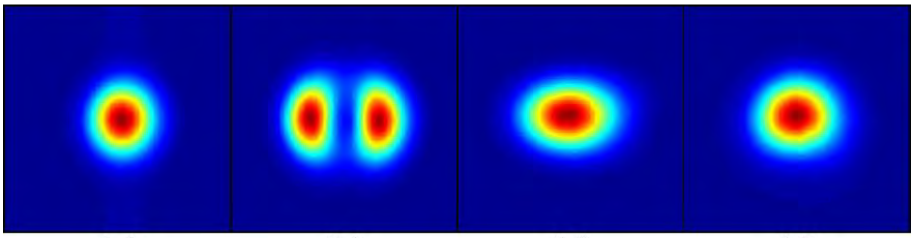

Figure 4.18: Output mode profiles of (a) reference TMF under LP_{01} excitation, (b) reference TMF under LP_{11} excitation, (c) AFTMF under LP_{11} excitation, and (d) target FMF under excitation of the converted beam shows in (c).

Mode profiles recorded at the output of reference TMF under LP_{01} and LP_{11} excitation are shown in Figure 4.18(a) and (b). Meanwhile, Figure 4.18(c) shows the mode profiles at the AFTMF output when the AFTMF was under LP_{11} excitation. The profile shows that the two-lobe LP_{11} mode can be converted into a single-lobe beam as simulated by OptiFDTD at facet angle of 43°. The elliptical shape of the single-lobe beam in Figure 4.18(c) is due to the larger divergence along the horizontal axis of the angled facet as compared to the vertical axis. Figure 4.18(d) shows the mode profile at the target FMF output when the FMF was excited by the single-lobe beam using the coupling configuration shown in Figure 4.16.

Next, the vertical and horizontal one-dimensional (1-D) line intensity profile that crossed the peak of the beam shown in Figure 4.18(a) and (d) were obtained. They were compared with the theoretical Gaussian profile as shown in Figure 4.19. The Gaussian profile is based on the following equation (Saleh & Teich, 1991):

$$I(r,z) = I_0 \left[\frac{W_0}{W(z)}\right]^2 \exp\left[-\frac{2r^2}{W^2(z)}\right] \qquad (4.5)$$

where I(r, z) is the intensity of the Gaussian beam as a function of axial (z) and radial (r) position, I_0 is the peak intensity for the Gaussian beam at its beam waist where r = 0 and z = 0, $W_0 = (\lambda z_0/\pi)^{0.5}$ is the beam waist radius, λ is the wavelength, z_0 is the Rayleigh length, $W(z) = W_0[1 + (z/z_0)^2]^{0.5}$ is the beam radius at axial distance of z. It can be seen that the profile of the target FMF output mode is in good agreement with the theoretical Gaussian profile.

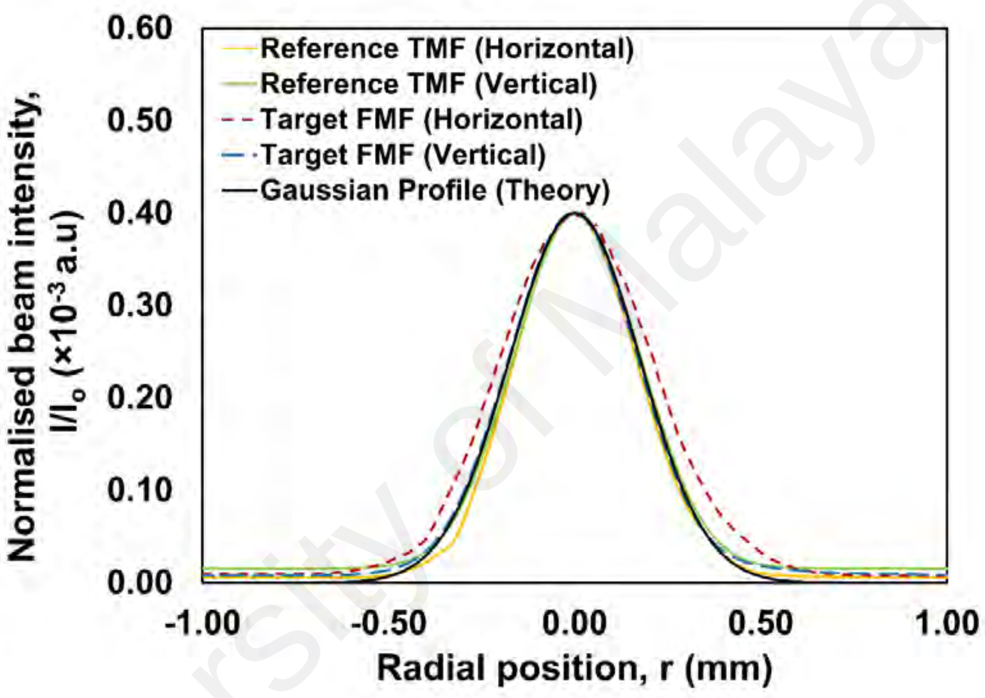

Figure 4.19: 1-D intensity profiles of the reference TMF and target FMF output beam.

Following that, the modal purity of the target FMF output beam was analysed by using the modal decomposition algorithm where three modes (LP_{01}, LP_{11odd} and LP_{11even}) were considered in the analysis. It is estimated that the output beam is composed of 99.2% LP_{01} mode, 0.5% LP_{11a} mode and 0.3% LP_{11b} mode as depicted in Figure 4.20. This shows that the single-lobe beam from the AFTMF can excite a high modal purity LP_{01} mode in the target FMF.

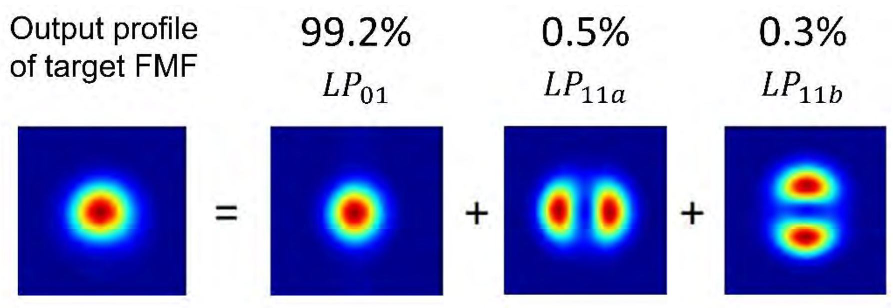

Figure 4.20: Modal purity of the target FMF output beam.

When the reference TMF was under the excitation of x-polarised LP_{11} mode, the output beam power was measured to be ~4.52 dBm. It is assumed to be equivalent to the input power (P_{in}) to the angled-facet of the AFTMF. As the AFTMF output beam power was measured to be 2.77 dBm, the insertion loss of the angled-facet is therefore 1.75 dB. When the 2.77 dBm AFTMF output beam was coupled into the target FMF, the power of the LP_{01} mode measured at the target FMF output is -1.23 dBm. This indicates a coupling loss of 4.00 dB and total insertion loss of 5.75 dB.

Table 4.1: Output beam power measurement and the calculated power losses.

Polarisation of LP_{11} excitation in AFTMF	Output beam power (dBm)			Insertion loss of angled-facet (dB)	Coupling loss (dB)	Total insertion loss (dB)
	Reference TMF	AFTMF	Target FMF			
x	4.52	2.77	-1.23	1.75	4.00	5.75
y	4.52	0.49	-3.50	4.03	4.00	8.02

For reference TMF under excitation of y-polarised LP_{11} mode, the output beam power of the reference TMF was same as that under excitation of x-polarised LP_{11} mode, which is 4.52 dBm. However, under y-polarised LP_{11} excitation, the output power of the AFTMF is only 0.49 dBm. Therefore, the insertion loss of angled-facet is higher when y-polarised LP_{11} mode is used, which is 4.03 dB. Coupling of the 0.49 dBm single-lobe beam into the target FMF leads to LP_{01} mode at the target FMF output with power of -3.50 dBm. The coupling loss is therefore 4.00 dB while the total insertion loss is 8.02 dB. The above power measurements were performed at an operating wavelength of 1550 nm. The total insertion loss varied in the range of ±0.5 dB when the wavelength changed from 1530 nm to 1580 nm at a step size of 5 nm with the input power of the TLS remained constant throughout the wavelength range.

Three major factors that might contribute to the total insertion loss are the light scattering at the fiber end facet due to surface roughness, Fresnel reflections and mode field mismatch (MFM). Scattering loss is generally small and negligible since the end facets of the AFTMF and target FMF have been properly polished and cleaved. Meanwhile, Fresnel reflection is responsible for the insertion loss at the angled-facet and the target FMF end facets when the light propagates across the air-glass or glass-air interfaces. When the incident angle is 10º or less, $\lesssim$ 3.5% of the incident light power will be reflected for both x- and y-polarisation beams. This is the case at the input and output facets of the target FMF. At incident angle of 43º, the reflectances for x- and y-polarisation beams are greater, which are ~31.5% and ~58.5% respectively. From the power measurement, the power loss at the angled-facet is 33.2% (1.75 dB) and 60.4% (4.03 dB) of P_{in} for x- and y-polarisation respectively, which are in agreement with the calculations. Anti-reflection coating can be applied at the angled-facet to reduce the insertion loss at the angled-facet. The use of different anti-reflection coatings and their performance will be discussed in next section. On the other hand, the mode field mismatch between the AFTMF output beam and the LP_{01} mode of the target FMF is a main constituent of the coupling loss. This is because the size of the AFTMF output beam becomes larger than the mode field of LP_{01} mode in the target FMF due to beam divergence. The mode field mismatch can be reduced by positioning the target FMF close to the AFTMF output so that the beam is coupled into the FMF before it diverges into a large beam. Besides, the acute tip of the AFTMF can be removed to allow the target FMF to be positioned closer to the AFTMF output as is illustrated in Figure 4.21.

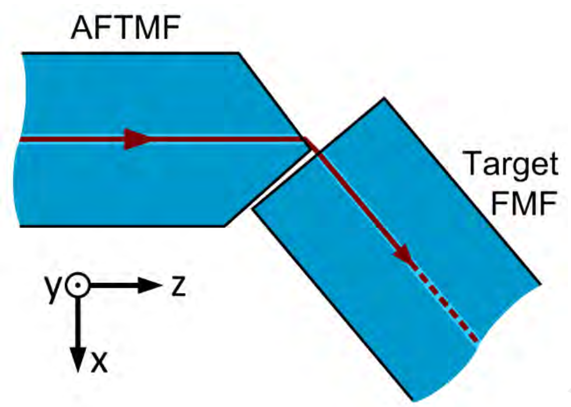

Figure 4.21: Illustration of the coupling between the AFTMF (without its acute tip) and the target FMF.

4.3.2 Anti-reflection Coating

Anti-reflection (AR) coating can be applied on the angled-facet to address the high insertion loss due to Fresnel reflection at the angled-facet. For AR coating on the angled-facet, light from the fiber core will hit the coating at an oblique angle. Catalan has provided a concise discussion on the calculation method for multilayer AR coating system which can be applied for any incident angle and wavelength (Catalán, 1962). Calculation in this work is based on the method described by Catalan.

Generally, the reflectance, R from a multilayer AR coating can be expressed as:

$$R = \left| \frac{u_p E_p - H_p}{u_p E_p + H_p} \right|^2 \tag{4.6}$$

where u_j is the generalised RI for the j-th medium where $j \in \{0,1,2,\cdots,p\}$ and φ_j is the incident angle at the boundary of the j-th and (j+1)-th medium.

The generalised RI is defined as follows depending on the polarisation of the incident light:

$$u_{j,\parallel} = n_j / \cos \varphi_j \tag{4.7}$$

$$u_{j,\perp} = n_j \cos \varphi_j \tag{4.8}$$

where $u_{j,\parallel}$ and $u_{j,\perp}$ are the generalised RI for incident light with polarisation parallel and perpendicular to the plane of incidence respectively and n_j is the RI of the j-th medium by assuming that the medium is lossless.

The electric and magnetic fields, E and H in different media can be obtained by the following relationship:

$$\begin{pmatrix} E_{k+1} \\ H_{k+1} \end{pmatrix} = \begin{pmatrix} \cos g_k & (i \sin g_k)/u_k \\ i u_k \sin g_k & \cos g_k \end{pmatrix} \begin{pmatrix} E_k \\ H_k \end{pmatrix} \tag{4.9}$$

where u_k is the generalised RI for the k-th medium, $g_k = \left(\frac{2\pi}{\lambda}\right) n_k h_k \cos \varphi_k$, h_k is the geometrical thickness of the corresponding layer with $k \in \{1,2,\cdots,(p-1)\}$, $E_1 = E_0$ and $H_1 = u_0 E_0$.

For the case of single layer AR coating, there are three media. Therefore, $j \in \{0,1,2\}$ and $p = 2$. Then, from equations (4.6) and (4.9):

$$R = \left| \frac{u_2 E_2 - H_2}{u_2 E_2 + H_2} \right|^2 \tag{4.10}$$

$$\begin{pmatrix} E_2 \\ H_2 \end{pmatrix} = \begin{pmatrix} \cos g_1 & (i \sin g_1)/u_1 \\ i u_1 \sin g_1 & \cos g_1 \end{pmatrix} \begin{pmatrix} E_1 \\ H_1 \end{pmatrix} \tag{4.11}$$

Applying $E_1 = E_0$ and $H_1 = u_0 E_0$ into equation (4.11) and substitute E_2 and H_2 into equation (4.10), the following relationship can be obtained:

$$R = \frac{(u_2 - u_0)^2 \, cos^2 g_1 + (\frac{u_0 u_2}{u_1} - u_1)^2 \, sin^2 g_1}{(u_2 + u_0)^2 \, cos^2 g_1 + (\frac{u_0 u_2}{u_1} + u_1)^2 \, sin^2 g_1} \tag{4.12}$$

On the other hand, in the case of bilayer AR coating, four media are involved where $j \in \{0,1,2,3\}$ and $p = 3$. Then:

$$R = \left|\frac{u_3 E_3 - H_3}{u_3 E_3 + H_3}\right|^2 \tag{4.13}$$

Using similar method for the case of single layer AR coating, it can be shown that:

$$\begin{aligned} u_3 E_3 \pm H_3 = &\left\{(u_3 \pm u_0) \cos g_1 \cos g_2 \mp \left(\frac{u_2 u_0}{u_1} \pm \frac{u_1 u_3}{u_2}\right) \sin g_1 \sin g_2\right\} E_0 \\ &+ i\left\{\left(\frac{u_0 u_3}{u_1} \pm u_1\right) \sin g_1 \cos g_2 \right. \\ &\left. + \left(\frac{u_0 u_3}{u_2} \pm u_2\right) \sin g_1 \cos g_2\right\} E_0 \end{aligned} \tag{4.14}$$

The term E_0 will be cancelled out when equation (4.14) is substituted into equation (4.13). Therefore, it is not necessary to determine its value. When bilayer AR coating are applied on the AFTMF, medium 0, 1, 2 and 3 are corresponding to the air, first layer of AR coating, second layer of AR coating and AFTMF respectively. Figure 4.22 illustrates the system and the respective parameters for each medium.

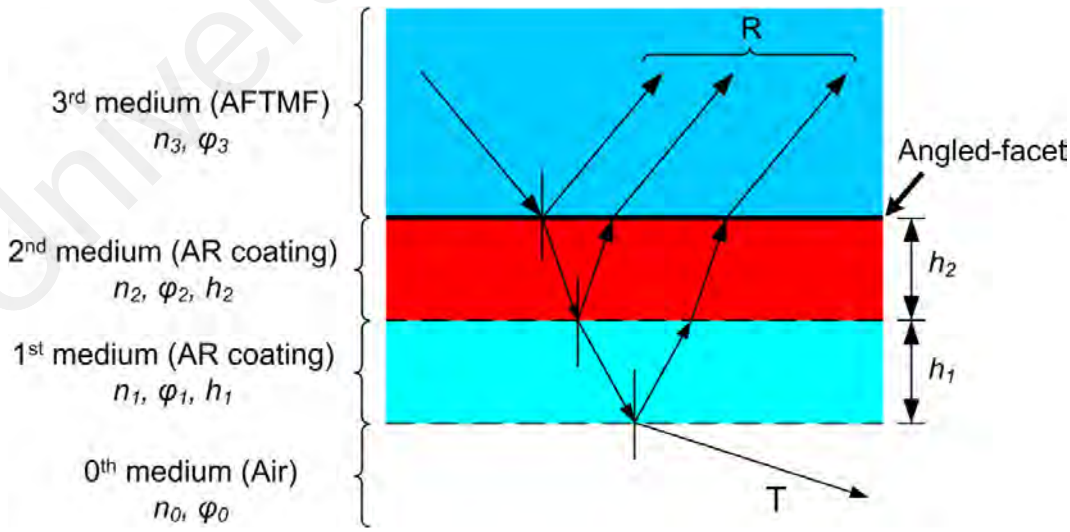

Figure 4.22: Illustration of a bilayer AR coating on the angled-facet and the corresponding parameters.

Based on the mathematical treatment presented above, several AR configurations to reduce the reflection at the angled-facet were considered and the performance for three of the coatings is summarised in Table 4.2. The transmittance was deduced from the calculated reflectance. In the table, the thickness for each layer of the AR coatings, *h* has been calculated based on operating wavelength of 1550 nm. The three coatings are single layer sodium fluoride (NaF), bilayer NaF/magnesium oxide (MgO), and bilayer NaF/zinc selenide (ZnSe). The RI for NaF, MgO and ZnSe are 1.32, 1.71 and 2.46 respectively. The coatings are assumed to be lossless. In the case of bilayer coating, the high index layer (MgO or ZnSe) is first deposited on the angled-facet and followed by the low index coating (NaF). This is illustrated in Figure 4.23 below.

Table 4.2: Performance of different AR coatings on the angled-facet.

Materials	**RI**	***h* (nm)**	**Transmittance (%)**		
			x-pol.	**y-pol.**	**Average**
Without coating (Experiment)	-	-	68.5 (66.8)	41.5 (39.6)	55.0 (53.2)
NaF	1.32	446	68.9	55.0	62.0
NaF/MgO	1.32/1.71	391/431	66.4	66.4	66.4
NaF/ZnSe	1.32/2.46	427/192	46.8	99.5	73.2

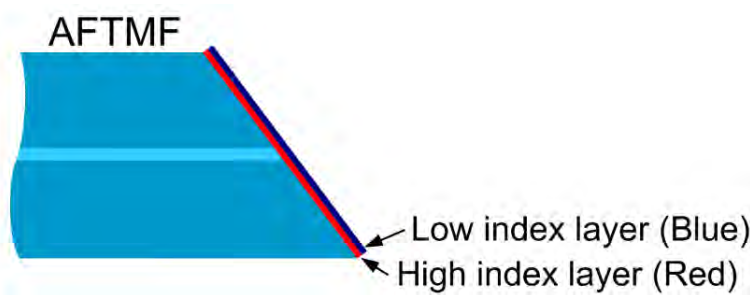

Figure 4.23: Configuration of bilayer AR coating on the angled-facet.

When no AR coating is applied, the theoretical transmittances at the angled-facet (silica-air interface) for x- and y-polarised lights are 68.5% and 41.5% respectively. From the experiment, we found that the transmittances for x- and y-polarised lights are 66.8% and 39.6% respectively, which are in agreement with the theoretical transmittances. The transmittances are observed to increase to 68.9% and 55.0% for x- and y-polarised light respectively, when a single layer NaF AR coating with thickness of 446 nm is applied on the angled-facet.

For NaF/MgO bilayer AR coating with thicknesses shown in Table 4.2, the transmittance at the angled-facet is the same for both x- and y-polarised light, which indicates that the transmittance is polarisation independent. By applying the NaF/MgO bilayer AR coating on the angled-facet, the average transmittance improved by about 11.4% when compared to the case without AR coating. Although the transmittance is slightly reduced for the case of x-polarised light when compared to that without coating, the advantage of polarisation independent transmittance might prevail over the small decrease. This is because the mode conversion efficiency will be independent of the input light polarisation.

On the other hand, NaF/ZnSe bilayer AR coating with thicknesses shown in Table 4.2 can further increase the average transmittance to 73.2%. However, the transmittance of this bilayer coating is strongly polarisation dependent. It significantly increases the transmittance of y-polarised light to 99.5% at the expense of lower transmittance for x-polarised light. The NaF/ZnSe bilayer coating is beneficial if the input light is restricted to y-polarisation only. If the input light is x-polarised, the NaF/ZnSe bilayer coating will reduce the transmittance at the output instead of increasing it.

4.4 Summary

In this chapter, $LP_{11} \rightarrow LP_{01}$ down conversion by an AFTMF has been examined. Firstly, the propagation of the output beam of TMF with different output facet angle has been simulated by the OptiFDTD. The refracted angle of the output beam was determined from the simulated results. It was found that LP_{11} mode in the TMF was turned into a single-lobe output beam when the TMF output facet angle was in the range of 42.5° - 43.5°. Based on the analysis, an AFTMF with facet angle of 43^0 was fabricated by fiber polishing machining by using abrasive films with progressive grades to achieve optical finishing. The facet angle of the AFTMF was determined through the optical micrograph.

Next, LP_{11} mode was excited in the fabricated AFTMF by using BPP. Then, the mode profile and power of the AFTMF output mode were recorded and measured. A single-lobe beam has been observed at the output of the AFTMF. Following that, the single-lobe beam was coupled into the core of a target FMF and the mode profile and power at the target FMF output were recorded and measured. The 1-D profile of the output beam was compared with the theoretical Gaussian profile and it was found that they are in good agreement. Besides, the modal purity was analysed by using numerical method-based modal decomposition technique. The analysis suggested that the recorded mode profile at the target FMF output is composed of 99.2% of LP_{01} mode, 0.5% LP_{11a} mode and 0.3% of LP_{11b} mode.

Through the power measurement, the AFTMF insertion loss was found to be 1.75 dB and 4.03 dB for LP_{11} mode excitation in the AFTMF with x- and y-polarisation respectively. On the other hand, the AFTMF-target FMF coupling loss was the same at 4.00 dB for both polarisation. This leads to total insertion loss of 5.75 dB and 8.02 dB for the case of x- and y-polarisation respectively. The total insertion loss varied in the range of ±0.5 dB when the operating wavelength was changed in the range of 1530 – 1580 nm.

Scattering loss, Fresnel reflection and mode field mismatch were suggested to be the major factors that contributed to the total insertion loss. The use of single-layer (NaF) and bilayer (NaF/MgO and NaF/ZnSe) AR coating was evaluated to reduce the insertion loss due to Fresnel reflection at the angled-fact of AFTMF. AR coating can potentially reduce the total insertion loss from 8.02 dB to 4.01 dB for the case of y-polarisation.

CHAPTER 5: LP MODES SPLITTING BASED ON POLARISATION MANIPULATION IN FMF

Three-paddle polarisation controller (PC) has been extensively used for controlling and manipulating the polarisation of beam in SMF (LP_{01} mode) due to its simple operation and low cost. However, the related literature on the use of three-paddle PC to manipulate polarisation of both fundamental and higher-order modes in few-mode fiber (FMF) is scanty. Hong et al. demonstrated the rotation of LP_{11} mode profile and polarisation over a range of 360^0 by using an FMF three-paddle PC (Hong et al., 2016). On the other hand, Cui et al. manipulated the polarisation of LP_{01}, LP_{11a} and LP_{11b} modes in an elliptical core FMF by a three-paddle PC (Cui et al., 2017). In this chapter, we demonstrate the use of a three-paddle two-mode fiber PC (TMPC) for simultaneous manipulation of LP_{01} and LP_{11} modes in a two-mode fiber (TMF) into perpendicular polarisation states. Based on this finding, we proposed a method for splitting of LP modes in a TMF by using a configuration consisted of a TMPC and a polarising beam splitter (PBS). The modal purity and power of the LP modes split at the PBS outputs were determined. Besides, the temporal stability of the split modes in terms of mode position and modal purity were analysed.

5.1 Theoretical Background

Three-paddle PC is a simple and convenient device to manipulate the polarisation of light in a fiber through the bend- and twist-induced birefringence. It is made by winding an optical fiber on the paddles of the PC where the fiber is bent into circular loops with a specific diameter on the paddles. Due to bending, the circular geometrical symmetry of the fiber is deformed and the stress field across the cross-section of the bent-fiber becomes asymmetry. This leads to the formation of anisotropic refractive index (RI) distribution across the fiber cross-section and birefringence in the bent-fiber. For a bent fiber with a bending radius of R, the changes in the RI in x- and y-directions are given by (Lefevre, 1980; Ulrich et al., 1980):

$$\Delta n_x = n_{eff,x} - n = \frac{n^3}{4}(p_{11} - 2\nu p_{12})\left(\frac{r}{R}\right)^2 \tag{5.1}$$

$$\Delta n_y = n_{eff,y} - n = \frac{n^3}{4}(p_{12} - \nu p_{12} - \nu p_{11})\left(\frac{r}{R}\right)^2 \tag{5.2}$$

where $n_{eff,x}$ and $n_{eff,y}$ are the effective indices in *x*- and *y*-directions respectively, *n* is the RI of the fiber core, *r* is the fiber radius, $\nu = 0.17$ is the Poisson's ratio, p_{11} and p_e are the strain-optical coefficient where $p_{11} = 0.121$, $p_{12} = 0.270$. The weak curvature limit should be satisfied where $(r/R) \ll 1$.

The bend-induced birefringence is defined as:

$$\begin{aligned}(\delta n)_b &= n_{eff,x} - n_{eff,y} \\ &= \frac{n^3}{4}(p_{11} - p_{12})(1+\nu)\left(\frac{r}{R}\right)^2\end{aligned} \tag{5.3}$$

The bend-induced birefringence per unit length, β_b, can be determined as follows:

$$\begin{aligned}\beta_b &= (\delta n)_b\, k \\ &= \frac{n^3}{4}(p_{11} - p_{12})(1+\nu)\left(\frac{r}{R}\right)^2 k\end{aligned} \tag{5.4}$$

where $k=2\pi/\lambda$ is the free space wavenumber and λ is the free space wavelength.

Equations (5.3) and (5.4) can be applied to weak-guidance silica fiber regardless of the fiber's core diameter and index profile. The birefringence will introduce phase retardance to the light in the fiber and change the polarisation state of the light. The phase retardance introduced by a fiber loop with bending radius of *R* is equivalent to $\beta_b L$ where $L = 2\pi R$ is the circumference of the loop. For *N* number of loops, the total phase retardance becomes $\beta_b(2\pi R)N$. Thus, the phase retardance can be increased by applying additional number of loops or reducing the bending radius.

The steps to rotate the polarisation of a linearly polarised light by using a three-paddle PC is illustrated in Figure 5.1. Generally, the first and third paddle of the PC are used to convert the light between linear and elliptical or circular polarisation states. These two paddles are equivalent to the quarter-wave plates (QWP) which introduces a phase retardance of π/2. When the input light is linearly polarised at 45º relative to the fast (f) and slow (s) axes of the QWP, its polarisation will be transformed into circular polarisation state by the QWP. However, if the linear polarisation state is at other angles relative to the two axes, the light will be transformed into elliptical polarisation state. Meanwhile, the second paddle of the PC acts as a half-wave plate (HWP) which introduces phase retardance of π and it is used to rotate the elliptical or circular polarisation angle. The handedness of the polarisation will also be inversed by the HWP. On the other hand, the fiber in the PC might be twisted when the orientation of the paddles is adjusted. This leads to the twist-induced birefringence which will rotate the polarisation orientation. The twist-induced birefringence is given by (Kumar & Ghatak, 2011):

$$(\delta n)_t = \frac{\lambda}{2\pi} g\tau \tag{5.5}$$

where $g = -(n^2/2)(p_{11} - p_{12}) \approx 0.16$ for a silica fiber and τ is the twist rate in rad/m. It will lead to the rotation of polarisation orientation at a rate of:

$$\alpha = \frac{1}{2} g\tau \tag{5.6}$$

The following equation can be used to determine the number of loop that needs to be wound on the three paddles to formulate the QWP and HWP (Lefevre, 1980):

$$|(\delta n)_b|(2\pi NR) = \frac{\lambda}{m} \tag{5.7}$$

where $(\delta n)_b$ is the bend-induced birefringence, R is the paddle's radius or the loop's bending radius, N is the number of fiber loops on each paddle and m = 2 and 4 for HWP and QWP respectively.

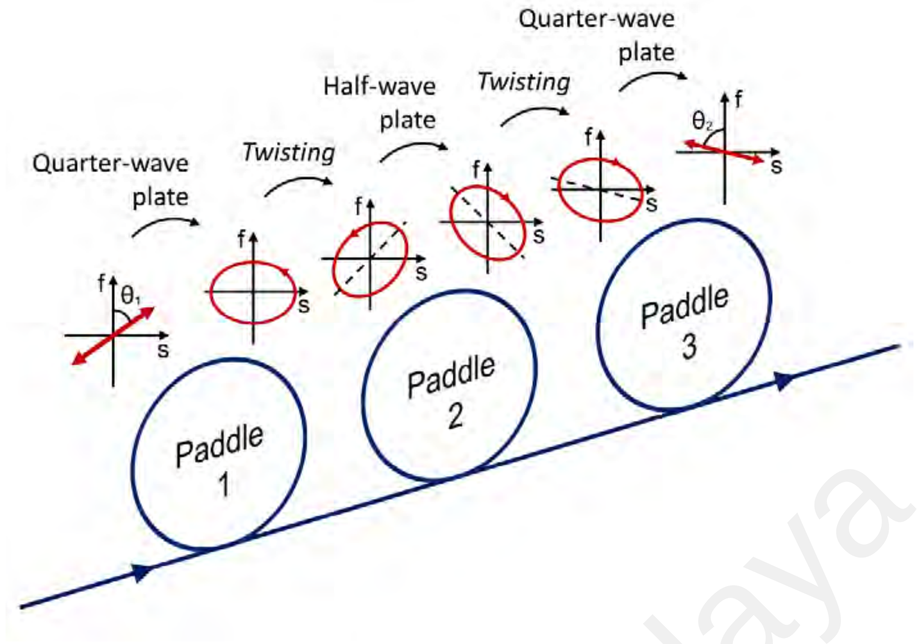

Figure 5.1: Manipulation of a linearly polarised light by a three-paddle polarisation controller.

A SMF can support an exact mode in x- and y-polarisation, namely HE_{11}^{x} and HE_{11}^{y} which are equivalent to LP_{01x} and LP_{01y} modes respectively. The effective index of the modes in the x- and y-polarisation states are $n_{eff,x}$ and $n_{eff,y}$ respectively. For an ideal circular core SMF, $n_{eff,x} = n_{eff,y}$ and the fiber does not exhibit any birefringence. However, due to external perturbations such as bending and twisting, birefringent is induced in the fiber and $n_{eff,x} \neq n_{eff,y}$. The polarisation of the modes in the SMF is manipulated by controlling the degree of bending and twisting in a three-paddle PC as described earlier.

On the other hand, an FMF can support more than one LP mode that has different effective index. When the FMF is used in the three-paddle PC, bending and twisting of the FMF lead to deformation of the mode field profiles and changing the effective index of the modes. From equations (5.1) – (5.4), bend-induced birefringence is related to $n_{eff,x}$ and $n_{eff,y}$ of the corresponding mode. Since different LP modes have different effective index, they will experience different bend-induced birefringence. This causes the LP modes to experience different polarisation evolution when the PC is manipulated.

5.2 Methodology for LP Modes Splitting by TMPC-PBS Setup

In the experiment, a tunable laser source (Santec, ECL-210; TLS) was used to provide monochromatic light with linewidth as low as 1.6 pm in the wavelength range of 1530 – 1610 nm. Laser from the TLS was guided by a SMF towards a TMF. LP_{01} and LP_{11} modes were excited in the TMF via offset-splicing between the SMF and the TMF. Then, the total output power of the TMF was measured by power meter when the TLS operating wavelength was changed from 1530 nm to 1560 nm at a step size of 10 nm. After the power measurement, the TMF was spliced to a TMPC to manipulate the polarisation of the LP modes in the TMF.

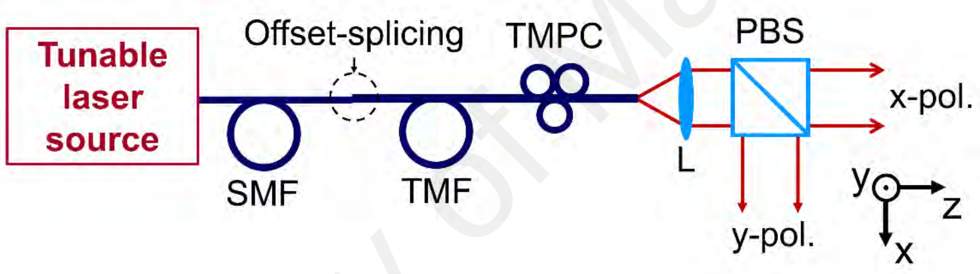

Figure 5.2: Schematic diagram of the experimental setup to split LP modes in a TMF by TMPC-PBS configuration.

The TMPC was made of TMF coiled on a commercially available three-paddle PC frame. This is shown in Figure 5.3. The PC have paddle radius, *R,* of 1.75 cm while the radius of the TMF, *r,* was 62.5 μm. Based on the calculation using equation (5.7), the required numbers of loops for phase retardances of π (HWP) and π/2 (QWP) at $\lambda = 1.55$ μm are 4.15 and 2.08 respectively. The numbers are rounded to 4 and 2 in the experiment. The phase retardances provided by 4 and 2 loops are in the range of 0.96π - 0.98π and 0.48π - 0.49π respectively when the operating wavelength decreased from 1560 nm to 1530 nm. These values are close to the expected phase retardance of π and π/2. Therefore, numbers of loop wound on the three paddles were 2, 4 and 2 respectively to obtain TMPC with paddle configuration of QWP-HWP-QWP.

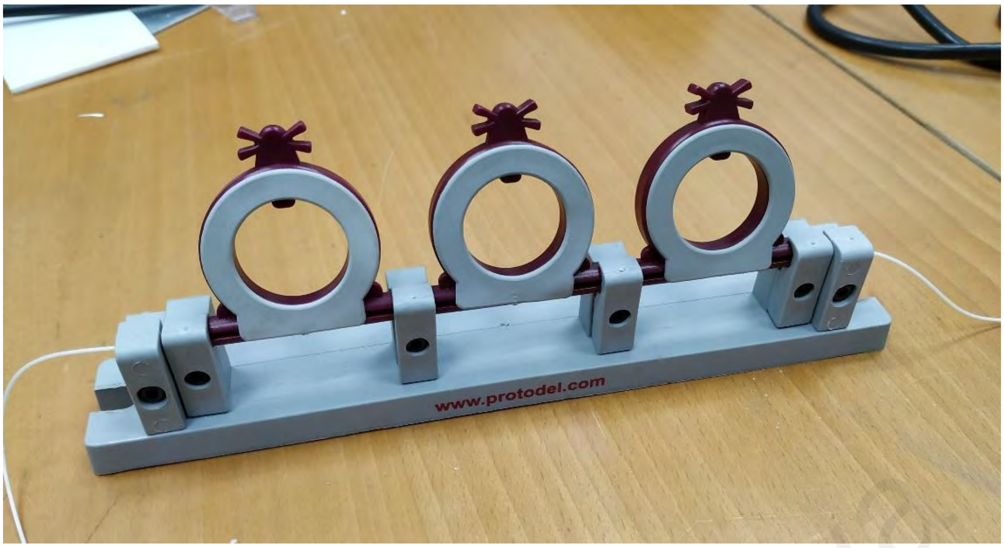

Figure 5.3: Commercial three-paddle polarisation controller.

Following that, an objective lens was used to collimate the output beam of the TMPC before being split by a PBS. At the transmitted and reflected output of the PBS, the output mode profile was recorded by a mode profiler while the mode power was measured by a power meter. With the PBS orientation shown in Figure 5.2, the transmitted output has x-polarisation while the reflected output has y-polarisation.

Then, the paddles of the TMPC were tuned to a configuration where LP_{01x} and LP_{11y} modes were observed at the transmitted and reflected outputs of the PBS respectively by mode profiler. This TMPC output state is denoted as TMPC-1. The mode power at the PBS outputs was measured. After that, the mode profile of LP_{01x} and LP_{11y} at the PBS outputs were recorded by mode profiler for 300 s at an interval of 5 s to determine the stability of the PBS output mode.

Firstly, the recorded mode profiles at different times were analysed by peak-finding algorithm to determine the peak position of the lobes. From the analysis, the standard deviation of the peak position over the recording period, σ_{peak}, was calculated by the following equation:

$$\sigma_{peak} = \sqrt{\frac{\sum_{i=1}^{n}\left[\left(x_i - x_{avg}\right)^2 + \left(y_i - y_{avg}\right)^2\right]}{n-1}} \tag{5.8}$$

where x_i and y_i are the normalised x- and y-coordinates for the peak of the i-th mode profile recorded during the 300 s. They were normalised with respect to the effective mode field radius, ω_{eff}, of the measured mode profile to obtain x_i and y_i. The effective mode field radius was determined by the following equations (Nakamura, Okamoto, Koshikiya, & Manabe, 2016):

$$A_{eff} = \frac{\left|\iint \mathrm{E}^2(\mathrm{x,y})\,\mathrm{dx\,dy}\right|^2}{\iint \mathrm{E}^4(\mathrm{x,y})\,\mathrm{dx\,dy}} \tag{5.9}$$

$$\omega_{\mathrm{eff}} = \sqrt{\frac{3\mathrm{A_{eff}}}{4\pi}} \tag{5.10}$$

where A_{eff} is the effective mode area and E(x,y) is the electric field distribution. Since $|E(x,y)|^2$ is directly proportional to the intensity distribution of the mode profile, the A_{eff} can be calculated from the recorded mode profile.

Meanwhile, x_{avg} and y_{avg} are the average of x_i and y_i respectively and they are given by:

$$\mathrm{x}_{avg} = \frac{\sum_{i=1}^{n} x_i}{n} \tag{5.11}$$

$$\mathrm{y}_{avg} = \frac{\sum_{i=1}^{n} y_i}{n} \tag{5.12}$$

where n is the total number of recorded mode profile over the period of 300 s.

After the mode position analysis, modal purity of the recorded mode profiles over the recording period was analysed by the numerical method-based modal decomposition technique discussed in Chapter 4. Based on the modal content determined from the analysis, the mode extinction ratio, MER, of each LP_ν mode profile is calculated by the following equation:

$$\mathrm{MER} = 10\log_{10}\left(\frac{\mathrm{P_\nu}}{\mathrm{P_\mu}}\right) \tag{5.13}$$

where ν, μ ∈ {01, 11} and ν ≠ μ while P_ν and P_μ are the modal content of LP_ν and LP_μ modes respectively, determined by the modal decomposition technique. After that, the MER corresponding to the individual mode profiles were summed and divided by the total number of mode profile recorded during the 300 s period to obtain the average mode extinction ratio:

$$\mathrm{MER_{avg}} = \frac{\sum_{\mathrm{j}=1}^{\mathrm{n}} \mathrm{MER_j}}{n} \tag{5.14}$$

where MER_i denotes the i-th MER of a recorded mode profile in the 300 s duration and n is the total number of recorded mode profiles. The standard deviation of all n MERs over the 300 s period, σ_{MER}, is calculated using the following equation:

$$\sigma_{MER} = \sqrt{\frac{\sum_{i=1}^{n}\left(MER_i - MER_{avg}\right)^2}{(n-1)}} \tag{5.15}$$

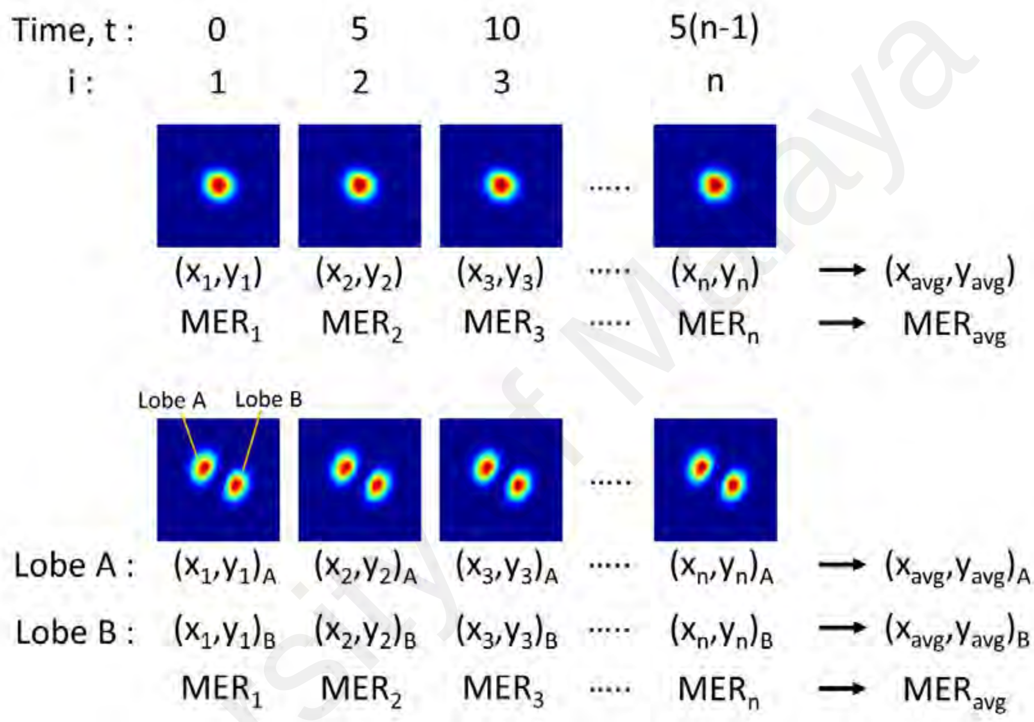

Figure 5.4: Information acquired from each individual mode profile recorded at different time for the determination of average peak position, MER_{avg} and their standard deviations.

In order to investigate the effect of operating wavelength on the PBS output mode profile and power, the above procedures were repeated with different operating wavelengths starting from 1530 until 1560 nm at interval of 10 nm. The LP_{11y} mode profile might become slightly asymmetry at first when the wavelength was changed. Nonetheless, the symmetry LP_{11y} mode could be restored with some minor adjustment on the TMPC paddles. After the recording and measurement of the mode profile and power at the PBS outputs, the TMPC output power at different operating wavelengths was measured by using the power meter. The power loss in the TMPC was deduced by subtracting the TMF output power from the TMPC output power.

Following that, the paddles of the TMPC were tuned to a configuration where LP_{11x} and LP_{01y} modes were obtained at the transmitted and reflected PBS output respectively. This TMPC output state is denoted as TMPC-2. Subsequently, the above procedures were repeated to determine the mode profile and power of the LP_{11x} and LP_{01y} modes at the PBS outputs at different wavelengths.

The mode profiles recorded above were that corresponding to the x- and y-polarised components of the TMPC output beam only. To examine the mode profile corresponding to linear polarisation state in between the x- and y-polarisation, the PBS was rotated around the z-axis to achieve different angles between x- and y-polarisation. The PBS was mounted on a rotation mount to perform the rotation from 0º to 90º at a step size of 10º. The transmitted and reflected output mode profiles of the PBS at each point were recorded. Then, the modal purity of the recorded mode profiles was analysed by the modal decomposition technique to determine the change in mode content at the different linear polarisation states.

5.3 Results and Discussions

5.3.1 Mode Profile, Modal Purity and Mode Power Analysis

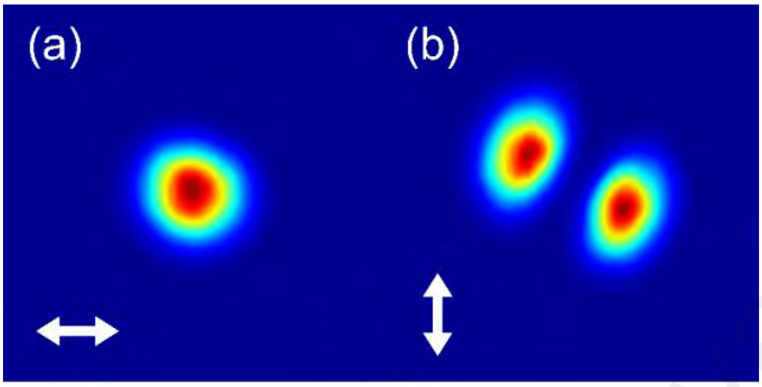

Figure 5.5: Linearly polarised modes recorded at the PBS outputs: (a) LP_{01x} and (b) LP_{11y} modes. The double-headed arrows indicate the state of polarisation of the modes.

Figure 5.5 shows the typical LP_{01x} and LP_{11y} mode profiles recorded at the PBS outputs under the TMPC-1 configuration. Due to cross-coupling between the LP_{11y} degenerate modes (LP_{11ay} and LP_{11by} modes), composition of the degenerate modes in the LP_{11y} output mode profile changed when the TMPC paddles were tuned. Since the LP_{11y} output mode profile is a superposition of the degenerate modes, its orientation depends on the composition of the LP_{11ay} and LP_{11by} modes. A rotated LP_{11y} mode profile (Figure 5.5(b)) is observed if power has been coupled into both LP_{11ay} and LP_{11by} degenerate modes. When the paddles configuration was switched to TMPC-2, LP_{01} and LP_{11} mode profiles similar to that shown in Figure 5.5 were observed but with their polarisation state being rotated 90° as compared to the case of TMPC-1.

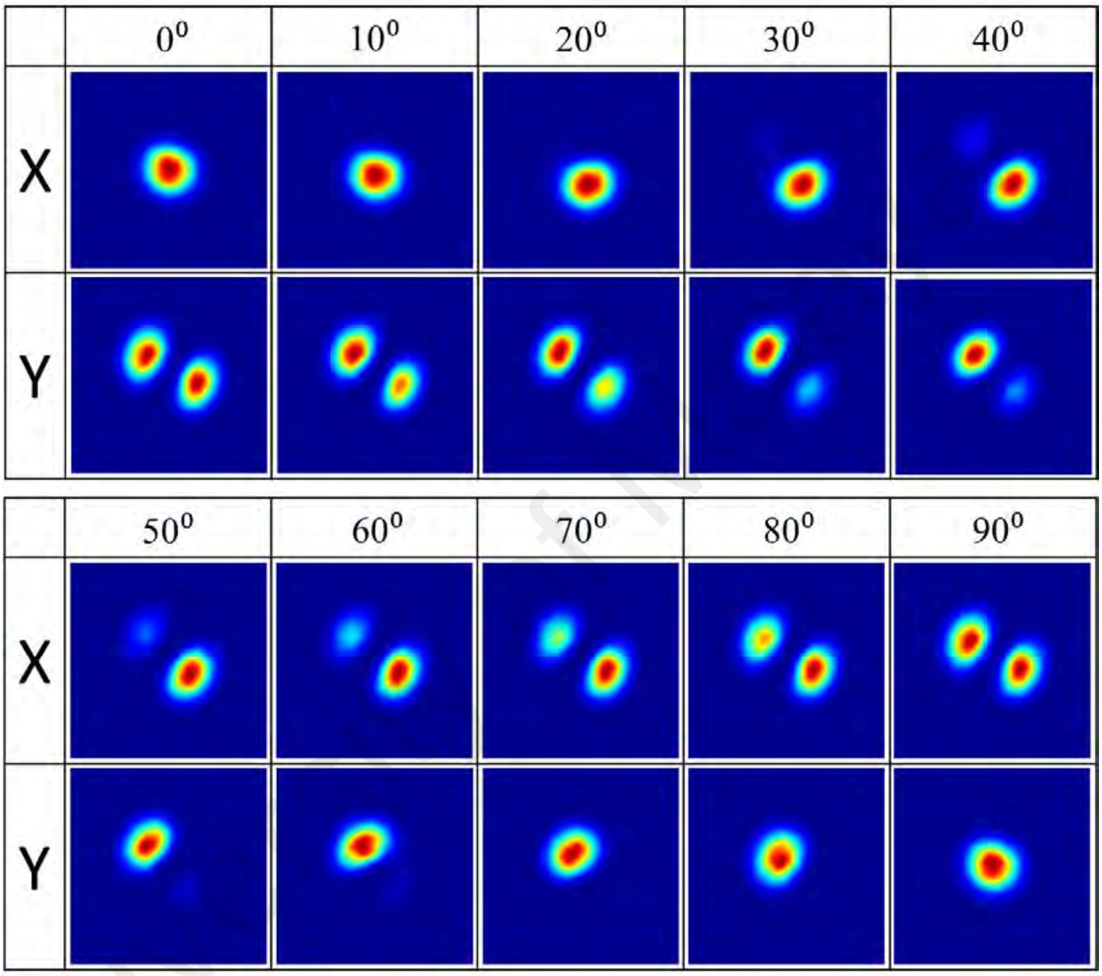

Figure 5.6: Mode profiles recorded at the transmitted (X) and reflected (Y) outputs of the PBS rotated to different angles.

When TMPC-1 was applied, LP_{01} and LP_{11} modes were obtained at the transmitted and reflected outputs of PBS respectively by using the experimental setup shown in Figure 5.2. With the PBS orientation shown in the figure, the transmitted and reflected mode profiles are of x- and y-polarisation respectively. In order to examine the mode profile corresponding to linear polarisation states in between the x- and y-polarisation, the PBS was rotated around the z-axis. The mode profile at the transmitted and reflected outputs were recorded by mode profiler when the PBS was rotated to different angles. Figure 5.6 shows the mode profiles recorded at the PBS outputs when the PBS was rotated from 0º to 90º with a step size of 10º.

Row X and row Y in Figure 5.6 show the mode profiles recorded at the transmitted and reflected PBS outputs respectively. At 0º, LP_{01} and LP_{11} modes were observed at the transmitted and reflected output respectively. These mode profiles are corresponding to the case of un-rotated PBS which gives LP_{01x} and LP_{11y}, similar to that shown in Figure 5.5. When the PBS angle increased, the LP_{01} mode profile at the transmitted output evolved into asymmetry LP_{11} mode and finally a symmetry LP_{11} mode at PBS angle of 90º.

On the other hand, the LP_{11} mode at the reflected output evolved into asymmetry LP_{11} mode and finally a LP_{01} mode when the PBS angle increased from 0º to 90º. At 90º, the polarisation state of the transmitted and reflected output of the PBS have been rotated as much as 90º and they are corresponding to y- and x-polarisation respectively. Therefore, the LP_{11} mode observed at the transmitted output is LP_{11y} mode while the LP_{01} mode observed at the reflected output is LP_{01x} mode.

The recorded mode profiles at the transmitted output of the PBS at different polarisation angles (Row X) were analysed by using numerical method-based modal decomposition technique described in Section 4.2.3 to estimate their modal purity. The modal purity of the recorded mode profiles is shown in Figure 5.7. From the figure, it can be seen that the mode profile recorded at linear polarisation angle (equivalent to PBS angle) of 0º (x-polarisation) has LP_{01} mode content close to 100% while its LP_{11} mode content is near to zero. As the angle increases, the LP_{01} mode content decreases while the LP_{11} mode content increases. At 90º (y-polarisation), the mode profile is purely composed of LP_{11} mode while the LP_{01} mode content has decreased down to zero. For linear polarisation angle in between 0º and 90º, the recorded mode profiles are composed of both LP_{01} and LP_{11} modes.

Meanwhile, the merit function, J indicates the degree of similarity between the measured and reconstructed mode profiles in the form of percentage ranging from 0 to 100%. Merit function in the range of 94% - 99% suggests that the reconstructed mode profile is closely similar to the measured mode profile. Figure 5.8 shows the typical measured and reconstructed LP_{01} and LP_{11} mode profiles with $J \sim 95\%$.

From the difference in the power measured at the TMF and TMPC outputs, the insertion loss of TMPC was estimated to be ~1 dB for the wavelength range of 1530 – 1560 nm. Meanwhile, the insertion loss of PBS was determined by deducting the TMPC output power from the total PBS output power (the sum of the transmitted and reflected output power). The calculation shows that the PBS insertion loss is less than 0.1 dB.

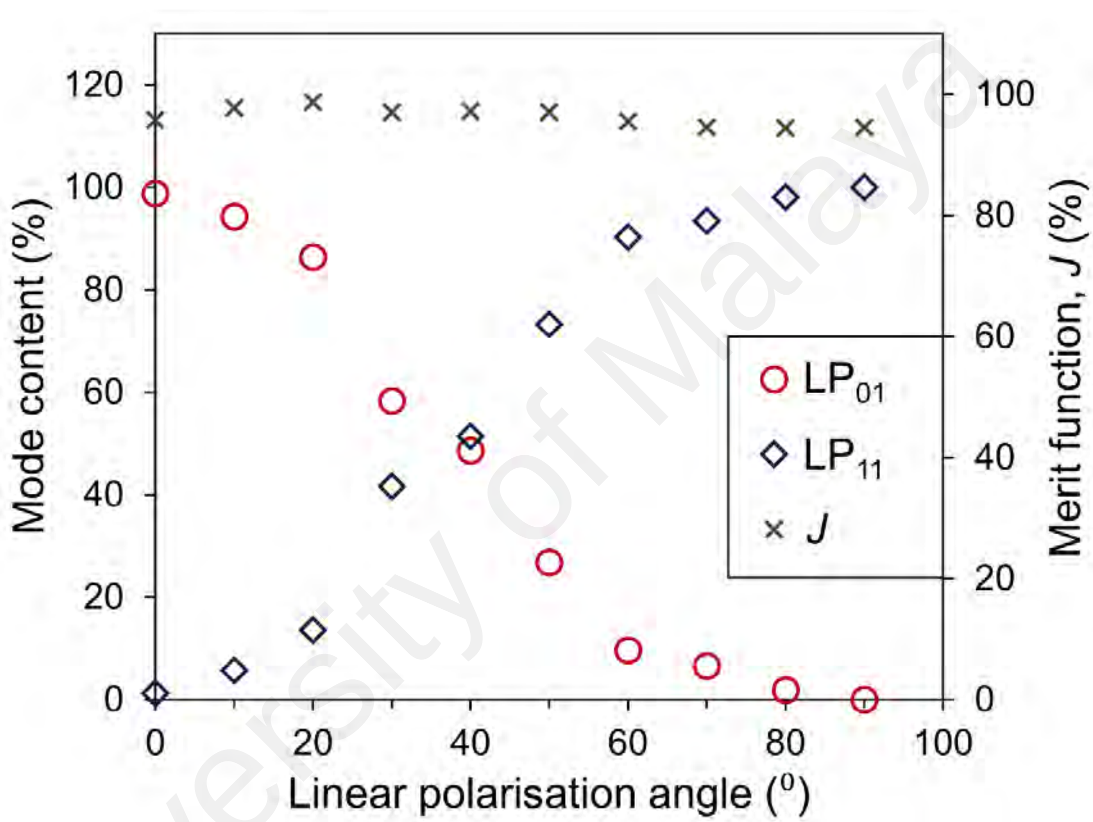

Figure 5.7: Modal content and merit function for mode profiles recorded at the transmitted (X) output of the PBS rotated to different linear polarisation angles.

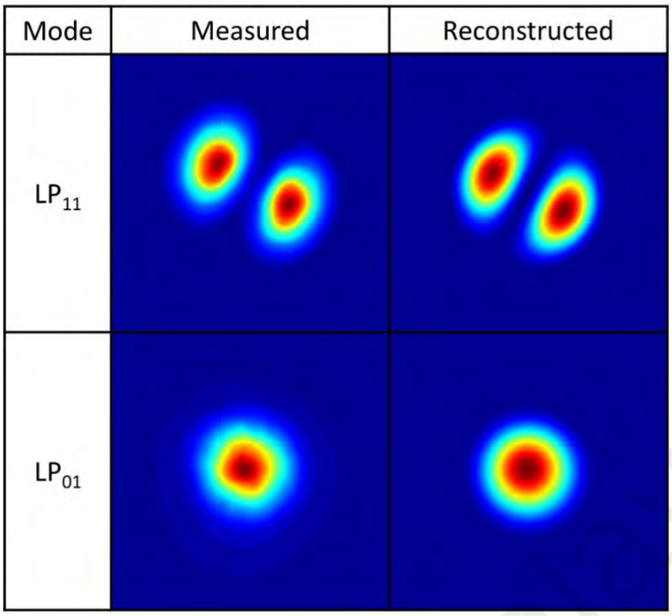

Figure 5.8: The measured and reconstructed LP$_{01}$ and LP$_{11}$ mode profiles by the numerical method-based modal decomposition technique.

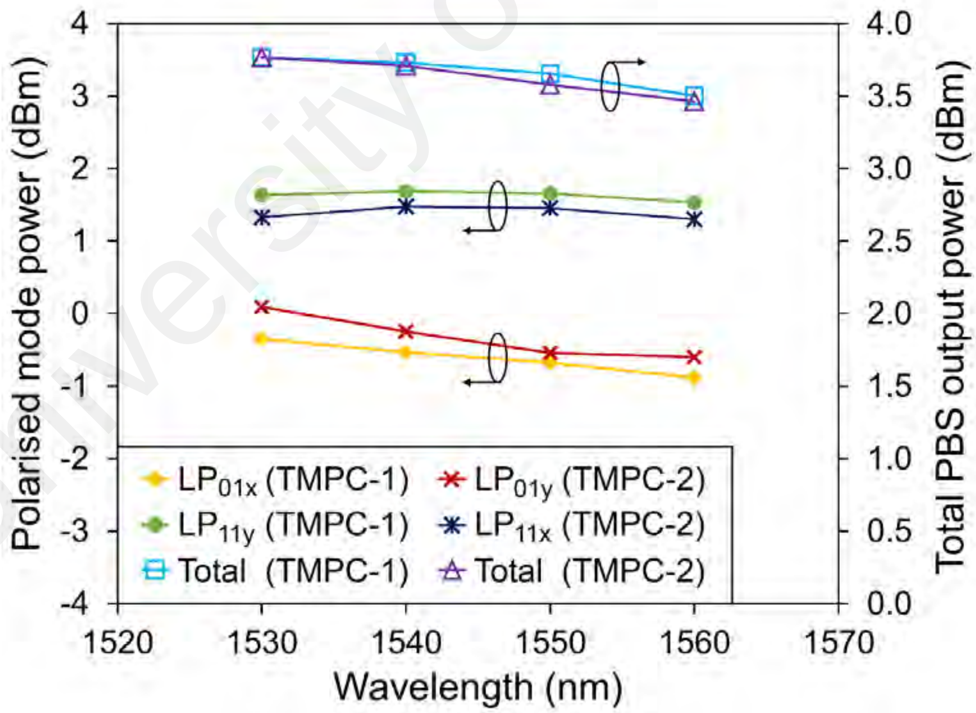

Figure 5.9: Power of the polarised LP$_{01}$ and LP$_{11}$ modes at the PBS outputs at different operating wavelengths for TMPC-1 and TMPC-2.

The total PBS output power for different operating wavelengths and TMPC configurations has been measured. This is shown in Figure 5.9. The total PBS output power decreased from ~3.8 dBm to ~3.5 dBm when the operating wavelength increased from 1530 nm to 1560 nm. The difference between the total PBS output power for the cases of TMPC-1 and TMPC-2 at a specific operating wavelength is found to be less than 0.1 dB. This shows that the change in TMPC configuration does not lead to significant loss in the total output power.

From the same figure, it can be seen that the power of LP_{01} mode is generally lower than LP_{11} mode for both TMPC configurations. This might due to the reason that the core-offset has excited more power in LP_{11} mode than LP_{01} mode. Meanwhile, the difference between the modal power of LP_{01x} (TMPC-1) and LP_{01y} (TMPC-2) is less than 0.5 dB for operating wavelengths in the range of 1530 – 1560 nm. Meanwhile, the modal power of LP_{11x} (TMPC-2) and LP_{11y} (TMPC-1) has difference less than 0.4 dB in the same wavelength range. The small differences indicate that tuning the TMPC from TMPC-1 to TMPC-2 or vice versa can efficiently switch the polarisation states of the LP_{01} and LP_{11} modes between x- and y-polarisations without significantly alter the power of the modes.

5.3.2 Stability of Modal Purity

The modal purity of the LP_{01} and LP_{11} mode profiles recorded at the PBS outputs was determined by the numerical method-based modal decomposition technique. The LP_{01} and LP_{11} modal content obtained from the modal decomposition technique for each mode profile were used to calculate the MER. Then, the MER_{avg} for the mode profiles at PBS outputs obtained under different operating wavelengths and TMPC configurations were calculated based on the method described in Section 5.2. The results are shown in Figure 5.10.

The MER_{avg} of LP_{11} mode in both cases of TMPC-1 (LP_{11y} mode) and TMPC-2 (LP_{11x} mode) are higher than 37.5 dB for operating wavelength ranged from 1530 – 1560 nm. On the other hand, it is in the range of 30 – 33 dB for LP_{01} mode. Inset in Figure 5.10 shows the fluctuation in MER of LP_{11x} mode recorded at the transmitted PBS output for 300 s. Similar fluctuation was observed in the case of LP_{11y}, LP_{01x} and LP_{01y} modes at operating wavelength ranged from 1530 – 1560 nm. The fluctuation might be attributed to: (i) environmental perturbation on the fiber used in the experiment and (ii) instability of the TLS intensity, polarisation or wavelength. The standard deviation of the MER over the 300 s was found to be ≤ 0.5 dB for the four modes observed at the PBS outputs (LP_{01x}, LP_{01y}, LP_{11x} and LP_{11y}) over the operating wavelength range of 1530 – 1560 nm.

By using the peak-finding algorithm, the peak position of the lobes for LP_{01} and LP_{11} modes recorded at the PBS outputs over the period of 300 s was obtained. The peak position of the LP_{01} and LP_{11} lobes as determined by the peak-finding algorithm are marked by white dots in the insets of Figure 5.11. The standard deviations of the peak position over the 300 s period have been determined by the method described in Section 5.2. It is found that the standard deviations are less than 4.5% of the effective mode field radius for operating wavelength ranged from 1530 – 1560 nm as shown in Figure 5.11. The stability of the peak position is related to the stability of the modal purity because fluctuation in the peak position indicates that the modal content of LP_{01} and LP_{11} modes is fluctuating. The calculated standard deviation of the MER and peak position show that the LP_{01} and LP_{11} modes at the PBS outputs are very stable.

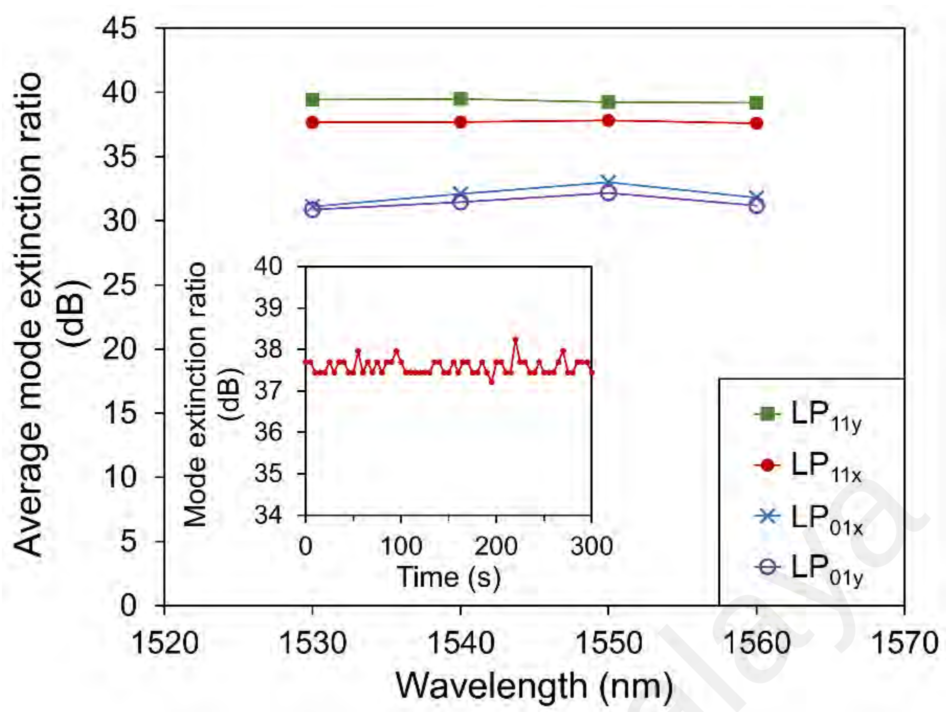

Figure 5.10: MER_{avg} for the polarised LP_{01} and LP_{11} modes recorded at PBS output at different operating wavelengths. Inset: Fluctuation of MER of LP_{11x} mode over a period of 300 s at operating wavelength of 1550 nm.

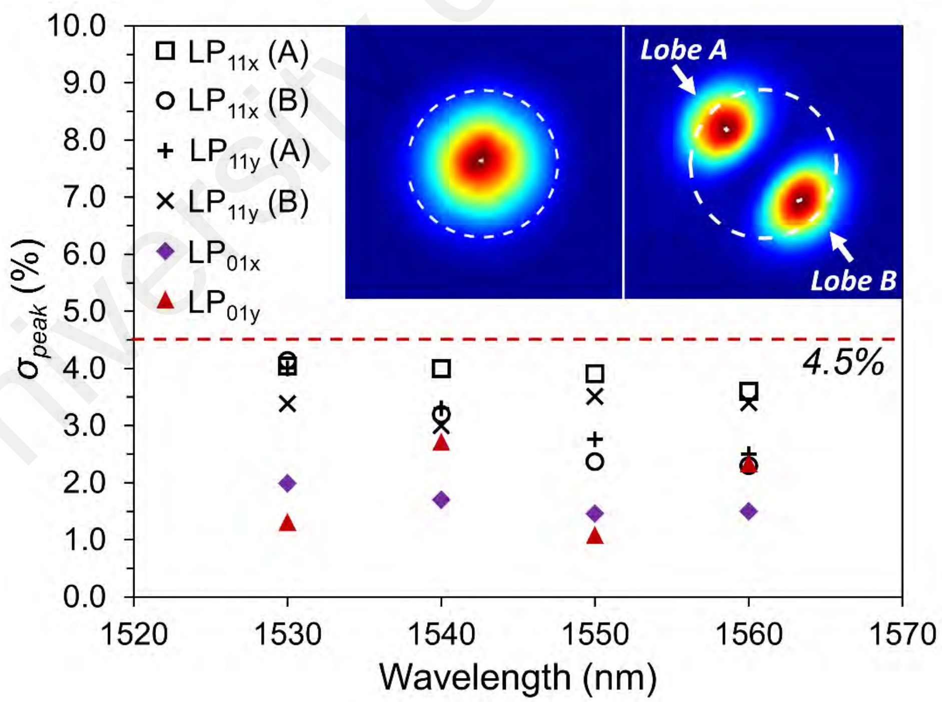

Figure 5.11: Standard deviation of peak position for LP_{01} and LP_{11} modes at different operating wavelengths. Inset: Profiles of LP_{01y} and LP_{11x} modes recorded at PBS output. The white dots indicate the fluctuation of peak position. The white dashed circle shows the diameter of the fiber core.

5.4 Summary

In this chapter, polarisation manipulation of LP_{01} and LP_{11} modes in a TMF was performed by using a TMPC. Firstly, the operating principle of a three-paddle polarisation controller was discussed. Then, it was demonstrated that the TMPC can simultaneously align the two modes into two perpendicular linear polarisation states. By using a PBS, the two modes were split at the TMPC output. The performance of the TMPC polarisation manipulation was examined through the analysis of modal purity and power for LP_{01} and LP_{11} modes recorded at the PBS outputs at different operating wavelengths.

The mode profiles recorded over a period of 300 s were analysed by peak-finding algorithm and numerical method-based modal decomposition technique to determine the stability of the split modes in terms of mode position and modal purity over the 300 s. The standard deviations of the peak position were found to be < 4.5 % of the effective mode field radius for operating wavelength of 1530 – 1560 nm. Meanwhile, the recorded $LP_{01x,y}$ modes have MER_{avg} in the range of 30 – 33 dB while $LP_{11x,y}$ modes have MER_{avg} higher than 37.5 dB for the same operating wavelength range. The standard deviations of the MERs were ≤ 0.5 dB for the four modes ($LP_{01x,y}$ and $LP_{11x,y}$). Mode profiles corresponding to linear polarisation states in between x- and y-polarisations were recorded at the outputs of the PBS rotated to different angles around the z-axis. The modal content of the mode profiles recorded at the transmitted output of the rotated PBS was determined through modal decomposition technique. High purity LP_{01} and LP_{11} modes were obtained at linear polarisation angle of 0° and 90° while the mode profiles with linear polarisation angle in between 0° and 90° were composed of both LP_{01} and LP_{11} modes.

From power measurement, the insertion loss of the TMPC and PBS were ~1 dB and < 0.1 dB respectively. On the other hand, it was found that the difference between the power of LP_{01x} (TMPC-1) and LP_{01y} (TMPC-2) modes measured at the PBS output is less than 0.5 dB for operating wavelength range of 1530 – 1560 nm. The difference is less than 0.4 dB for the case of LP_{11x} (TMPC-2) and LP_{11y} (TMPC-1) modes for the same operating wavelength range.

CHAPTER 6: CONCLUSION AND OUTLOOK

6.1 Conclusion

In conclusion, three techniques have been investigated and experimentally demonstrated for MDM (de)multiplexing applications, namely, titled binary phase plate (BPP), angled-facet two-mode fiber (AFTMF) and three-paddle two-mode fiber polarisation controller (TMPC).

Tilted BPP technique has been proposed and demonstrated to increase the operating wavelength range of a BPP to achieve efficient $LP_{01} \rightarrow LP_{11}$ up-conversion. Theoretical background for the operation of a tilted BPP has been established based on geometrical optics. Then, fused silica BPPs were fabricated by photolithography, chemical wet etching and inductively-coupled plasma (ICP) dry etching processes. The home-made fused silica BPPs were used to verify the mode conversion performance of the tilted BPP technique. It was found that tilting the BPP from 0^0 to 7.5^0 can extend the operating wavelength range for efficient $LP_{01} \rightarrow LP_{11}$ mode conversion as much as 9.16 nm longer than the design wavelength. This provides a convenient mean to achieve efficient mode conversion at a wide spectral range by using a single BPP.

Following that, $LP_{11} \rightarrow LP_{01}$ down-conversion performance of an AFTMF has been investigated. The characteristic of the beam at the TMF output with output facet angle in the range of 0^0 – 43.5^0 was simulated by using OptiFDTD simulator. It was observed that the LP_{11} mode in the TMF turned into a single-lobe beam when the facet angle was in the range of 42.5^0 – 43.5^0. Then, a 43^0 AFTMF was fabricated by mechanical polishing to verify its down-conversion performance experimentally. A single-lobe beam was observed at the AFTMF output in the experiment and the beam was butt-coupled into a target FMF to excite LP_{01} mode in the target FMF. LP_{01} mode recorded at the target FMF output was found to have modal purity higher than 99%. The performance of single-layer and bilayer anti-reflection (AR) coating on the angled-facet has been evaluated to reduce the insertion loss due to Fresnel reflection.

Finally, the performance of a TMPC in polarisation manipulation and mode splitting were investigated. Both LP_{01} and LP_{11} modes were excited in a TMF by core-offset splicing technique. The TMF output was spliced to the TMPC to manipulate the polarisation of LP_{01} and LP_{11} mode in the fiber. It was observed that tuning the paddles of the TMPC can simultaneously manipulate the LP_{01} and LP_{11} modes into perpendicular polarisation states. Then, the two LP modes were split at the TMPC by a polarising beam splitter (PBS). Analysis of the $LP_{01x,y}$ and $LP_{11x,y}$ mode profiles recorded at the PBS outputs over 300 s indicates that the split modes exhibited high modal purity and temporal stability for wavelength range of 1530 nm – 1560 nm (C-band). The work shows that the TMPC-PBS configuration can potentially be used as mode splitter and filter in SDM system.

6.2 Outlook

BPP has been a simple and versatile tool for mode conversion in many of the SDM transmission experiments in early 2010s. It has the same working principle as the SLM but it is simpler to operate. Although BPP might have higher insertion loss and bulkier as compared to all-fiber devices such as photonic lantern and mode coupler, but it remains to be a valuable tool with simple operation procedure for selective modes excitation in an FMF. Its insertion loss can be reduced by applying AR coating on one of the surfaces of the plate (the flat side that is without phase pattern) to minimise the insertion loss induced by Fresnel reflection. The investigation of tilted BPP technique in this work has been focused on $LP_{01} \rightarrow LP_{11}$ mode conversion. The next work should be on exploring the possibility of mode conversion to other higher-order modes (HOMs) by using the tilted BPP technique.

On the other hand, operation of AFTMF is very similar to the mode filtering technique which blocks specific lobes of the higher-order LP mode to perform the mode conversion. It is possible for AFTMF to achieve lower insertion loss as compared to mode filtering technique. Experimental investigation can be performed to study the performance of AR coating on the insertion loss of AFTMF. Besides, $LP_{21} \rightarrow LP_{11}$ down-conversion can be experimentally investigated by fabricating an angled-facet on an FMF that support LP_{21} mode. This down-conversion technique can be adopted in the planar waveguide technology to produce a stable, low loss and miniaturised mode converter.

The manipulation of LP_{01} and LP_{11} modes into perpendicular polarisation states by using different types of polarisation controller (PC) with smaller physical footprint should be investigated such as Lithium Niobate Polarisation Controller. Besides, the understanding on the polarisation manipulation mechanism is far from complete. Effect of strain, twist and bend of an FMF on the phase retardance of different LP modes in the FMF should be investigated to facilitate the design of few-mode fiber PC with better performance.

REFERENCES

Abedin, K. S., Taunay, T. F., Fishteyn, M., Yan, M. F., Zhu, B., Fini, J. M., . . . Wisk, P. W. (2011). Amplification and noise properties of an erbium-doped multicore fiber amplifier. *Optics Express, 19*(17), 16715-16721.

Agrawal, G. P. (1997). *Fiber-optic communication systems* (2nd ed.). New York, USA: Wiley-Interscience.

Agrell, E., Karlsson, M., Chraplyvy, A. R., Richardson, D. J., Krummrich, P. M., Winzer, P., . . . Gisin, N. (2016). Roadmap of optical communications. *Journal of Optics, 18*(6), 063002.

Al Amin, A., Li, A., Chen, S., Chen, X., Gao, G., & Shieh, W. (2011). Dual-LP_{11} mode 4x4 MIMO-OFDM transmission over a two-mode fiber. *Optics Express, 19*(17), 16672-16679.

Ali, M. M., Jung, Y., Lim, K.-S., Islam, M. R., Alam, S.-u., Richardson, D. J., & Ahmad, H. (2015). Characterization of mode coupling in few-mode FBG with selective mode excitation. *IEEE Photonics Technology Letters, 27*(16), 1713-1716.

Antonelli, C., Mecozzi, A., & Shtaif, M. (2013). Raman amplification in multimode fibers with random mode coupling. *Optics Letters, 38*(8), 1188-1190.

Arikawa, M., Ito, T., Gabory, E. L. T. d., & Fukuchi, K. (2015, 27 Sept.-1 Oct. 2015). *Crosstalk reduction using bidirectional signal assignment over square lattice structure 16-core fiber for gradual upgrade of SSMF-based lines.* Paper presented at the European Conference on Optical Communication (ECOC 2015), Valencia, Spain.

Berdagué, S., & Facq, P. (1982). Mode division multiplexing in optical fibers. *Applied Optics, 21*(11), 1950-1955.

Birks, T. A., Gris-Sánchez, I., Yerolatsitis, S., Leon-Saval, S. G., & Thomson, R. R. (2015). The photonic lantern. *Advances in Optics and Photonics, 7*, 107-167.

Birks, T. A., Mangan, B. J., Díez, A., Cruz, J. L., & Murphy, D. F. (2012). "Photonic lantern" spectral filters in multi-core fibre. *Optics Express, 20*(13), 13996-14008.

Blake, J. N., Kim, B. Y., & Shaw, H. J. (1986). Fiber-optic modal coupler using periodic microbending. *Optics Letters, 11*(3), 177-179.

Buck, J. A. (2004). *Fundamentals of optical fibers* (2nd ed.). New Jersey, USA: Wiley-Interscience.

Carpenter, J., & Wilkinson, T. D. (2012). Characterization of multimode fiber by selective mode excitation. *Journal of Lightwave Technology, 30*(10), 1386-1392.

Catalán, L. A. (1962). Some computed optical properties of antireflection coatings. *Journal of the Optical Society of America, 52*(4), 437-440.

Chen, H., Fontaine, N. K., Ryf, R., Jin, C., Huang, B., Shang, K., . . . LaRochelle, S. (2016). Demonstration of Cladding-Pumped Six-Core Erbium-Doped Fiber Amplifier. *Journal of Lightwave Technology, 34*(8), 1654-1660.

Chen, H., Sleiffer, V., Huijskens, F., Uden, R. v., Okonkwo, C., Leoni, P., . . . Koonen, T. (2013). Employing prism-based three-spot mode couplers for high capacity MDM/WDM transmission. *IEEE Photonics Technology Letters, 25*(24), 2474-2477. doi: 10.1109/LPT.2013.2286826

Cui, J., Hong, Z., Fu, S., Chen, B., Tang, M., & Liu, D. (2017). All-fiber polarization manipulation for high-order LP modes with mode profile maintenance. *Optics Express, 25*(15), 18197-18204.

Desurvire, E. B. (2006). Capacity demand and technology challenges for lightwave systems in the next two decades. *Journal of Lightwave Technology, 24*(12), 4697-4710.

Ding, Y., Ou, H., Xu, J., & Peucheret, C. (2013). Silicon photonic integrated circuit mode multiplexer. *IEEE Photonics Technology Letters, 25*(7), 648-651.

Doerr, C. R., & Taunay, T. F. (2011). Silicon photonics core-, wavelength-, and polarization-diversity receiver. *IEEE Photonics Technology Letters, 23*(9), 597-599.

Dong, J., & Chiang, K. S. (2015). Temperature-insensitive mode converters with CO_2-laser written long-period fiber gratings. *IEEE Photonics Technology Letters, 27*(9), 1006-1009.

Ellis, A. D. (2013, 8-12 Sept. 2013). *The MODE-GAP project.* Paper presented at the IEEE Photonics Conference 2013, Washington, USA.

Essiambre, R.-J., Foschini, G. J., Kramer, G., & Winzer, P. J. (2008). Capacity limits of information transport in fiber-optic networks. *Physical Review Letters, 101*(16), 163901.

Essiambre, R.-J., Kramer, G., Winzer, P. J., Foschini, G. J., & Goebel, B. (2010). Capacity limits of optical fiber networks. *Journal of Lightwave Technology, 28*(4), 662-701.

Fontaine, N. K. (2013, 8-10 July 2013). *Photonic lantern spatial multiplexers in space-division multiplexing.* Paper presented at the IEEE Photonics Society Summer Topical Meeting Series 2013, Waikoloa, USA.

Fontaine, N. K., Huang, B., Eznaveh, Z. S., Chen, H., Cang, J., Ercan, B., . . . Amezcua-Correa, R. (2016, 20-24 March 2016). *Multi-mode optical fiber amplifier supporting over 10 spatial modes.* Paper presented at the Optical Fiber Communications Conference and Exhibition (OFC 2016), Anaheim, USA.

Fontaine, N. K., Ryf, R., Bland-Hawthorn, J., & Leon-Saval, S. G. (2012). Geometric requirements for photonic lanterns in space division multiplexing. *Optics Express, 20*(24), 27123-27132.

Gambling, W. A. (2000). The rise and rise of optical fibers. *IEEE Journal of Selected Topics in Quantum Electronics, 6*(6), 1084-1093.

Gao, Y., Sun, J., Chen, G., & Sima, C. (2015). Demonstration of simultaneous mode conversion and demultiplexing for mode and wavelength division multiplexing systems based on tilted few-mode fiber Bragg gratings. *Optics Express, 23*(8), 9959-9967.

Giles, I., Obeysekara, A., Chen, R., Giles, D., Poletti, F., & Richardson, D. (2012). Fiber LPG mode converters and mode selection technique for multimode SDM. *IEEE Photonics Technology Letters, 24*(21), 1922-1925.

Gnauck, A., Tkach, R. W., Chraplyvy, A. R., & Li, T. (2008). High-capacity optical transmission systems. *Journal of Lightwave Technology, 26*(9), 1032-1045.

Gruner-Nielsen, L., Sun, Y., Nicholson, J. W., Jakobsen, D., Jespersen, K. G., Lingle, R., & Palsdottir, B. (2012). Few mode transmission fiber with low DGD, low mode coupling, and low loss. *Journal of Lightwave Technology, 30*(23), 3693-3698. doi: 10.1109/JLT.2012.2227243

Hayashi, T. (2013). Multi-core optical fibers. In I. Kaminow, T. Li & A. Willner (Eds.), *Optical Fiber Telecommunications* (Vol. VI A, pp. 321-352). Massachusetts, USA: Academic Press.

Hecht, J. (1999). *City of light: The story of fiber optics*. New York, USA: Oxford University Press.

Hecht, J. (2016). The bandwidth bottleneck. *Nature, 536*(7615), 139-142.

Ho, K.-P., & Kahn, J. M. (2013). Mode coupling and its impact on spatially multiplexed systems. In I. Kaminow, T. Li & A. Willner (Eds.), *Optical Fiber Telecommunications* (Vol. VI B, pp. 491-568). Massachusetts, USA: Academic Press.

Hong, Z., Fu, S., Yu, D., Tang, M., & Liu, D. (2016). All-fiber tunable LP_{11} mode rotator with 360° range. *IEEE Photonics Journal, 8*(5), 7102007.

Huang, B., Xia, C., Matz, G., Bai, N., & Li, G. (2013, 17-21 March 2013). *Structured directional coupler pair for multiplexing of degenerate modes.* Paper presented at the Optical Fiber Communication Conference and Exposition and the National Fiber Optic Engineers Conference (OFC/NFOEC 2013), Anaheim, USA.

Huang, L., Guo, S., Leng, J., Lü, H., Zhou, P., & Cheng, X. a. (2015). Real-time mode decomposition for few-mode fiber based on numerical method. *Optics Express, 23*(4), 4620-4629.

Igarashi, K., Park, K. J., Tsuritani, T., Morita, I., & Kim, B. Y. (2018). All-fiber-based selective mode multiplexer and demultiplexer for weakly-coupled mode-division multiplexed systems. *Optics Communications, 408*, 58-62.

Igarashi, K., Souma, D., Takeshima, K., & Tsuritani, T. (2015). Selective mode multiplexer based on phase plates and Mach-Zehnder interferometer with image inversion function. *Optics Express, 23*(1), 183-194.

Igarashi, K., Souma, D., Tsuritani, T., & Morita, I. (2014). Performance evaluation of selective mode conversion based on phase plates for a 10-mode fiber. *Optics Express, 22*(17), 20881-20893.

IIzuka, K. (2002). *Elements of photonics volume II*. New York, USA: Wiley-Interscience.

Inao, S., Sato, T., Sentsui, S., Kuroha, T., & Nishimura, Y. (1979, 6 March 1979). *Multicore optical fiber.* Paper presented at the Optical Fiber Communication, Washington, D.C., USA.

Ismaeel, R., & Brambilla, G. (2016). Removing the directional degeneracy of LP_{11} mode in a fused-type mode selective coupler. *Journal of Lightwave Technology, 34*(4), 1242-1246.

Ismaeel, R., Lee, T., Oduro, B., Jung, Y., & Brambilla, G. (2014). All-fiber fused directional coupler for highly efficient spatial mode conversion. *Optics Express, 22*(10), 11610-11619.

Jin, C., Huang, B., Shang, K., Chen, H., Ryf, R., Essiambre, R. J., . . . LaRochelle, S. (2015, 27 Sept.-1 Oct. 2015). *Efficient annular cladding amplifier with six, three-mode cores.* Paper presented at the European Conference on Optical Communication (ECOC 2015), Valencia, Spain.

Jung, Y., Alam, S., Li, Z., Dhar, A., Giles, D., Giles, I. P., . . . Richardson, D. J. (2011). First demonstration and detailed characterization of a multimode amplifier for space division multiplexed transmission systems. *Optics Express, 19*(26), B952-B957.

Jung, Y., Lim, E. L., Kang, Q., May-Smith, T. C., Wong, N. H. L., Standish, R., . . . Richardson, D. J. (2014). Cladding pumped few-mode EDFA for mode division multiplexed transmission. *Optics Express, 22*(23), 29008-29013.

Kao, K. C., & Hockham, G. A. (1966). Dielectric-fibre surface waveguides for optical frequencies. *Proceedings of the Institution of Electrical Engineers, 113*(7), 1151-1158.

Kasahara, M., Saitoh, K., Sakamoto, T., Hanzawa, N., Matsui, T., Tsujikawa, K., . . . Koshiba, M. (2013). Design of few-mode fibers for mode-division multiplexing transmission. *IEEE Photonics Journal, 5*(6), 7201207-7201207.

Kilper, D. C., & Tucker, R. S. (2013). Energy-efficient telecommunications. In I. Kaminow, T. Li & A. Willner (Eds.), *Optical Fiber Telecommunications* (Vol. VI B, pp. 747-791). Massachusetts, USA: Academic Press.

Kitayama, K., & Diamantopoulos, N.-P. (2017). Few-mode optical fibers: Original motivation and recent progress. *IEEE Communications Magazine, 55*(8), 163-169.

Klaus, W., Sakaguchi, J., Puttnam, B. J., Awaji, Y., Wada, N., Kobayashi, T., & Watanabe, M. (2012). Free-space coupling optics for multicore fibers. *IEEE Photonics Technology Letters, 24*(21), 1902-1905.

Kobayashi, T., Takara, H., Sano, A., Mizuno, T., Kawakami, H., Miyamoto, Y., . . . Morioka, T. (2013, 22-26 Sept. 2013). *2×344 Tb/s propagation-direction interleaved transmission over 1500-km MCF enhanced by multicarrier full electric-field digital back-propagation.* Paper presented at the European Conference and Exhibition on Optical Communication (ECOC 2013), London, UK.

Koebele, C., Salsi, M., Milord, L., Ryf, R., Bolle, C., Sillard, P., . . . Charlet, G. (2011, 18-22 Sept. 2011). *40km transmission of five mode division multiplexed data streams at 100Gb/s with low MIMO-DSP complexity.* Paper presented at the European Conference and Exhibition on Optical Communication (ECOC 2011), Geneva, Switzerland.

Koebele, C., Salsi, M., Sperti, D., Tran, P., Brindel, P., Mardoyan, H., . . . Charlet, G. (2011). Two mode transmission at 2x100Gb/s, over 40km-long prototype few-mode fiber, using LCOS-based programmable mode multiplexer and demultiplexer. *Optics Express, 19*(17), 16593-16600.

Kogelnik, H., & Winzer, P. J. (2012). Modal birefringence in weakly guiding fibers. *Journal of Lightwave Technology, 30*(14), 2240-2245.

Kokubun, Y. (2018). Rigorous mode theory and analysis of few-mode fibers. *Japanese Journal of Applied Physics, 57*, 08PA05.

Koonen, A. M. J., Chen, H., van den Boom, H. P. A., & Raz, O. (2012). Silicon photonic integrated mode multiplexer and demultiplexer. *IEEE Photonics Technology Letters, 24*(21), 1961-1964.

Krummrich, P. M. (2011). Spatial multiplexing for high capacity transport. *Optical Fiber Technology, 17*(5), 480-489.

Kumar, A., & Ghatak, A. (2011). *Polarization of light with applications in optical fibers*. Washington, USA: SPIE.

Labroille, G., Barré, N., Pinel, O., Denolle, B., Lenglé, K., Garcia, L., . . . Morizur, J.-F. (2017). Characterization and applications of spatial mode multiplexers based on Multi-Plane Light Conversion. *Optical Fiber Technology, 35*, 93-99.

Labroille, G., Denolle, B., Jian, P., Genevaux, P., Treps, N., & Morizur, J.-F. (2014). Efficient and mode selective spatial mode multiplexer based on multi-plane light conversion. *Optics Express, 22*(13), 15599-15607.

Lee, K. S., & Erdogan, T. (2000). Fiber mode coupling in transmissive and reflective tilted fiber gratings. *Applied Optics, 39*(9), 1394-1404.

Lee, K. S., & Erdogan, T. (2001). Fiber mode conversion with tilted gratings in an optical fiber. *Journal of the Optical Society of America A, 18*(5), 1176-1185.

Lefevre, H. C. (1980). Single-mode fibre fractional wave devices and polarisation controllers. *Electronics Letters, 16*(20), 778-780.

Leon-Saval, S. G., Argyros, A., & Bland-Hawthorn, J. (2010). Photonic lanterns: a study of light propagation in multimode to single-mode converters. *Optics Express, 18*(8), 8430-8439.

Leon-Saval, S. G., Argyros, A., & Bland-Hawthorn, J. (2013). Photonic lanterns. *Nanophotonics, 2*(5-6), 429-440.

Leon-Saval, S. G., Fontaine, N. K., & Amezcua-Correa, R. (2017). Photonic lantern as mode multiplexer for multimode optical communications. *Optical Fiber Technology, 35*, 46-55.

Leon-Saval, S. G., Fontaine, N. K., Salazar-Gil, J. R., Ercan, B., Ryf, R., & Bland-Hawthorn, J. (2014). Mode-selective photonic lanterns for space-division multiplexing. *Optics Express, 22*(1), 1036-1044.

Li, A., Chen, X., Amin, A. A., Ye, J., & Shieh, W. (2012). Space-division multiplexed high-speed superchannel transmission over few-mode fiber. *Journal of Lightwave Technology, 30*(24), 3953-3964.

Li, G., Bai, N., Zhao, N., & Xia, C. (2014). Space-division multiplexing: the next frontier in optical communication. *Advances in Optics and Photonics, 6*(4), 413-487.

Li, M., Hoover, B., Li, S., Bickham, S., Ten, S., Ip, E., . . . Wang, T. (2012, 2-6 July 2012). *Low delay and large effective area few-mode fibers for mode-division multiplexing.* Paper presented at the Opto-Electronics and Communications Conference 2012, Busan, South Korea.

Love, J. D., & Riesen, N. (2012). Mode-selective couplers for few-mode optical fiber networks. *Optics Letters, 37*(19), 3990-3992.

Maruyama, R., Kuwaki, N., Matsuo, S., & Ohashi, M. (2014). Two mode optical fibers with low and flattened differential modal delay suitable for WDM-MIMO combined system. *Optics Express, 22*(12), 14311-14321.

Matsuo, S., Sasaki, Y., Akamatsu, T., Ishida, I., Takenaga, K., Okuyama, K., . . . Kosihba, M. (2012). 12-core fiber with one ring structure for extremely large capacity transmission. *Optics Express, 20*(27), 28398-28408.

Mizuno, T., & Miyamoto, Y. (2017). High-capacity dense space division multiplexing transmission. *Optical Fiber Technology, 35*, 108-117.

Mohammed, W. S., Pitchumani, M., Mehta, A. A., & Johnson, E. G. (2006). Selective excitation of the LP_{11} mode in step index fiber using a phase mask. *Optical Engineering, 45*(7), 074602.

Mori, T., Sakamoto, T., Wada, M., Urushibara, A., Yamamoto, T., & Yamamoto, F. (2015, 27 Sept.-1 Oct. 2015). *Experimental evaluation of nonlinear tolerance of* *two LP mode fibre in optical MIMO transmission.* Paper presented at the European Conference on Optical Communication (ECOC 2015), Valencia, Spain.

Morioka, T. (2009, 13-17 July 2009). *New generation optical infrastructure technologies: "EXAT initiative" towards 2020 and beyond.* Paper presented at the OptoElectronics and Communications Conference (OECC 2009), Hong Kong SAR, China.

Morioka, T., Awaji, Y., Ryf, R., Winzer, P., Richardson, D., & Poletti, F. (2012). Enhancing optical communications with brand new fibers. *IEEE Communications Magazine, 50*(2), s31-s42.

Murshid, S., Grossman, B., & Narakorn, P. (2008). Spatial domain multiplexing: A new dimension in fiber optic multiplexing. *Optics & Laser Technology, 40*(8), 1030-1036.

Nakamura, A., Okamoto, K., Koshikiya, Y., & Manabe, T. (2016). Effective mode field diameter for LP_{11} mode and its measurement technique. *IEEE Photonics Technology Letters, 28*(22), 2553-2556. doi: 10.1109/LPT.2016.2605639

Noordegraaf, D., Skovgaard, P. M. W., Maack, M. D., Bland-Hawthorn, J., Haynes, R., & Lægsgaard, J. (2010). Multi-mode to single-mode conversion in a 61 port Photonic Lantern. *Optics Express, 18*(5), 4673-4678.

Noordegraaf, D., Skovgaard, P. M. W., Nielsen, M. D., & Bland-Hawthorn, J. (2009). Efficient multi-mode to single-mode coupling in a photonic lantern. *Optics Express, 17*(3), 1988-1994.

Okamoto, K. (2006). *Fundamentals of optical waveguides* (2nd ed.). USA: Academic Press.

Peckham, D. W., Sun, Y., McCurdy, A., & Lingle, R., Jr. (2013). Few-mode fiber technology for spatial multiplexing. In I. Kaminow, T. Li & A. Willner (Eds.), *Optical Fiber Telecommunications* (Vol. VI A, pp. 283-319). Massachusetts, USA: Academic Press.

Qian, D., Ip, E., Huang, M.-F., Li, M.-J., Dogariu, A., Zhang, S., . . . Wang, T. (2012, 14-18 Sept. 2012). *1.05Pb/s transmission with 109b/s/Hz spectral efficiency using hybrid single- and few-mode cores.* Paper presented at the Frontiers in Optics 2012/Laser Science XXVIII, New York, USA.

Ramachandran, S., Wang, Z., & Yan, M. (2002). Bandwidth control of long-period grating-based mode converters in few-mode fibers. *Optics Letters, 27*(9), 698-700.

Randel, S., Ryf, R., Sierra, A., Winzer, P. J., Gnauck, A. H., Bolle, C. A., . . . Lingle, R. (2011). 6×56-Gb/s mode-division multiplexed transmission over 33-km few-mode fiber enabled by 6×6 MIMO equalization. *Optics Express, 19*(17), 16697-16707.

Richardson, D. J., Fini, J. M., & Nelson, L. E. (2013). Space-division multiplexing in optical fibres. *Nature Photonics, 7*, 354-362.

Riesen, N., Gross, S., Love, J. D., Sasaki, Y., & Withford, M. J. (2017). Monolithic mode-selective few-mode multicore fiber multiplexers. *Scientific Reports, 7*, 6971.

Riesen, N., & Love, J. D. (2012). Weakly-guiding mode-selective fiber couplers. *IEEE Journal of Quantum Electronics, 48*(7), 941-945.

Riesen, N., & Love, J. D. (2013). Ultra-broadband tapered mode-selective couplers for few-mode optical fiber networks. *IEEE Photonics Technology Letters, 25*(24), 2501-2504.

Ryf, R., Esmaeelpour, M., Fontaine, N. K., Chen, H., Gnauck, A. H., Essiambre, R., . . . Lingle, R. (2015, 27 Sept.-1 Oct. 2015). *Distributed Raman amplification based transmission over 1050-km few-mode fiber.* Paper presented at the European Conference on Optical Communication (ECOC 2015), Valencia, Spain.

Ryf, R., Essiambre, R., Gnauck, A. H., Randel, S., Mestre, M. A., Schmidt, C., . . . Sasaki, T. (2012, 4-8 March 2012). *Space-division multiplexed transmission over 4200-km 3-core microstructured fiber.* Paper presented at the Optical Fiber Communication Conference and Exposition and the National Fiber Optic Engineers Conference (OFC/NFOEC 2012), Los Angeles, USA.

Ryf, R., Essiambre, R., Hoyningen-Huene, J. v., & Winzer, P. J. (2012, 4-8 March 2012). *Analysis of mode-dependent gain in Raman amplified few-mode fiber.* Paper presented at the Optical Fiber Communication Conference and Exposition and the National Fiber Optic Engineers Conference (OFC/NFOEC 2012), Los Angeles, USA.

Ryf, R., Fontaine, N. K., & Essiambre, R. (2012). Spot-based mode couplers for mode-multiplexed transmission in few-mode fiber. *IEEE Photonics Technology Letters, 24*(21), 1973-1976.

Ryf, R., Fontaine, N. K., Guan, B., Essiambre, R., Randel, S., Gnauck, A. H., . . . Sasaki, T. (2014, 21-25 Sept. 2014). *1705-km transmission over coupled-core fibre supporting 6 spatial modes.* Paper presented at the European Conference on Optical Communication (ECOC 2014), Cannes, France.

Ryf, R., Fontaine, N. K., Montoliu, M., Randel, S., Chang, S. H., Chen, H., . . . Sasaki, T. (2014, 9-13 March 2014). *Space-division multiplexed transmission over 3×3 coupled-core multicore fiber.* Paper presented at the Optical Fiber Communications Conference and Exhibition (OFC 2014), San Francisco, USA.

Ryf, R., Fontaine, N. K., Montoliu, M., Randel, S., Ercan, B., Chen, H., . . . Lingle, R. (2014, 9-13 March 2014). *Photonic-lantern-based mode multiplexers for few-mode-fiber transmission.* Paper presented at the OFC 2014, San Francisco, USA.

Ryf, R., Mestre, M. A., Gnauck, A. H., Randel, S., Schmidt, C., Essiambre, R., . . . Lingle, R. (2012, 4-8 March 2012). *Low-loss mode coupler for mode-multiplexed transmission in few-mode fiber.* Paper presented at the Optical Fiber Communication Conference and Exposition and the National Fiber Optic Engineers Conference (OFC/NFOEC 2012), Los Angeles, USA.

Ryf, R., Randel, S., Gnauck, A. H., Bolle, C., Essiambre, R., Winzer, P. J., . . . Lingle, R. (2011, 6-10 March 2011). *Space-division multiplexing over 10 km of three-mode fiber using coherent 6 × 6 MIMO processing.* Paper presented at the Optical Fiber Communication Conference/National Fiber Optic Engineers Conference 2011, Los Angeles, USA.

Ryf, R., Randel, S., Gnauck, A. H., Bolle, C., Sierra, A., Mumtaz, S., . . . Lingle, R. (2012). Mode-division multiplexing over 96 km of few-mode fiber using coherent 6 x 6 MIMO processing. *Journal of Lightwave Technology, 30*(4), 521-531.

Ryf, R., Sierra, A., Essiambre, R., Randel, S., Gnauck, A. H., Bolle, C., . . . Lingle, R. (2011, 18-22 Sept. 2011). *Mode-equalized distributed Raman amplification in 137-km few-mode fiber.* Paper presented at the European Conference and Exhibition on Optical Communication (ECOC 2011), Geneva, Switzerland.

Saitoh, K., & Matsuo, S. (2016). Multicore Fiber Technology. *Journal of Lightwave Technology, 34*(1), 55-66.

Sakaguchi, J., Awaji, Y., Wada, N., Kanno, A., Kawanishi, T., Hayashi, T., . . . Watanabe, M. (2011, 6-10 March 2011). *109-Tb/s (7x97x172-Gb/s SDM/WDM/PDM) QPSK transmission through 16.8-km homogeneous multi-core fiber.* Paper presented at the Optical Fiber Communication Conference/National Fiber Optic Engineers Conference 2011, Los Angeles, California.

Sakaguchi, J., Klaus, W., Puttnam, B. J., Mendinueta, J. M. D., Awaji, Y., Wada, N., . . . Jensen, R. V. (2014). 19-core MCF transmission system using EDFA with shared core pumping coupled via free-space optics. *Optics Express, 22*(1), 90-95.

Sakamoto, T., Mori, T., Yamamoto, T., & Tomita, S. (2012). Differential mode delay managed transmission line for WDM-MIMO system using multi-step index fiber. *Journal of Lightwave Technology, 30*(17), 2783-2787.

Sakata, H., Sano, H., & Harada, T. (2014). Tunable mode converter using electromagnet-induced long-period grating in two-mode fiber. *Optical Fiber Technology, 20*(3), 224-227.

Saleh, B. E. A., & Teich, M. C. (1991). *Fundamentals of photonics*. USA: Wiley-Interscience.

Salsi, M., Koebele, C., Sperti, D., Tran, P., Mardoyan, H., Brindel, P., . . . Charlet, G. (2012). Mode-division multiplexing of 2 x 100 Gb/s channels using an LCOS-based spatial modulator. *Journal of Lightwave Technology, 30*(4), 618-623.

Sano, A., Takara, H., Kobayashi, T., Kawakami, H., Kishikawa, H., Nakagawa, T., . . . Morioka, T. (2013). 409-Tb/s + 409-Tb/s crosstalk suppressed bidirectional MCF transmission over 450 km using propagation-direction interleaving. *Optics Express, 21*(14), 16777-16783.

Sano, A., Takara, H., Kobayashi, T., & Miyamoto, Y. (2014). Crosstalk-managed high capacity long haul multicore fiber transmission with propagation-direction interleaving. *Journal of Lightwave Technology, 32*(16), 2771-2779.

Sato, K., Maruyama, R., Kuwaki, N., Matsuo, S., & Ohashi, M. (2013). Optimized graded index two-mode optical fiber with low DMD, large A_{eff} and low bending loss. *Optics Express, 21*(14), 16231-16238.

Schulze, C., Brüning, R., Schröter, S., & Duparré, M. (2015). Mode Coupling in Few-Mode Fibers Induced by Mechanical Stress. *Journal of Lightwave Technology, 33*(21), 4488-4496.

Sillard, P. (2011). New fibers for ultra-high capacity transport. *Optical Fiber Technology, 17*, 495-502.

Sillard, P. (2015). Next-generation fibers for space-division-multiplexed transmissions. *Journal of Lightwave Technology, 33*(5), 1092-1099.

Sillard, P., Bigot-Astruc, M., & Molin, D. (2014). Few-mode fibers for mode-division-multiplexed systems. *Journal of Lightwave Technology, 32*(16), 2824-2829.

Sillard, P., Molin, D., Bigot-Astruc, M., Jongh, K. D., Achten, F., Velázquez-Benítez, A. M., . . . Okonkwo, C. M. (2016). Low-differential-mode-group-delay 9-LP-mode fiber. *Journal of Lightwave Technology, 34*(2), 425-430.

Sleiffer, V. A. J. M., Jung, Y., Veljanovski, V., van Uden, R. G. H., Kuschnerov, M., Chen, H., . . . de Waardt, H. (2012). 73.7 Tb/s (96 x 3 x 256-Gb/s) mode-division-multiplexed DP-16QAM transmission with inline MM-EDFA. *Optics Express, 20*(26), B428-B438.

Song, K. Y., Hwang, I. K., Yun, S. H., & Kim, B. Y. (2002). High performance fused-type mode-selective coupler using elliptical core two-mode fiber at 1550 nm. *IEEE Photonics Technology Letters, 14*(4), 501-503.

Song, K. Y., & Kim, B. Y. (2003). Broad-band LP_{02} mode excitation using a fused-type mode-selective coupler. *IEEE Photonics Technology Letters, 15*(12), 1734-1736.

Sorin, W. V., Kim, B. Y., & Shaw, H. J. (1986). Highly selective evanescent modal filter for two-mode optical fibers. *Optics Letters, 11*(9), 581-583.

Spaleniak, I., Jovanovic, N., Gross, S., Ireland, M. J., Lawrence, J. S., & Withford, M. J. (2013). Integrated photonic building blocks for next-generation astronomical instrumentation II: the multimode to single mode transition. *Optics Express, 21*(22), 27197-27208.

Strasser, T. A., Pedrazzani, J. R., & Andrejco, M. J. (1997, 16-21 Feb. 1997). *Reflective-mode conversion with UV-induced phase gratings in two-mode fiber.* Paper presented at the Optical Fiber Communication Conference (OFC 1997), Dallas, USA.

Synder, A. W., & Love, J. D. (1983). *Optical waveguide theory*. London, UK: Chapman & Hall.

Takahashi, H., Tsuritani, T., de Gabory, E. L. T., Ito, T., Peng, W. R., Igarashi, K., . . . Suzuki, M. (2013). First demonstration of MC-EDFA-repeatered SDM transmission of 40 x 128-Gbit/s PDM-QPSK signals per core over 6,160-km 7-core MCF. *Optics Express, 21*(1), 789-795.

Takara, H., Mizuno, T., Kawakami, H., Miyamoto, Y., Masuda, H., Kitamura, K., . . . Yamada, M. (2014, 21-25 Sept. 2014). *120.7-Tb/s (7 SDM/180 WDM/95.8 Gb/s) MCF-ROPA unrepeatered transmission of PDM-32QAM channels over 204 km.* Paper presented at the European Conference on Optical Communication (ECOC 2014), Cannes, France.

Takara, H., Sano, A., Kobayashi, T., Kubota, H., Kawakami, H., Matsuura, A., . . . Morioka, T. (2012, 16-20 Sept. 2012). *1.01-Pb/s (12 SDM/222 WDM/456 Gb/s) crosstalk-managed transmission with 91.4-b/s/Hz aggregate spectral efficiency.* Paper presented at the European Conference and Exhibition on Optical Communication (ECOC 2012), Amsterdam, Netherlands.

Takenaga, K., Arakawa, Y., Tanigawa, S., Guan, N., Matsuo, S., Saitoh, K., & Koshiba, M. (2011, 6-10 March 2011). *Reduction of crosstalk by trench-assisted multi-core* *fiber.* Paper presented at the Optical Fiber Communication Conference and Exposition and the National Fiber Optic Engineers Conference (OFC/NFOEC 2011), Los Angeles, USA.

Takenaga, K., Matsuo, S., Saitoh, K., & Koshiba, M. (2013, 8-10 July 2013). *Multicore fiber with ring structure.* Paper presented at the IEEE Photonics Society Summer Topical Meeting Series 2013, Waikoloa, USA.

Takenaga, K., Sasaki, Y., Guan, N., Matsuo, S., Kasahara, M., Saitoh, K., & Koshiba, M. (2012). Large effective-area few-mode multicore fiber. *IEEE Photonics Technology Letters, 24*(21), 1941-1944.

Thomson, R. R., Birks, T. A., Leon-Saval, S. G., Kar, A. K., & Bland-Hawthorn, J. (2011). Ultrafast laser inscription of an integrated photonic lantern. *Optics Express, 19*(6), 5698-5705.

Thornburg, W. Q., Corrado, B. J., & Zhu, X. D. (1994). Selective launching of higher-order modes into an optical fiber with an optical phase shifter. *Optics Letters, 19*(7), 454-456.

Uden, R. G. H. v., Correa, R. A., Antonio-Lopez, E., Huijskens, F. M., Li, G., Schulzgen, A., . . . Okonkwo, C. M. (2014, 21-25 Sept. 2014). *1 km hole-assisted few-mode multi-core fiber 32QAM WDM transmission.* Paper presented at the European Conference on Optical Communication (ECOC 2014), Cannes, France.

Ulrich, R., Rashleigh, S. C., & Eickhoff, W. (1980). Bending-induced birefringence in single-mode fibers. *Optics Letters, 5*(6), 273-275.

van Uden, R. G. H., Correa, R. A., Lopez, E. A., Huijskens, F. M., Xia, C., Li, G., . . . Okonkwo, C. M. (2014). Ultra-high-density spatial division multiplexing with a few-mode multicore fibre. *Nature Photonics, 8*, 865-870.

Velazquez-Benitez, A. M., Alvarado, J. C., Lopez-Galmiche, G., Antonio-Lopez, J. E., Hernández-Cordero, J., Sanchez-Mondragon, J., . . . Amezcua-Correa, R. (2015). Six mode selective fiber optic spatial multiplexer. *Optics Letters, 40*(8), 1663-1666.

Velázquez-Benítez, A. M., Antonio-López, J. E., Alvarado-Zacarías, J. C., Fontaine, N. K., Ryf, R., Chen, H., . . . Amezcua-Correa, R. (2018). Scaling photonic lanterns for space-division multiplexing. *Scientific Reports, 8*, 8897.

von Hoyningen-Huene, J., Ryf, R., & Winzer, P. (2013). LCoS-based mode shaper for few-mode fiber. *Optics Express, 21*(15), 18097-18110.

Wang, A., Wang, G. Z., & Claus, R. O. (1992, 8-11 Sept. 1992). *Study of near- and far-field two-lobe patterns outside the output endface of a two-mode fiber.* Paper presented at the Fibers '92, Massachusetts, USA.

Wang, A., Wang, G. Z., & Claus, R. O. (1993). *Study of near- and far-field two-lobe patterns outside the output endface of a two-mode fiber.* Paper presented at the Fiber Optic and Laser Sensors X, Boston, USA.

Weerdenburg, J. v., Ryf, R., Alvarado-Zacarias, J. C., Alvarez-Aguirre, R. A., Fontaine, N. K., Chen, H., . . . Okonkwo, C. (2018). 138-Tb/s mode- and wavelength-multiplexed transmission over six-mode graded-index fiber. *Journal of Lightwave Technology, 36*(6), 1369-1374.

Weng, Y., He, X., & Pan, Z. (2017). Space division multiplexing optical communication using few-mode fibers. *Optical Fiber Technology, 36*, 155-180.

Winzer, P. J. (2011). Energy-efficient optical transport capacity scaling through spatial multiplexing. *IEEE Photonics Technology Letters, 23*(13), 851-853.

Winzer, P. J. (2013, 22-26 Sept. 2013). *Spatial multiplexing: The next frontier in network capacity scaling.* Paper presented at the European Conference and Exhibition on Optical Communication (ECOC 2013), London, UK.

Winzer, P. J., Ryf, R., & Randel, S. (2013). Spatial multiplexing using multiple-input multiple-output signal processing. In I. Kaminow, T. Li & A. Willner (Eds.), *Optical Fiber Telecommunications* (Vol. VI B, pp. 433-490). Massachusetts, USA: Academic Press.

Wu, C., Liu, Z., Chung, K. M., Tse, M. V., Chan, F. Y. M., Lau, A. P. T., . . . Tam, H. (2012). Strong LP_{01} and LP_{11} mutual coupling conversion in a two-mode fiber Bragg grating. *IEEE Photonics Journal, 4*(4), 1080-1086.

Xia, C., Bai, N., Ozdur, I., Zhou, X., & Li, G. (2011). Supermodes for optical transmission. *Optics Express, 19*(17), 16653-16664.

Xie, Y., Fu, S., Zhang, M., Tang, M., Shum, P., & Liu, D. (2013). Optimization of few-mode-fiber based mode converter for mode division multiplexing transmission. *Optics Communications, 306*, 185-189.

Youngquist, R. C., Brooks, J. L., & Shaw, H. J. (1984). Two-mode fiber modal coupler. *Optics Letters, 9*(5), 177-179.

Zhu, B., Taunay, T. F., Fishteyn, M., Liu, X., Chandrasekhar, S., Yan, M. F., . . . Dimarcello, F. V. (2011). 112-Tb/s Space-division multiplexed DWDM transmission with 14-b/s/Hz aggregate spectral efficiency over a 76.8-km seven-core fiber. *Optics Express, 19*(17), 16665-16671.

Zhu, B., Taunay, T. F., Yan, M. F., Fini, J. M., Fishteyn, M., Monberg, E. M., & Dimarcello, F. V. (2010). Seven-core multicore fiber transmissions for passive optical network. *Optics Express, 18*(11), 11117-11122.

LIST OF PUBLICATIONS

Thesis related publications during the candidature

1. **Lee, Y.-S.**, Lim, K.-S., Islam, M. R., Lai, M.-H., & Ahmad, H. (2017). Dynamic LP_{01}–LP_{11} mode conversion by a tilted binary phase plate. *Journal of Lightwave Technology, 35*(16), 3597-3603.

2. **Lee, Y.-S.**, Lim, K.-S., Zaini, M. K. A., & Ahmad, H. (2017). LP_{11}–LP_{01} mode conversion based on an angled-facet two-mode fiber. *IEEE Photonics Technology Letters, 29*(12), 1007-1010.

3. **Lee, Y.-S.**, Lim, K.-S., Zaini, M. K. A., & Ahmad, H. (2018). Mode splitting based on polarization manipulation in few-mode fiber. *IEEE Journal of Quantum Electronics, 54*(4), 6800306.

Other publications during the candidature

1. Zaini, M. K. A., **Lee, Y.-S.**, Lim, K.-S., Nazal, N. A. M., Zohari, M. H., & Ahmad, H. (2017). Axial stress profiling for few-mode fiber Bragg grating based on resonant wavelength shifts during etching process. *Journal of the Optical Society of America B, 34*(9), 1894-1898.

2. Zaini, M. K. A., **Lee, Y.-S.**, Lim, K.-S., Nazal, N. A. M., Yang, H.-Z., & Ahmad, H. (2018). Enhanced optical delay line in few-mode fiber based on mode conversion using few-mode fiber Bragg gratings. *IEEE Journal of Quantum Electronics, 54*(5), 6800507.

3. Lim, K.-S., Islam, M. R., **Lee, Y.-S.**, Yang, H.-Z., & Ahmad, H. (2016). LP_{01}–LP_{11} cross-mode interference in a chirped grating inscribed in two-mode fiber. *IEEE Journal of Quantum Electronics, 52*(6), 6600206.

4. Islam, M. R., Gunawardena, D. S., **Lee, Y.-S.**, Lim, K.-S., Yang, H.-Z., & Ahmad, H. (2016). Fabrication and characterization of laser-ablated cladding resonances of two different-diameter photosensitive optical fibers. *Sensors and Actuators A: Physical, 243*, 111-116.

5. Lim, K.-S., Ong, Z.-C., **Lee, Y.-S.**, Zaini, M. K. A., & Ahmad, H. (2018). Pseudohigh-resolution spectral interrogation scheme for small signals from FBG sensors. *IEEE Transactions on Instrumentation and Measurement*, 1-7. doi: 10.1109/TIM.2018.2871279

6. Nazal, N. A. M., Lim, K.-S., **Lee, Y.-S.**, Salim, M. A. M., & Ahmad, H. (2019). Influence of internal stresses in few-mode fiber on the thermal characteristics of regenerated gratings. *Photonic Sensors*, 1-8. doi: 10.1007/s13320-018-0527-4

7. Lai, M.-H., Lim, K.-S., Gunawardena, D. S., **Lee, Y.-S.**, & Ahmad, H. (2017). CO_2 laser applications in optical fiber components fabrication and treatment: A review. *IEEE Sensors Journal, 17*(10), 2961-2974.

8. Liu, H., Yang, H., Qiao, X., Wang, Y., Liu, X., **Lee, Y.-S.**, Lim, K.-S., & Ahmad, H. (2017). Curvature and temperature measurement based on a few-mode PCF formed M-Z-I and an embedded FBG. *Sensors, 17*(8), 1725.

9. Lai, M.-H., Gunawardena, D. S., Lim, K.-S., Machavaram, V. R., Lee, S.-H., Chong, W.-Y., **Lee, Y.-S.**, & Ahmad, H. (2016). Thermal activation of regenerated fiber Bragg grating in few mode fibers. *Optical Fiber Technology, 28*, 7-10.